Investigating Galaxy Size Growth and Stellar Mass Assembly Through the Buildup of Stellar Haloes Since $z \sim 1.1$

by

Devin J. Williams

A Thesis Submitted to Saint Mary's University, Halifax, Nova Scotia in Partial Fulfillment of the Requirements for the Degree of Master of Science in Astronomy (Department of Astronomy and Physics)

August 2023, Halifax, Nova Scotia

Approved: _____
Dr. Marcin Sawicki
Supervisor

Approved: _____
Dr. Ivana Damjanov
Supervisor

Approved: _____
Dr. Robert Thacker
Examiner

Approved: _____
Dr. Vincent Hénault-Brunet
Examiner

Date: August 3, 2023

Acknowledgments

First, I want to express my immense gratitude to my supervisors Dr. Ivana Damjanov and Dr. Marcin Sawicki, for their tremendous support and guidance throughout my journey as a researcher. Their constant patience and expertise have been instrumental in improving both my research project and my fundamental understanding of the universe. Working alongside them and the extragalactic group at SMU has deepened my passion for pursuing a career in astronomy.

I also extend my sincere thanks to all of the faculty members and fellow graduate students in the Astronomy and Physics Department at SMU, who have made my time at Saint Mary's extremely pleasant. A special thanks to Dr. Robert Thacker and Dr. Vincent Hénault-Brunet for their feedback and suggestions on improving my thesis.

I would also like to acknowledge the incredible effort of Harrison Souchereau for laying the important technical foundations that made this thesis project and the last two years of my research possible.

Finally, I am forever grateful for the love and support from my parents Allan and Gail, whose unrelenting belief in me has helped make this journey possible.

"We are stardust brought to life, then empowered by the universe to figure itself out—and we have only just begun."

-Neil deGrasse Tyson

Contents

List of Figures

List of Tables

Investigating Galaxy Size Growth and Stellar Mass Assembly Through the Buildup of Stellar Haloes Since $z \sim 1.1$

by Devin J. Williams

Abstract

In our current theoretical framework of galaxy formation and evolution, galaxies assemble stellar halo components through galaxy-galaxy interactions and accretion of ex-situ material. Studying this buildup of stellar haloes helps us better understand the processes driving the size growth and mass assembly of galaxies. In this work, we investigate the stellar halo assembly of ∼500,000 galaxies over $0.2 \leq z \leq 1.1$, by analyzing the evolution in their radial surface brightness and colour profiles. We find that since z=1.1 more massive galaxies assemble larger and brighter stellar haloes, and this assembly is inducing negative colour gradients. Quiescent galaxies grow more through ex-situ accretion than star-forming galaxies of similar masses, which results in faster evolution of quiescent galaxy sizes (R_e). Our results suggest that minor mergers drive the size growth of galaxy haloes since z=1.1, while major mergers fuel the mass assembly and further size growth of the most massive ($M_\star \geq 10^{10.5} M_\odot$) quiescent galaxies.

August 3, 2023

Chapter 1

Introduction

Since the time of Edwin Hubble, who gave us the first formal classification of galaxies (Hubble 1936), we have strived to gain a better understanding of how galaxies evolve in our vast universe (e.g., Gott 1977; Kormendy & Djorgovski 1989; Gilmore et al. 1989; Conselice 2014; Naab & Ostriker 2017). In Hubble's classification (the famous *tuning fork* diagram, Fig. 1.1), galaxies are grouped based on their visual appearances (or their *morphologies*) into two broad groups known as *ellipticals* and *spirals* (Hubble 1936; Kormendy & Djorgovski 1989; Gilmore et al. 1989). These groups are then further subdivided based on particular morphological differences, such as the presence of a stellar bar in the central regions of spiral galaxies, or the level of ellipticity in elliptical galaxies (i.e. how spherical or oval they appear). Remarkably, this classification system has persisted to this day as we continue to group galaxies based on the Hubble sequence types (see Gordon 2007 for an updated tuning fork).

The two distinct galaxy groups are often referred to by their secondary names, which are *early-type* galaxies (ellipticals) and *late-type* galaxies (spirals). This naming

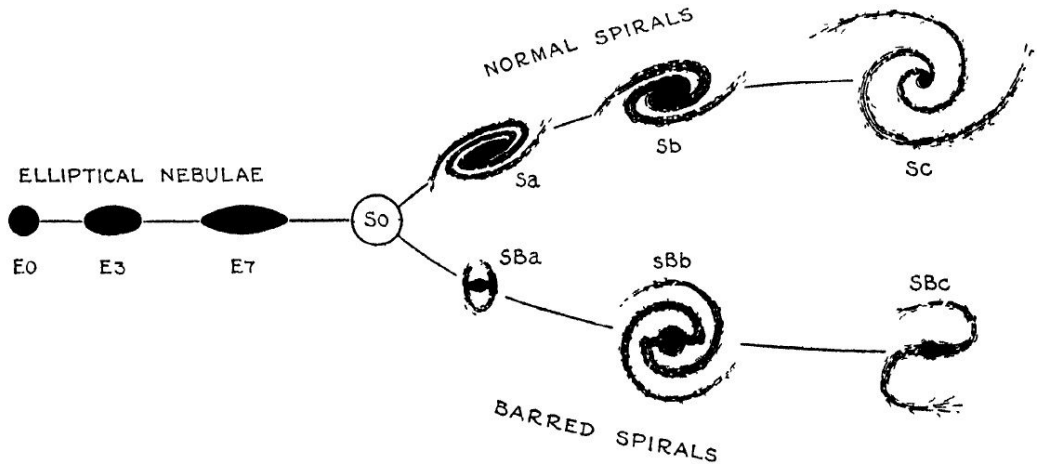

Figure 1.1. Original Hubble sequence diagram from the 1936 book "Realm of the Nebulae" (Hubble 1936).

system resulted from the initial (and incorrect) belief that Hubble's diagram (Fig. 1.1) could be viewed as an evolutionary sequence, where all galaxies evolve from elliptical to spiral-like morphologies over their lifetimes (Hubble 1936). We now know this to be mostly false and the sequence often goes in the opposite direction, as galaxies typically evolve from spiral to elliptical morphologies (e.g., Martig et al. 2009; Oser et al. 2010; Conselice 2014; Jackson et al. 2019, 2020). This can be inferred from comparing stellar mass functions of galaxies from high to low redshift, where star-forming spiral galaxies greatly outnumber non-star-forming (i.e. *quiescent*) elliptical galaxies at earlier times (higher redshifts). At lower redshifts, the number densities of both populations become more comparable due to the buildup of the quiescent elliptical population particularly at lower stellar masses (e.g., Santini et al. 2022).

Spiral galaxies consist of gas, dust, and stars that orbit the galaxy center in a rotationally-supported disk structure. This rotational motion is governed by the gravitational potential of the galaxy (e.g., Gilmore et al. 1989; Conselice 2014; Naab & Ostriker 2017). Over time, spiral galaxies can lose their disk structure through

different mechanisms, including internally driven secular processes (e.g., growth of a central stellar bar, quenching mechanisms) or interactions with their environment such as equal-mass mergers (e.g., Kormendy & Kennicutt 2004; Martig et al. 2009; Benson 2010; Jackson et al. 2019, 2020).

When a spiral galaxy loses its disk structure the motions of the gas and stars become governed by random velocity dispersion (i.e. the galaxy becomes *dispersion-dominated*). Due to the randomized stellar orbits, the overall morphology of the galaxy becomes elliptical or spheroidal (Gilmore et al. 1989; van Dokkum & Franx 2001a; Bell et al. 2006; Martig et al. 2009). Studies of the kinematic properties of elliptical galaxies have revealed that they can sometimes exhibit rotational motion or have embedded disk components (i.e. *fast rotators*), while others lack any significant rotation (i.e. *slow rotators*; e.g., Naab et al. 2014; Pulsoni et al. 2021). Furthermore, as demonstrated by Jackson et al. (2019, 2020), there are instances where interactions between galaxies can inject angular momentum and "spin up" a gaseous elliptical galaxy and reform a spiral disk structure. The complex nature of morphological transformations is why they remain an open field of research (e.g., Brennan et al. 2015; Park et al. 2022; Liu et al. 2021; Giri et al. 2023).

Just as galaxies differ in their morphological and dynamical properties, observations have revealed they also vary in colour (e.g., Kennicutt 1998; Strateva et al. 2001; Baldry et al. 2004; Balogh et al. 2004; Menci et al. 2005). Some galaxies are intrinsically bluer, typically the case for *spiral* galaxies (right-hand image in Fig. 1.2). Other galaxies are intrinsically redder (left-hand image in Fig. 1.2), typically seen in the *elliptical* or *bulge-dominated* galaxies (Strateva et al. 2001; Menci et al. 2005; Baldry et al. 2004; Balogh et al. 2004; Kennicutt 1998). This is an oversimplified picture,

however, as galaxies can display different colours throughout different physical regions giving rise to colour gradients (e.g., redder interiors and bluer outer regions; Tal & van Dokkum 2011; Hirschmann et al. 2015; Buitrago et al. 2017). Furthermore, some observational studies have presented evidence for the presence of red spiral galaxies (e.g., Shimakawa et al. 2022; Nelson et al. 2022) and blue elliptical galaxies (e.g., Mahajan et al. 2018; Moffett et al. 2019; Lazar et al. 2023).

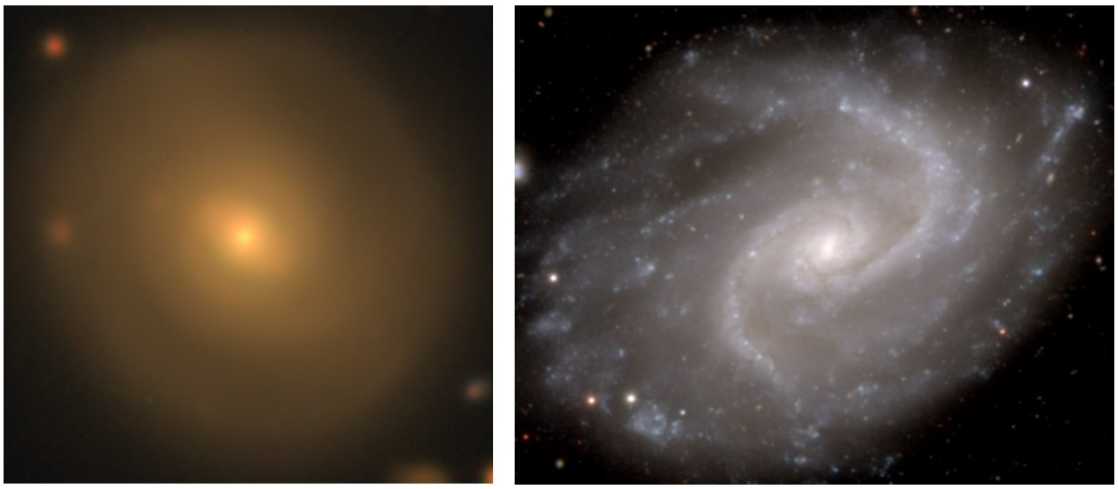

Figure 1.2. Two example galaxies from the HSC-SSP PDR3 observations (Aihara et al. 2022), showcasing a blue spiral galaxy (right) and a red elliptical galaxy (left). These R-G-B colour images were generated from the hscMap via the HSC-SSP PDR3 website (https://hsc-release.mtk.nao.ac.jp/doc/index.php/data-access__pdr3/), using the SDSS_TRUE_COLOR template and the i, r, and g-band filters as R-G-B colours, respectively.

The variety of colours we observe in galaxies reflects the types of stars that dominate their stellar populations (e.g., Kennicutt 1998; Gustafsson 1989; Strateva et al. 2001; Menci et al. 2005). When a galaxy is actively forming new stars in appreciable quantities, the colour of light we observe in those regions will be bluer. The bluer colours come from the hot massive young stars (e.g., O and B stars) which emit more at shorter (bluer) wavelengths (Gustafsson 1989; Bruzual & Charlot 2003;

Strateva et al. 2001; Arnouts et al. 2013). Since these stars are relatively short-lived, if a galaxy ceases its star formation (is *quenched*) it will no longer be able to replenish its source of blue light and will turn redder in colour over time (Gustafsson 1989; Strateva et al. 2001; Menci et al. 2005; Arnouts et al. 2013). This reddening of colours results from most of the light from a galaxy being dominated by the longer (redder) wavelength light emitted by older lower-mass stars (e.g., G, K, and M stars; Gustafsson 1989; Bruzual & Charlot 2003; Strateva et al. 2001; Arnouts et al. 2013).

Along with reddening due to the quenching of star formation or the ageing of stellar populations, higher stellar metallicities are also linked with redder colours in galaxies (e.g., Gustafsson 1989; Gilmore et al. 1989; Ferreras & Silk 2000; Streich et al. 2014). A larger abundance of heavy elements will lead to more absorption or scattering of shorter (bluer) wavelength light emitted from a galaxy, turning it redder in colour (e.g., Gustafsson 1989; Streich et al. 2014; Hirschmann et al. 2015). Additionally, the presence of dust within a galaxy, or intergalactic dust between the galaxy and the observer, can make a galaxy *appear* redder through extinction (e.g., Schlegel et al. 1998; Calzetti et al. 1993; Puget & Leger 1989; Moutard et al. 2018). By studying the colours of galaxies and how they evolve over time we can probe the physical processes that are affecting the evolution of their stellar populations (e.g., Pagel & Edmunds 1981; Bruzual & Charlot 2003; Hirschmann et al. 2015; Buitrago et al. 2017).

From observations, we have also learned galaxies differ in how large they are (e.g., Gilmore et al. 1989; Kormendy & Djorgovski 1989; Trujillo et al. 2007; Naab et al. 2009; Conselice 2014). When discussing how large a galaxy is we must consider its total stellar mass and physical size separately, despite their very dependent rela-

tionship (e.g., Stone et al. 2021; Zhang & Zaritsky 2016; Trujillo et al. 2007; Trujillo 2013; Matharu 2019; Damjanov et al. 2022b). The light we detect from a galaxy may translate into different amounts of stellar mass depending on the specific stellar population and stellar mass-to-light ratio ($M_\star/L$) of the galaxy. Most of the luminosity of a galaxy comes from its most massive (and less numerous) stars, while the fainter lower-mass stars (which are more numerous) contribute most of the stellar mass (e.g., Bell et al. 2003; Flynn et al. 2006; Szomoru et al. 2013; Du et al. 2020). Galaxies can span a wide range of stellar masses, from low-mass dwarf galaxies ($M_\star \sim 10^{6-7} M_\odot$; e.g., Lazar et al. 2023) to massive brightest-cluster galaxies ($M_\star \sim 10^{12} M_\odot$; e.g., Montenegro-Taborda et al. 2023). At a fixed stellar mass, galaxies can also span a range of sizes and thus densities (e.g., Trujillo et al. 2007; Damjanov et al. 2015; Matharu 2019). Galaxies can be small and compact, with most of their material concentrated near the center - an example are the so-called "red nugget" galaxies (e.g., Damjanov et al. 2009). Alternatively, galaxies can also be large in size and possess loosely bound extended material in their outer regions (e.g., tidal features, extended stellar haloes; Cooper et al. 2010; Giri et al. 2023).

Observations of galaxies from high to low redshift clearly show that galaxies are growing both in their physical sizes and total stellar mass content over time and that the rate of growth in both these properties varies in different types of galaxies (e.g., Faber & Gallagher 1979; Gilmore et al. 1989; Kormendy & Djorgovski 1989; White & Frenk 1991; Bell et al. 2006; Trujillo et al. 2007; van Dokkum et al. 2010). Gaining a better understanding of the processes that drive this size growth and stellar mass assembly in different galaxy populations has been a major focus of research efforts for decades (e.g., Roche et al. 1998; van Dokkum & Franx 2001a; Oser et al. 2010;

Cook et al. 2010; Rodriguez-Gomez et al. 2016; Buitrago et al. 2017; Naab & Ostriker 2017; Huang et al. 2018a,b; Tacchella et al. 2019; Huško et al. 2022).

1.1 Galaxy Size Growth and Stellar Mass Assembly

As galaxies first form through the accumulation of cold star-forming gas in virialized dark matter haloes (Naab & Ostriker 2017; Conselice 2014), one might naively think that simply prolonging this early star formation is how galaxies grow in stellar mass and size over time. While star formation may be part of the picture (especially for star-forming galaxies), previous observational and theoretical studies have demonstrated that internal star formation cannot account for the total stellar mass growth we see in individual galaxies from high to low redshift (e.g., van Dokkum et al. 2010; Oser et al. 2010; Cook et al. 2016; Rodriguez-Gomez et al. 2016; Pillepich et al. 2015; Tacchella et al. 2019; Spavone et al. 2021; Huško et al. 2022; Cannarozzo et al. 2022). Some simulations for example show that only $\sim 10-50\%$ of the total stellar mass content of massive galaxies ($10^{11-12} M_{\odot}$) at low redshift ($z \sim 0$), can be attributed to internal star formation (e.g., Davison et al. 2020; Huško et al. 2022).

Furthermore, there is substantial evidence for quiescent galaxies exhibiting evolution in both their size (or *effective radius*[1]) and stellar mass from high to low redshift (e.g., Bezanson et al. 2009; van Dokkum et al. 2010; van der Wel et al. 2014; Matharu 2019; Damjanov et al. 2019). In some observational studies for example, high-mass

[1]The effective radius (R_e) of a galaxy is the radius that contains 50% of the integrated light.

($M_\star \sim 10^{11} M_\odot$) quiescent galaxies evolve in stellar mass by a factor of ∼2 since $z \sim 2$ and evolve in size by a factor of ∼4 at fixed stellar masses (e.g., Daddi et al. 2005; Trujillo et al. 2007; Trujillo 2013). Lower stellar mass quiescent galaxies also exhibit signs of size growth with decreasing redshift, although to a lesser degree than the more massive galaxies (e.g., Kawinwanichakij et al. 2021). Growth seen in quenched galaxies clearly indicates that some mechanism in addition to internal star formation contributes to the size growth and stellar mass assembly of galaxies over time.

From simulations, our current understanding is that this additional growth in galaxies is being fueled by interactions with their local environment (e.g., Pillepich et al. 2014; Cook et al. 2016; Rodriguez-Gomez et al. 2016; Tacchella et al. 2019; Huško et al. 2022; Cannarozzo et al. 2022; Rey & Starkenburg 2022). The local environment of a galaxy refers to its physical location in the large-scale cosmic structure of the universe (i.e. the *cosmic web*). The cosmic web, which is made up of dark matter and gas, contains different components (or regions) where galaxies reside. These include the dense and populated node regions where galaxy clusters are located in large dark matter haloes. These node regions are connected by multiple filament components, and in between them are low-density cosmic void and sheet regions (Sousbie 2011; Wechsler & Tinker 2018; Kotecha et al. 2021). As galaxies evolve and move throughout the cosmic web, they can interact with other galaxies and accrete new material from them which accelerates their growth in size and stellar mass.

The theoretical framework that has been established through simulations is the *two-phase formation scenario of galaxies* (Oser et al. 2010; Cook et al. 2010). In this framework, galaxies first assemble through an initial *in-situ* growth phase, where a galaxy increases its stellar mass and size by internally forming new stars from its

gaseous material (Oser et al. 2010; Cook et al. 2010). In-situ assembly is a complex interplay between physical processes that work to enhance or quench star formation within a galaxy (see Sec 1.1.1). Following this phase, galaxies build up a secondary *ex-situ* stellar mass component (Sec 1.1.2) where galaxies accrete stars and gas through interactions with their external environment (e.g., mergers with galaxies). These fractions of accreted material (or *ex-situ fractions*) are predicted to be fairly small (∼3-20%) in low stellar mass galaxies ($M_\star \sim 10^{9-10} M_\odot$) but can be quite significant for more massive galaxies (∼50-90%, $M_\star \geq 10^{11} M_\odot$; Rodriguez-Gomez et al. 2016; Davison et al. 2020; Huško et al. 2022).

How a galaxy experiences these two phases of assembly (i.e. the *in-situ* and *ex-situ* phase) is more similar to a continuously fluctuating process rather than a definitive first and second phase (Huško et al. 2022; Lin et al. 2022). The star formation rate of a galaxy may fluctuate considerably over its lifetime, leading to periods of quenching and rejuvenation (e.g., Madau & Dickinson 2014; Jackson et al. 2020, 2022). Additionally, the frequency of mergers (different merger types discussed in Sec. 1.1.2) and the rate of growth due to external interactions will also vary throughout time for different types of galaxies (e.g., Rodriguez-Gomez et al. 2016; Tacchella et al. 2019; Rey & Starkenburg 2022; Conselice et al. 2022).

1.1.1 In-Situ Growth: Star Formation vs. Quenching

Stars form out of the cold gaseous material distributed throughout galaxies (mostly in the disks or spiral arms of spiral galaxies) when conditions allow for this material to coalesce and collapse through gravitational attraction (Kennicutt 1998; Bergin &

Tafalla 2007; McKee & Ostriker 2007). The compression of this baryonic material (i.e. molecular hydrogen) in proto-stellar cores causes the pressure and temperature to continuously rise, until the point where nuclear fusion ignites and stellar nucleosynthesis begins (e.g., Bergin & Tafalla 2007; McKee & Ostriker 2007). The ability of a galaxy to effectively utilize its supply of gas to form new stars (i.e. its star formation efficiency) can be influenced in a myriad of ways and is regulated by multiple processes acting simultaneously over time (Man & Belli 2018; Madau & Dickinson 2014).

Some processes can lead to an enhancement of star formation efficiency, by contributing extra fuel (baryonic material) or making conditions more favourable for stellar production (e.g., injecting angular momentum that reforms disk structures; Bergin & Tafalla 2007; McKee & Ostriker 2007; Jackson et al. 2020). A prime example of star formation enhancement is a starburst galaxy, characterized by a brief phase ($\sim$100 Myr) of significantly heightened star formation rates (Calzetti et al. 2002; Poggianti & Barbaro 1996; Di Matteo et al. 2008; Li et al. 2023). The cause of this starburst phase is still being investigated but has been linked to tidal interactions and mergers with other galaxies (e.g., Li et al. 2023; Renaud et al. 2022a). The starburst phase will end if the gas supply of the galaxy has been depleted, and this depletion of available material is one way that a galaxy can have its star formation *quenched*.

As summarized by Man & Belli (2018), a galaxy can quench through a variety of mechanisms that depend on a range of internal and external galaxy properties. These quenching mechanisms are often divided into two broad categories referred to as *mass* and *environmental quenching* processes (Peng et al. 2010; Moutard et al. 2018, 2020;

Zhang et al. 2021).

The mechanisms in the mass-quenching category involve physical processes that are internal to galaxies. This could include expelling the gas from galaxies or heating up the gaseous material making it unable to cool and collapse (e.g., AGN or stellar feedback; Man & Belli 2018). Stellar feedback occurs when massive stars go supernova and they inject large amounts of energy into their surrounding interstellar medium, which heats up the surrounding material making it harder to form further stars (Naab & Ostriker 2017; Man & Belli 2018). An active galactic nucleus (AGN) is a supermassive black hole (SMBH) at the center of a galaxy that is actively accreting material. AGN can release energy through radiation and jet activity, which can expel stellar material from galaxies or increase the temperature of the gas making it unable to cool and collapse for further star formation (Naab & Ostriker 2017; Davies et al. 2022). These mass-quenching mechanisms work in all galaxies to some degree but exert greater influences in galaxies of higher stellar masses. For example, massive galaxies have larger SMBHs and more material for them to accrete and therefore will experience stronger feedback from AGN activity (Peng et al. 2010; Moutard et al. 2020; Contini et al. 2020; Zhang et al. 2021).

Environmental quenching mechanisms include processes that are driven by external sources in the cosmic environment of a galaxy. External quenching processes can remove the gas supply from a galaxy, as in the case of ram-pressure stripping (e.g., Abadi et al. 1999; Hester 2006; Boselli et al. 2022). This is often experienced in dense cluster environments, where the hot intra-cluster medium acts like a strong wind that is able to overcome the gravitational potential of a galaxy and strip away its material. Galaxy *harassment* (Moore et al. 1996), or close high-speed encounters

with other galaxies (e.g., flybys), can also cause changes in the morphologies or internal properties of galaxies (e.g., gas temperature or density) and induce quenching. These environmental quenching mechanisms are more dominant in galaxies of lower stellar masses ($M_\star \lesssim 10^{9.5-10} M_\odot$; Moutard et al. 2018; Zhang et al. 2021), as they have shallower gravitational potentials which makes it harder to retain material from being stripped away. Environmentally-driven quenching is also more prevalent in denser environments of the cosmic web (Kuschel et al. 2022; McNab et al. 2021). In denser environments (i.e. galaxy cluster vs. cosmic void) there are more galaxies to interact with, and the gas encountered in the intergalactic medium (IGM) is hotter and denser.

1.1.2 Ex-Situ Buildup: Mergers and Accretion

Mergers between galaxies are often classified by the relative mass ratio of the merging partners ($\mu_\star = M_{\star 1}/M_{\star 2}$; Cook et al. 2016; Rodriguez-Gomez et al. 2016; Huško et al. 2022). Major mergers are between galaxies of similar masses ($\mu_\star \geq 0.25$), while minor mergers are between a larger and a smaller galaxy ($0.1 \leq \mu_\star < 0.25$). Additionally, a third ex-situ channel is sometimes defined for mergers between a galaxy and a smaller object (e.g., globular cluster, dwarf galaxy), or when accretion occurs but galaxy cores do not coalesce (e.g., flyby instead of a merger, accretion of a stellar stream; Rodriguez-Gomez et al. 2016; Huško et al. 2022). In this work, we will refer to these three ex-situ channels as the *major* ($\mu_\star \geq 0.25$), *minor* ($0.1 \leq \mu_\star < 0.25$), and *very minor merger* ($\mu_\star < 0.1$) channels. In Fig. 1.3 we illustrate these different merger types with a set of images and diagrams.

An additional classification we will mention in this work is based on the amount of gas involved in the merger. A merger involving gas-rich galaxies is typically called a "wet" merger (e.g. merger between two gaseous disk galaxies). Alternatively, a "dry" merger occurs between two gas-poor galaxies (e.g. two gas-deficient quiescent elliptical galaxies; Boylan-Kolchin et al. 2005; Bell et al. 2006; Trujillo et al. 2007; Graham 2023). We illustrate both wet and dry merger types in the left-hand diagram in Fig. 1.3 (denoted by the ×2 and wet or dry labels).

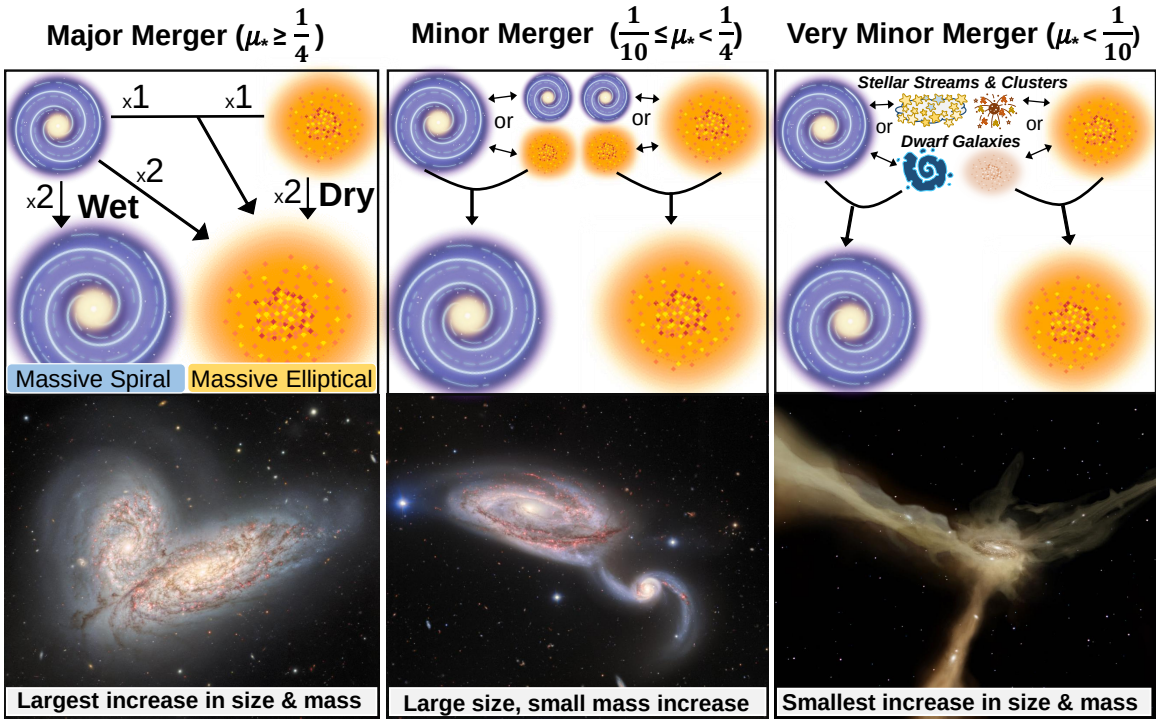

Figure 1.3. Diagram of galaxy merger types (see Sec. 1.1.2), showing major (left column), minor (center column) and very minor (right column) merger channels. Mass ratio ($\mu_\star$) definitions are shown along the top. Diagrams in the top row illustrate different merger combinations that result in a large spiral or elliptical galaxy, with the largest increase in size and stellar mass resulting from larger merger ratios. In the left-hand panel are examples of a "wet" merger between two gas-rich disk galaxies, and a "dry" merger between two gas-poor spheroidal galaxies. The (×1) and (×2) in the left-hand diagram convey whether two spiral galaxies, two elliptical galaxies, or one of each were involved in the merger.

One open question regarding merger-driven growth in galaxies is which ex-situ channel is driving the majority of the size and stellar mass evolution we see in different galaxy populations (Naab et al. 2009; Trujillo et al. 2011; Ownsworth et al. 2014; Borlaff et al. 2014; Peschken et al. 2020; Cannarozzo et al. 2022). Constraining galaxy merger rates is challenging, as studies using both observations (e.g., Conselice et al. 2009a; Bridge et al. 2010; Newman et al. 2012; Man et al. 2016; Sawicki et al. 2020; Nevin et al. 2023; Conselice et al. 2022) and simulations (e.g., Rodriguez-Gomez et al. 2016; Davison et al. 2020; Huško et al. 2022; Cannarozzo et al. 2022) have produced varying results.

Both observational and theoretical studies have argued that major mergers dominate the assembly histories of more massive galaxies (Faber et al. 2007; Naab et al. 2007; Conselice et al. 2009b; Borlaff et al. 2014; Mantha et al. 2018; Peschken et al. 2020), and that major mergers are occurring at low redshifts ($z \lesssim 1$) as well as high redshifts ($z \gtrsim 2-3$; Cannarozzo et al. 2022; Sotillo-Ramos et al. 2022; Giri et al. 2023). Other studies (both observational and simulation-based) instead support a more minor merger-driven scenario (Naab et al. 2009; Bundy et al. 2009; Trujillo et al. 2011; Ownsworth et al. 2014; Jackson et al. 2022), where galaxies build up gradually through consecutive minor mergers at lower redshifts ($z \lesssim 1$), and major mergers are only important at higher redshifts ($z \gtrsim 2-3$). Further complicating the issue of which ex-situ channel is dominating galaxy assembly, is the unknown contribution from merger-induced star formation and starburst phases (Di Matteo et al. 2008; Huško et al. 2022; Li et al. 2021; Renaud et al. 2022b).

Major mergers will contribute the most to stellar mass growth in a galaxy as there is more material to accrete. Using the viral theorem and conservation of energy

arguments, this increase in stellar mass results in a linearly proportional increase in size in the remnant galaxy with

$$\frac{R_f}{R_i} \propto \frac{M_f}{M_i}, \tag{1.1}$$

where (R_f and M_f) represent the final radius and stellar mass of the galaxy, and (R_i and M_i) represent the initial amounts prior to the accretion of material from the merger (see Naab et al. 2009 and Bezanson et al. 2009 for detailed derivations). Using the same arguments, minor or very minor mergers are expected to cause a stronger evolution in size for a given increase in stellar mass ($\frac{R_f}{R_i} \propto (\frac{M_f}{M_i})^{2-2.5}$; Naab et al. 2009; Bezanson et al. 2009; Hopkins et al. 2010; Trujillo et al. 2011).

Due to their energetically violent nature and their effect on the orbital velocities of stars within a galaxy, major mergers are expected to induce significant morphological transformations in galaxies (Martig et al. 2009; Kaviraj 2014; Graham 2023). Observational and theoretical studies argue that the product of a major merger is a large elliptical or spheroidal galaxy, as disk structures get destroyed and material from both galaxies is mixed together into a large gravitationally bound but dispersion-dominated structure (e.g., Martig et al. 2009; Pulsoni et al. 2021; Jackson et al. 2020, 2022). Given the high stellar masses of some galaxies ($\sim 10^{12} M_{\odot}$), it has been argued that major mergers are necessary to explain the buildup of such massive objects (e.g., Bluck et al. 2012; Mantha et al. 2018; Sawicki et al. 2020; Huško et al. 2022). However, if major mergers were a dominating ex-situ channel and galaxies experienced them frequently, we would expect to see higher abundances of massive galaxies in the local universe than we do today (e.g., Hopkins et al. 2010; Trujillo 2013; Santini et al. 2022).

During minor or very minor mergers, the larger galaxy accretes material from the smaller system and distributes it throughout its outskirts, growing its stellar halo and increasing its measured size (e.g., Trujillo et al. 2007; Naab et al. 2009; Huško et al. 2022; Huang et al. 2018a). The morphological transformations induced by these minor interactions are often much more subtle than the more energetic major mergers (e.g., Lambas et al. 2012; Giri et al. 2023). Minor and very minor mergers are able to enhance disk structures already in place rather than destroy them and are even linked with the reformation of a previously disrupted disk (e.g., Jackson et al. 2020, 2022). Since minor mergers are measured to be more frequent than major mergers, particularly at low redshift $z \lesssim 1$ (e.g., Conselice et al. 2022), they have been proposed as a likely explanation for the accelerated size evolution seen in the quiescent population (e.g., the observed increase in size by a factor of $\sim$4 since $z \sim 2$ in massive quiescent galaxies; e.g., Daddi et al. 2005; Trujillo et al. 2007; Trujillo 2013).

1.1.3 Alternative Contributions to Observed Growth

While mergers and accretion of ex-situ material are efficient in explaining the evolution in average sizes in different galaxy populations, it is important to consider the possible contributions from additional effects. One such effect that influences our measurements of how average quiescent galaxy sizes have evolved across redshift is the effect of *progenitor bias* (van Dokkum & Franx 1996, 2001b; Carollo et al. 2013; Saglia et al. 2016; Damjanov et al. 2019, 2022a). When comparing populations of quiescent galaxies from high to low redshift, we must take into account that some

low-redshift quiescent galaxies were, in fact, star-forming galaxies at high redshift (that have since quenched). As star-forming galaxies are typically larger in size than quiescent galaxies of similar masses (e.g., van der Wel et al. 2014; Mowla et al. 2019b), this effect of star-forming galaxies entering our lower redshift quiescent samples will bias our measurements of the average growth in size of the quiescent population.

This contribution from progenitor bias is important to consider but does not negate the need for additional assembly mechanisms such as ex-situ accretion through mergers. For example as Damjanov et al. (2022a) recently demonstrated, only $\sim 11\%$ of the size evolution seen in their massive ($\sim 10^{11} M_{\odot}$) quiescent sample since $z \sim 0.6$, could be attributed to the effect of progenitor bias. This contribution is expected to increase for galaxies of lower stellar masses, simply due to the larger size difference between star-forming and quiescent galaxies at lower stellar masses (e.g., $10^{9-10} M_{\odot}$; Mowla et al. 2019b; Kawinwanichakij et al. 2021).

Another factor to consider is the internal physical processes operating in individual galaxies which can influence their individual size growth or stellar mass assembly. One mechanism that can affect the sizes of galaxies is the "puffing up" scenario induced by *adiabatic expansion* (e.g., Hopkins et al. 2010; Damjanov et al. 2009). This occurs when a galaxy loses mass from its central regions in an adiabatic fashion (e.g., through AGN and stellar feedback), leading to a shallower gravitational potential. In response to the change in potential, the system expands. As demonstrated by the simulations of Hopkins et al. (2010), the contribution to size growth from adiabatic expansion is predicted to be smaller than the contribution from mergers (of any mass ratio). The effect is not negligible however, and can possibly account for up to a factor of ~ 2 increase in size (R_e) since $z \sim 2$ (Hopkins et al. 2010).

As demonstrated by the simulations of Boecker et al. (2023), stars born in the outer regions of galaxies ($R \gtrsim 10$ kpc) can migrate towards the center and account for up to $\sim 23\%$ of the stellar material in the inner core region of a galaxy ($R < 1$ kpc). These migrated stars have the ability to contribute to bulge and stellar bar components in galaxies, which could affect the measurements of galaxy sizes (R_e). Additionally, these structural components (i.e. a stellar bar or bulge) often impact the level of star formation in galaxy central regions (i.e. induce quenching), and can thus influence the in-situ stellar mass assembly of galaxies (e.g., Géron et al. 2021; Dimauro et al. 2022; Boecker et al. 2023).

1.2 Studying Assembly Histories Through Stellar Haloes

Our understanding of how galaxy mergers and the accretion of ex-situ material influence the assembly of galaxies (i.e. the ex-situ phase of the two-phase formation scenario) is through simulations (e.g., Oser et al. 2010; Pillepich et al. 2014; Cook et al. 2010, 2016; Rodriguez-Gomez et al. 2016; Tacchella et al. 2019; Davison et al. 2020; Huško et al. 2022; Rey & Starkenburg 2022). This is due to the additional capabilities provided by simulations, such as the ability to establish merger trees and follow the evolution of individual galaxies over large timescales (e.g., Rodriguez-Gomez et al. 2016; Tacchella et al. 2019; Huško et al. 2022). One common finding amongst these studies is that the stellar halo components of galaxies are prime areas to search for evidence of this merger-driven buildup (e.g., Hirschmann et al. 2015; Cook et al. 2016;

Pulsoni et al. 2021; Genina et al. 2023).

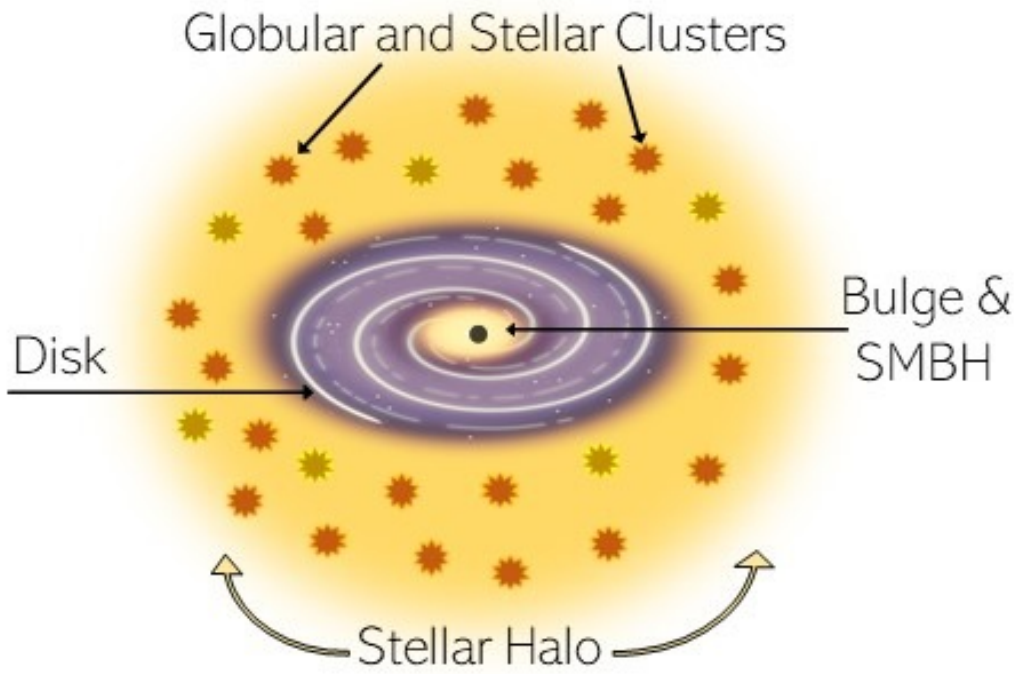

Figure 1.4. Illustration of different galaxy structural components, based on a similar diagram from The European Space Agency (ESA) website - https://www.esa.int/ESA_Multimedia/Images/2016/09/Anatomy_of_the_Milky_Way. While the diagram represents a spiral disk galaxy, an elliptical galaxy can be viewed in the same way, just with a much larger bulge component instead of a disk structure.

Stellar haloes (see Fig. 1.4) are large and diffuse stellar components that surround galaxies (Cooper et al. 2010). The stellar haloes are understood to be one of the last structural components to assemble in a galaxy and are gradually built up over time from the accretion and redistribution of stars, gas, and smaller bodies (e.g., globular clusters) that a galaxy acquires (Cook et al. 2016; Buitrago et al. 2017; Huško et al. 2022; Rey & Starkenburg 2022). The different types of interactions a galaxy experiences (e.g., the merger types shown in Fig. 1.3) will influence the stellar populations throughout its stellar halo in different ways (Lambas et al. 2012; Hirschmann et al. 2015; Cook et al. 2016; Cannarozzo et al. 2022). This activity can

potentially leave unique observable signatures in the stellar haloes of galaxies that act like fossil evidence of the assembly history of the observed galaxy.

For this reason, stellar halo regions have been the focus of many recent observational studies investigating the ex-situ phase of galaxy assembly (e.g., Iodice et al. 2017; Huang et al. 2018a; Smercina et al. 2020; Spavone et al. 2017, 2021; Gilhuly et al. 2022). A commonly used method of analyzing the stellar haloes of observed galaxies is through the extraction of 1D radial profiles, that measure how different galaxy properties change with radius (e.g., D'Souza et al. 2014; Huang et al. 2018a; Spavone et al. 2021; Gilhuly et al. 2022). Two particular radial profiles that simulations have shown can act as efficient tracers of galaxy assembly are surface brightness and colour profiles (Hopkins et al. 2010; Hilz et al. 2013; Pillepich et al. 2014; Hirschmann et al. 2015; Cook et al. 2016). For example, Hilz et al. (2013) and Hopkins et al. (2010) have demonstrated the surface brightness profiles of galaxies will undergo different changes depending on the type of merger or physical process (e.g., adiabatic expansion) a galaxy experiences. Similarly, different types of mergers are predicted to induce different effects on colour profiles and colour gradients throughout a galaxy (e.g., Bernardi et al. 2011; Lambas et al. 2012; Hirschmann et al. 2015).

1.2.1 Radial Surface Brightness and Colour Profiles

Radial surface brightness profiles (also referred to as *light profiles* for simplicity throughout this text) depict how the observed surface brightness of a galaxy in a given wavelength or photometric band, changes with increasing distance from its center (Graham & Driver 2005; Jedrzejewski 1987). The technique used to extract and

construct radial surface brightness profiles from galaxy images is known as *elliptical isophote analysis* (Jedrzejewski 1987), and is illustrated in Fig. 1.5.

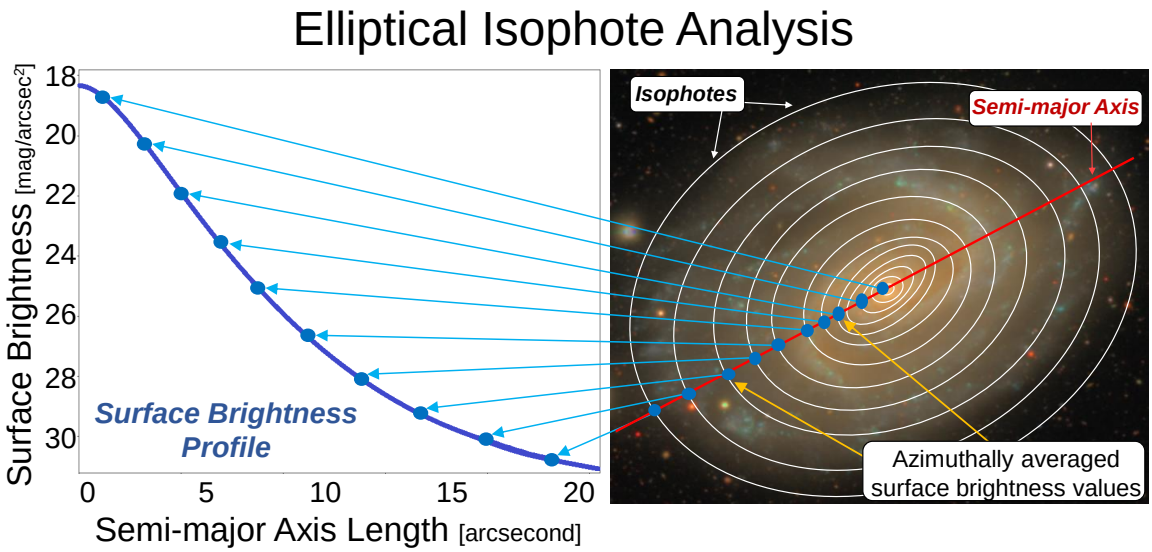

Figure 1.5. Simplified illustration of elliptical isophote analysis (Jedrzejewski 1987), discussed in Sec. 1.2.1. On the right is a galaxy image of a large low-redshift spiral galaxy from the HSC-SSP PDR3 observations (Aihara et al. 2022). The image is fit with white ellipses (*isophotes*) and the semi-major axis is identified with the red line. The mean surface brightness value along an individual elliptical isophote (i.e. the *azimuthally averaged* value) forms the single surface brightness value used in the 1D radial profile for that given semi-major axis length. See Jedrzejewski (1987) for details on the theory behind this procedure, and see Souchereau et al. (in prep.) for technical details on the computational implementation we use in this work.

In this procedure, an image of a galaxy is fit with ellipses of roughly constant surface brightness (within errors) called *isophotes* (Jedrzejewski 1987). The isophotes (white ellipses in Fig. 1.5) continuously increase in size and decrease in surface brightness from galaxy center to outskirts. The isophotes will also differ in other

properties[2] such as their ellipticity[3] and position angle. These additional parameters can provide information about the shape and structure of a galaxy (Jedrzejewski 1987; Graham & Driver 2005). For example, the parameter `a4`, a fourth-order harmonic coefficient involved in the fitting routine, can provide information about the shape of the isophote and whether it is *boxy* or *disky* (e.g., Bender et al. 1988; de Jong & Davies 1997). Disky isophotes arise from having extra light along the semi-major axis and can reveal the presence of an embedded disk component. Boxy isophotes instead have extra light in the corners of the ellipses and are typically associated with large and luminous elliptical galaxies.

The 1D radial light profile is formed by taking the mean surface brightness of all values along an isophote (as they are only constant within errors), to be the single surface brightness value at that radius in the semi-major axis direction (red line in Fig. 1.5). By taking the mean surface brightness value along each isophote, the surface brightness values are *azimuthally averaged* which increases the signal-to-noise ratio by using additional pixel information (Jedrzejewski 1987). The outcome of the procedure is a 1D radial surface brightness profile which shows the mean isophote surface brightness values on the y-axis as a function of semi-major axis length on the x-axis (i.e. the radius of the isophote in the semi-major axis direction). The number of isophotes shown in Fig. 1.5 has been reduced for visual clarity, but in practice, the number of isophotes used is larger and they are more finely spaced, which produces

[2]For a full list of parameters that result from fitting isophotes in this procedure, see https://photutils.readthedocs.io/en/stable/api/photutils.isophote.IsophoteList.html#photutils.isophote.IsophoteList.

[3]Ellipticity (e) is defined as $e = 1 - (b/a)$, where (a) and (b) represent the semi-major and semi-minor axis of a galaxy, respectively.

a more finely sampled and smoother light profile (e.g., blue profile in Fig. 1.5).

These light profiles enable us to study stellar haloes through the intrinsic properties of galaxies, providing valuable information on how stellar population properties change with galactocentric radius as observed through different photometric bands. These profiles also allow us to discern morphologies of galaxies simply through the shapes of their 1D surface brightness profiles. A common model used to represent the 1D light profile of a galaxy is the Sérsic model (Sérsic 1963), where the intensity (I, related to surface brightness via Eq. 3.3) as a function of galactocentric radius (R) is described by

$$I(R) = I_e \exp\left(-b_n\left[\left(\frac{R}{R_e}\right)^{1/n} - 1\right]\right). \tag{1.2}$$

In Eq. 1.2 R_e is the effective radius defined to be the radius which contains half of the integrated light of the galaxy, and I_e is the intensity at that effective radius. The Sérsic index (n) will influence both the slope and central concentration of the light profile. The final term, b_n, is defined in terms of the Sérsic index and different analytical approximations are summarized in Graham & Driver (2005).

Different Sérsic indices (n) are typically associated with different morphologies of galaxies and galaxy structural components. For example, the light profile of a spiral galaxy or disk structure is often represented with a $n = 1$ Sérsic model (Trujillo et al. 2001a; Graham & Driver 2005; Simard et al. 2011), while light profiles of elliptical galaxies or bulge components are better represented with higher (e.g., $n \gtrsim 3 - 4$) Sérsic indexes (Trujillo et al. 2001a; Graham & Driver 2005; Simard et al. 2011). Real galaxy light profiles are often better represented by a combination of

multiple components, and thanks to our modern computational capabilities we often fit whole galaxy images with 2D models (e.g., `Sersic2D` Astropy Collaboration et al. 2013) rather than simplified 1D models (Simard et al. 2011; Trujillo & Fliri 2016; Spavone et al. 2020, 2021). These 2D models better represent the true complexity of galaxy morphologies and their light distributions, by providing information on how the surface brightness of a galaxy is spatially distributed across the whole image.

As mentioned in Sec. 1.2, galaxy light profiles can serve as tracers of galaxy assembly. Changes in profile shape or brightness can indicate which internal physical processes (Sec. 1.1.1 and Sec. 1.1.3) or external interactions (e.g., mergers, Sec. 1.1.2) have influenced the evolution of a galaxy. Regarding galaxy mergers for example, major mergers are expected to induce the largest amount of growth (i.e. increase in brightness), and this buildup of stellar material can occur as inward as central galaxy regions (e.g., 0-1R_e; Genina et al. 2023; Hopkins et al. 2010; Hilz et al. 2013). On the contrary, minor and very minor mergers (Sec. 1.1.2) will produce a smaller amount of growth in galaxy light profiles and are predicted to build up the outer regions (e.g., $R \gtrsim 2-3R_e$) more than the inner regions (Hopkins et al. 2010; Hilz et al. 2013).

Related to radial surface brightness profiles are radial colour profiles, which analyze how the colour of a galaxy's light is changing with distance from its center (i.e. more red or blue). These are formed by subtracting the surface brightness measured within one photometric band (longer, redder wavelengths) from the surface brightness in a shorter (bluer) wavelength range (Hirschmann et al. 2015; Buitrago et al. 2017; Consolandi et al. 2016; Miller et al. 2023). Similar to light profiles, radial colour profiles and colour gradients can also be used as tracers of galaxy assembly (e.g., Lambas et al. 2012; Hirschmann et al. 2015; Huang et al. 2018a; Spavone et al. 2021). However,

due to the number of effects that can influence galaxy colours (e.g., effects of dust, stellar metallicities, aging of the stellar population), it is more difficult to disentangle the exact processes that contributed to the assembly history of an individual galaxy. Despite this, simulations predict that we should still be able to distinguish between merger histories (i.e. driven by minor vs. major mergers) through the steepness of colour gradients (Hirschmann et al. 2015).

Minor or very minor mergers are predicted to induce bluer colours in galaxy outskirts and steeper (more negative) colour gradients (Lambas et al. 2012; Hirschmann et al. 2015). This arises from the larger galaxy accreting bluer stellar material from the lower-mass merging companion and distributing it throughout its stellar halo. Lower-mass galaxies have lower stellar metallicities and are often found to be star-forming spiral galaxies (e.g., Santini et al. 2022), which provide bluer stellar populations to accrete. Major mergers on the other hand should induce flatter colour gradients (Lambas et al. 2012; Hirschmann et al. 2015), as they are more efficient in mixing the stellar populations throughout a galaxy which eliminates (flattens out) any gradients in stellar properties (e.g., colours, ages, and metallicities).

1.3 Motivations and Research Goals of This Thesis

A key objective of modern galaxy formation and evolution studies is to better understand the processes that are driving the observed size growth, structural evolution, and stellar mass assembly of galaxies. As mentioned in Sec. 1.1, simulations have identified two main phases of galaxy assembly - the *in-situ* (Sec. 1.1.1) and *ex-situ* (Sec. 1.1.2) phases (Oser et al. 2010; Cook et al. 2010).

Simulations have provided much of what we know concerning the ex-situ phase, and how galaxy mergers and the accretion of ex-situ material are influencing the evolution of galaxies (e.g., Cook et al. 2016; Rodriguez-Gomez et al. 2016; Pillepich et al. 2015; Huško et al. 2022). Despite the theoretical framework and understanding we have established through these studies, there remain some open questions and topics of disagreement on how ex-situ driven assembly is proceeding in different galaxies (e.g., minor vs major merger driven assemblies, see discussion in Sec. 1.1.2). Furthermore, in order to truly understand this crucial phase of galaxy assembly, these predictions need to be tested with observational evidence. Some recent observational studies investigate this ex-situ-based assembly in real galaxies through the buildup of stellar haloes and extended material. However, these previous works have been mostly limited to the massive galaxy population (e.g., $M_\star \gtrsim 10^{11} M_\odot$; van Dokkum et al. 2010; Bezanson et al. 2009; Ownsworth et al. 2014; Huang et al. 2013, 2018a), small-numbered galaxy samples (e.g., Bell et al. 2006; Coccato et al. 2010; Trujillo et al. 2011; Bluck et al. 2012), or a low redshift range (e.g., $z < 0.1$; D'Souza et al. 2014; Spavone et al. 2017, 2021; Iodice et al. 2017; Gilhuly et al. 2022).

In this work, we aim to address these limitations by analyzing an extremely large observed galaxy sample (500,621 galaxies, see Table 3.1) across a wide range of redshift beyond the local universe ($0.2 \leq z \leq 1.1$). By analyzing the assembly and evolution of the stellar halo components in these galaxies, we investigate the mechanisms driving their growth in size and stellar mass since $z \sim 1.1$. Our galaxy sample consists of both star-forming and quiescent galaxies with stellar masses of $M_\star \geq 10^{9.5} M_\odot$, enabling us to study stellar halo assembly in a variety of different galaxy populations. Analyzing this assembly in galaxies over our wide redshift range

enables us to probe how merger activity and ex-situ accretion influence the evolution of galaxies over a large range of cosmic time (∼6 Gyr). By comparing our results with others from the literature, we test predictions from simulations concerning the ex-situ phase of galaxy assembly (Sec. 1.1 and 1.1.2).

To accomplish these objectives we make use of the observations and associated catalogues of the CLAUDS (Sawicki et al. 2019) and HSC-SSP (Aihara et al. 2018) surveys, two complementary imaging surveys which offer excellent depth and area coverage (details in Sec. 2.1). From the galaxies in these observations, we extract 1D radial surface brightness and rest-frame U-g colour profiles (Sec. 1.2.1). By analyzing how these radial light and colour profiles are changing in different galaxy sub-populations over our full redshift range, we are able to probe the processes driving the size growth and stellar mass assembly of galaxies since $z \sim 1.1$.

This thesis is structured as follows. In Chapter 2 we describe our observational datasets and outline the selection and refinement of our final galaxy sample. In Chapter 3 we describe our methodology and computational procedures used to extract radial profiles, and the steps taken to prepare results for scientific analysis. We present the main results of our work in Chapter 4, along with further discussion and comparisons with predictions from the literature in Chapter 5. Finally in Chapter 6 we summarize our conclusions and discuss future research objectives. Throughout this work, magnitudes are quoted in the AB system and a ΛCDM cosmological model with $\Omega_m = 0.3$, $\Omega_m = 0.7$, and $H_o = 70\text{km s}^{-1}\text{Mpc}^{-1}$ is assumed.

Chapter 2

Datasets and Sample Selection

To properly investigate the stellar haloes of galaxies and their faint outer regions, we require observations of galaxies capable of reaching low surface brightness levels (Merritt et al. 2020; Li et al. 2021; Trujillo & Fliri 2016). Furthermore, to study the buildup of stellar haloes over large timescales and discuss the evolution of galaxies on a population level, a sufficiently large sample of galaxies spread across a wide range of redshift is required. These factors heavily influenced the selection of datasets for this work, and the combined observations of the Hyper Suprime-Cam Subaru Strategic Program (HSC-SSP; Aihara et al. 2018) and The CFHT Large Area U-band Deep Survey (CLAUDS; Sawicki et al. 2019) are particularly well suited to address the research objectives and technical requirements of this study (Sec. 1.3).

2.1 HSC-SSP and CLAUDS Imaging Surveys

For the HSC-SSP observations, we have made use of the images from the Deep (26 deg^2) and UltraDeep (3.5 deg^2, embedded within Deep fields) layers of the third Public Data Release (PDR3; Aihara et al. 2022). These images were taken with the Hyper Suprime-Cam on the 8.2m Subaru Telescope (NAOJ) using a set of broad and narrow-band photometric filters (see Aihara et al. 2018 for full details). The specific filters and image sets we use are the five broadband photometric filters - g, r, i, z, and y (or simply $grizy$ throughout this text). Figure 2.1 displays the range of wavelengths covered as well as the transmission curves of each individual filter.

The CLAUDS survey (Sawicki et al. 2019) covers similarly large areas of the same Deep (18.6 deg^2) and UltraDeep fields (1.36 deg^2, embedded within the Deep layer) as HSC-SSP and extends the wavelength coverage into the ultraviolet (UV) regime (<4000 Å). The observations from CLAUDS were taken by the MegaCam imager on the 3.6m Canada-France-Hawaii Telescope (CFHT), using two UV-band filters - u & u^* (transmission curves also shown in Figure 2.1). We will use "U-band" in this text to refer to both (or either) of these MegaCam filters and the broad wavelength range of ∼3000-4000 Å (as described by Sawicki et al. 2019). The addition of the CLAUDS U-band data provides a number of important benefits to our study, such as improving the accuracy of galaxy photometric redshift measurements (Sawicki et al. 2019; Desprez et al. 2023), and enabling us to extract rest-frame U-g colour profiles (see Sec. 3.2.3) from lower redshift galaxies ($z < 0.35$).

In Table 2.1 we show additional information on the individual $U + grizy$ photometric filters. The seeing of each filter refers to the effect of its point-spread function

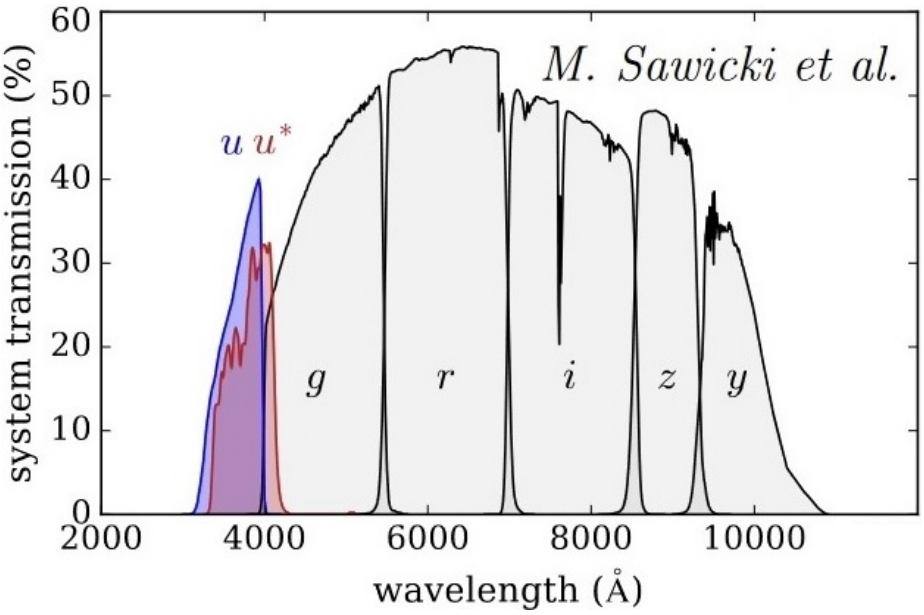

Figure 2.1. Transmission curves for the full set of photometric filters used in this work, showing the u and u^* filters from CLAUDS (Sawicki et al. 2019) and *grizy* filters from HSC-SSP (Aihara et al. 2018). Figure acquired from Sawicki et al. 2019 with permission.

Filter	**Central λ** [Å]	**Width** [Å]	**Seeing** [*arcsec*]	**Depth (Deep/UD)** [*mag*]	**Area (Deep/UD)** [deg^2]
u/u*	3538/3743	868/758	0.92	27.1 / 27.7	18.6 / 1.36
g	4754	1395	0.83	27.4 / 28.2	26 / 3.5
r	6175	1503	0.77	27.1 / 27.9	26 / 3.5
i	7711	1574	0.66	26.9 / 27.7	26 / 3.5
z	8898	766	0.78	26.3 / 27.1	26 / 3.5
y	9762	783	0.70	25.3 / 26.1	26 / 3.5

Table 2.1: Properties of the $U + grizy$ photometric filters of the HSC-SSP (Aihara et al. 2018) and CLAUDS (Sawicki et al. 2019) surveys. Specific properties are defined and discussed throughout Section 2.1. Depths listed for HSC-SSP *grizy* filters are 5σ depths for point sources, while CLAUDS U-band filters are 5σ depths in 2" apertures. Areas represent the total coverage of all Deep or UltraDeep (UD) fields combined.

(PSF). This effect, caused by atmospheric turbulence in ground-based observations (as well as instrumental effects from filter-specific design), will cause the light of a point-like source to be spread out or smeared in our images. The effect this will have

on galaxy images is to artificially suppress brightness levels in galaxy centers and redistribute this light to more extended radii (Sandin 2014, 2015). The HSC-SSP and CLAUDS observations have excellent seeing quantified as the full-width-half-maximum (FWHM)[1] of the PSF model (arcsecond values listed in Table 2.1), and thus provide us with some of the best quality ground-based images of galaxies available. However, we still account for the effects of instrumental PSFs on the galaxy images we use in this work through a model-fitting PSF correction procedure (see Sec. 3.1.3). The depths reached in each filter (Table 2.1) represent the limiting magnitude for each image set. The depths listed for the HSC-SSP *grizy* filters are computed as 5σ depths for point sources (Aihara et al. 2022), while the CLAUDS U-band depths are calculated as 5σ in 2-arcsecond apertures (Sawicki et al. 2019). These deep, high-resolution images enable us to detect the faint and extended light emitted from galaxies, which is critical for our investigation into stellar halo assembly.

Another substantial benefit of the combined HSC+CLAUDS datasets is the specific fields of observations (Fig. 2.2) targeted by the Deep and UltraDeep layers of the surveys. There are four main Deep fields of observation (XMM-LSS, E-COSMOS, ELAIS-N1, and DEEP2-3), along with two smaller UltraDeep fields embedded within a particular Deep field (SXDS inside XMM-LSS, and COSMOS inside E-COSMOS). These fields were chosen by HSC-SSP to specifically overlap with the footprint of the Pan-STARRS1 (Chambers et al. 2016) and SDSS (York et al. 2000) surveys (see Aihara et al. 2018 for field coordinates). These well-known extragalactic fields of observation have been thoroughly studied by other additional surveys (e.g., McCracken

[1]The full-width-half-maximum (FWHM) of a distribution is the width of the distribution (i.e. the difference between the two values of the independent variable) when the dependent variable is equal to half its maximum value.

et al. 2012; Scoville et al. 2007; Lawrence et al. 2007; Martin et al. 2005), and thus a wealth of additional data (beyond $U + grizy$ wavelength ranges) is available for galaxies in them. Some of this complementary data (specifically from the UltraVISTA (McCracken et al. 2012) and VIDEO (Jarvis et al. 2013) surveys) was utilized in the construction of the HSC+CLAUDS photometric catalogues by Desprez et al. (2023) which contain global properties of galaxies we study in this work (see Sec. 2.2),

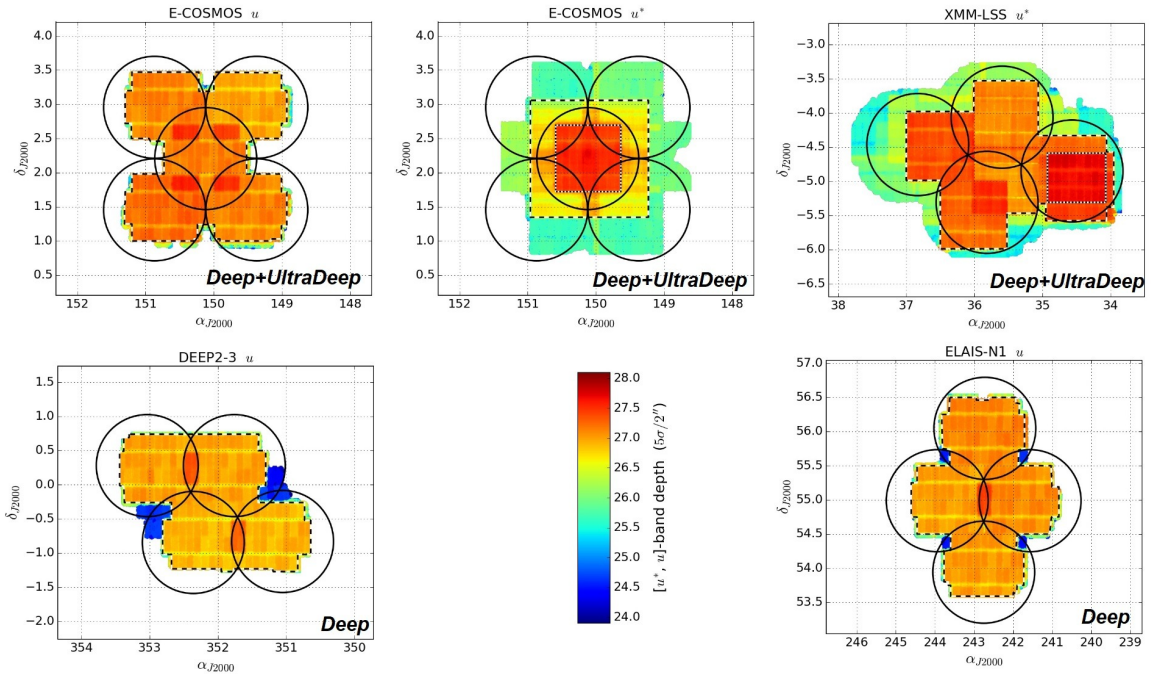

Figure 2.2. Deep and UltraDeep fields covered by the HSC-SSP (Aihara et al. 2018) and CLAUDS (Sawicki et al. 2019) surveys. Black circles represent the nominal pointings of HSC, and the coloured regions within dashed lines mark the CLAUDS coverage. Specific colours correspond to depth levels, which are 5σ depths in 2-arcsecond apertures (Sawicki et al. 2019). Figure acquired from Sawicki et al. 2019 with permission.

As the four observed fields are well separated on the sky, they sample a wide variety of galaxy environments. Observing a range of environments helps address the effect that cosmic variance (Driver & Robotham 2010) may have on our results.

Cosmic variance refers to the fact that the large-scale structure of the universe is not uniform in every direction (i.e. line of sight from Earth). One area of the sky could be probing dense cluster regions while another may be probing under-dense void or sheet regions of the cosmic web (Sousbie 2011; Driver & Robotham 2010). By analyzing observations of galaxies taken from widely separated areas on the sky, we combat this issue of cosmic variance biasing our results towards a particular type of cosmic environment or population of galaxies. Furthermore, the full areas covered by each of the Deep and UltraDeep fields (Table 2.1) are much larger than the typical sizes of individual cosmic web components (i.e. nodes, filaments, voids; e.g. Kraljic et al. 2018), which further ensures we are sampling a large number of environments.

2.1.1 Image Processing and Pipelines

The images from both datasets have been processed for scientific analysis through the image processing pipelines of both surveys (for pipeline details see Bosch et al. 2018 for HSC-SSP, and Gwyn 2008; Sawicki et al. 2019 for CLAUDS). The two surveys are structured into a tract and patch system, where a field of observation (Fig. 2.2) is divided into tracts that are then subdivided into 9 x 9 patches each. The CFHT (CLAUDS) images have been resampled to the HSC-SSP pixel scale and this tract+patch system (see Sawicki et al. 2019 for details). Each tract is an area of 1.7 deg^2 and each patch is a single 4200 x 4200 pixel image ($\sim$0.2 deg^2 with HSC+CLAUDS pixel scale of 0.168"/pixel). Every patch also overlaps by 100 pixels on each edge to ensure no galaxies are split between two images (Aihara et al. 2018; Sawicki et al. 2019). Figure 2.3 shows an example of a single patch (i.e. $\sim$0.2 deg^2

image) to illustrate the exquisite detail of these ground-based observations. The i, r, and g-band filters serve as the R-G-B colours, respectively.

Figure 2.3. Single 4200 x 4200 pixel (∼705 x 705 arcsecond) image from the HSC-SSP PDR3 observations (Aihara et al. 2022). The i, r, and g-band filters serve as the R-G-B colours, respectively. The CLAUDS datasets also contain a similar patch, as explained in Sec. 2.1.1. This image includes approximately 23,569 galaxies which reside over an extensive range of redshift ($z \sim 0 - 6$). Once we apply our stellar mass and redshift limits (Sec. 2.3) and a series of quality cuts (Sec. 2.2.1), 822 galaxies remain in our final sample used for analysis.

One important aspect of the HSC-SSP pipeline is the selection between the local or global sky subtraction methods of estimating and subtracting the contamination

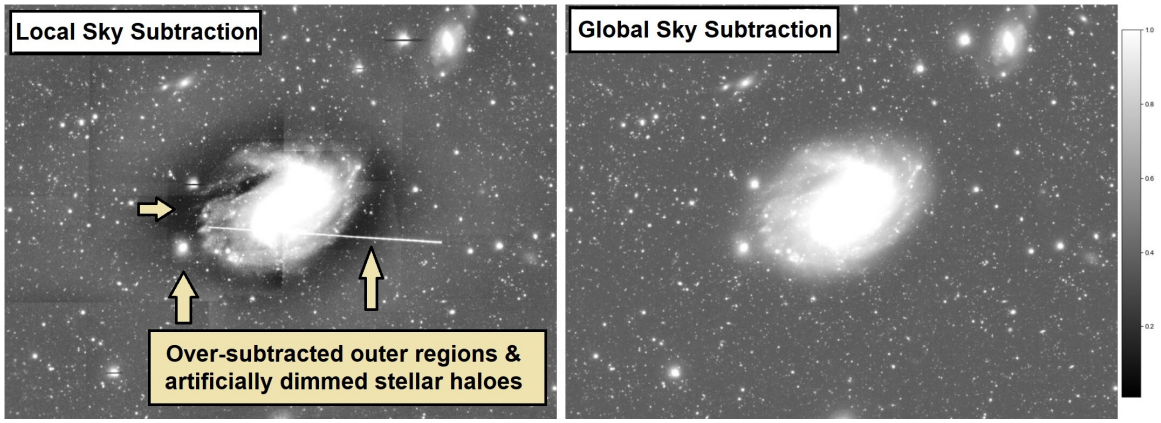

Figure 2.4. Results from the local (left) and global (right) sky subtraction procedures from the HSC-SSP PDR3 image processing pipeline (Bosch et al. 2018; Aihara et al. 2022) performed on the same galaxy image. Figure obtained from HSC-SSP PDR3 website (https://hsc-release.mtk.nao.ac.jp/doc/index.php/available-data__pdr3/).

from background emission. Figure 2.4 illustrates the effects of using either method on the same galaxy image. In the local sky subtraction method (left-hand side of Fig. 2.4), a smooth slowly-varying flux distribution is subtracted from an image. It was found by the HSC-SSP team that this was over-subtracting the light around the edges of galaxies and artificially dimming their extended regions (e.g. where yellow arrows point in Fig. 2.4).

In future releases like the PDR3 data release we use in this work, HSC-SSP added the global sky subtraction method. This method better preserves the faint light in the outer regions of galaxies by not over-subtracting the background sky emission, while suffering from longer computational times and slightly reduced detection efficiency when identifying sources. In this background subtraction routine, a large-scale empirical model of the background (i.e. an 8000 x 8000 superpixel; Aihara et al. 2022) is subtracted across the field of view for each exposure. Following this, a smaller sky frame model with smaller spatial variations than the large empirical model is gener-

ated for each filter and observation, and subtracted from the images. Finally, small superpixels (256 pixels) are used to perform masking of nearby objects to better estimate local sky residuals around individual objects (i.e. galaxies). As the goal of our study is to examine the faint stellar haloes around galaxies, we select the HSC-SSP PDR3 images that were processed through the global sky subtraction procedure for use in our work.

2.2 HSC+CLAUDS Photometric Catalogues and Sample Selection

We retrieve properties of galaxies forming our final sample from the HSC+CLAUDS photometric catalogues produced by Desprez et al. 2023 (`SExtractor`/`LePhare` versions). For all sources within these catalogues, the authors have performed object detection and photometry with the `SExtractor` (Bertin & Arnouts 1996) software and computed physical properties with `LePhare` (Arnouts & Ilbert 2011) SED fitting[2] package. Desprez et al. (2023) includes full details of the catalogues.

We use the following catalogued galaxy properties:

- **Right Ascension & Declination**: Celestial coordinates (J2000) used to locate galaxies within individual HSC+CLAUDS patches.
- **Stellar Mass ($M_\star$)**: Galaxy stellar mass (i.e. not including the dark matter

[2] *SED fitting* refers to fitting different models or templates to the observed spectral energy distribution (SED) of a galaxy, which is the distribution of flux density as a function of wavelength or frequency.

halo mass) given in units of $\log(M_\star/M_\odot)$, and calculated via `LePhare`.

- **Redshift**: Galaxy photometric redshifts calculated via `LePhare`.
- **Star Formation Rate (SFR)**: Galaxy star formation rates ($M_\odot$/year), calculated via `LePhare`.
- **Total Magnitudes ($U + grizy$)**: Total magnitudes for each of the $grizy$ filters from HSC-SSP and the u and u^* filters from CLAUDS, which have been corrected for galactic extinction due to dust within the Milky Way based on the Schlegel extinction maps (Schlegel et al. 1998).

From the HSC+CLAUDS catalogues, we retrieve an initial sample of 17,608,793 galaxies, of which 870,732 are within the stellar mass ($M_\star \geq 10^{9.5} M_\odot$) and redshift range ($0.2 \leq z \leq 1.1$) we probe in this study (ranges discussed in Sec. 2.3). In order to refine this initial sample of galaxies we perform a series of quality cuts based on additional catalogue parameters (discussed in Sec. 2.2.1 and summarized in Table 2.2).

2.2.1 Galaxy Sample Quality Cuts

To eliminate contamination from point source objects we make a cut to the `CLASS_STAR_HSC_I` parameter in the catalogue, which helps determine if any objects were misclassified as galaxies. This is performed by the star estimator tool (`CLASS_STAR`) from the `SExtractor` software package (Bertin & Arnouts 1996), which computes a probability that an object is either a point source or an extended object (i.e. a galaxy). Following the recommendation of Desprez et al. (2023) we remove any galaxies with values

above 0.9 of this parameter which ensures a robust selection of extended objects.

We apply further quality cuts in order to address the effect that image artifacts have on galaxy photometry. First, we require `MASK`=0 which eliminates galaxies that have nearby bright objects with source masks identified in their images. These masks will affect the pixels around an object causing issues during photometry (e.g. calculation of magnitudes) and can affect the photometric redshift calculated for the source (Desprez et al. 2023). In a similar vein, we require the `ST_TRAILS` parameter in the catalogue to be zero which eliminates galaxy images where satellite trails or streaks were identified.

We apply final cuts to the `SExtractor` derived magnitudes of individual galaxies. Following the recommendation of Desprez et al. (2023) we remove any galaxies whose total apparent i-band magnitude is $\geq$ 26 mag. This limit was determined based on the precision of photometric redshifts calculated by the authors, where the typical uncertainties on the photometric redshift calculations are roughly σ $\sim$0.04 at $m_i \sim$ 26, and grow larger at deeper magnitudes (redshift range of this study discussed in Sec. 2.3). Additionally, the photometry performed by two different methods during catalogue construction (i.e. `hscPipe` pipeline and `SExtractor` software), agreed with each other down to $\sim$ 26 mag. We make another cut to the `OFFSET_MAG_2s` parameter in the catalogue, which is added to the 2" aperture magnitudes in the HSC+CLAUDS catalogues to convert them to total magnitudes. Following the recommendation of Desprez et al. (2023) we use a cutoff of <-1 for this parameter to remove galaxies with less reliable magnitude measurements.

The number of galaxies remaining in our final sample after we apply these quality

cuts is 514,202. In Table 2.2 we summarize these quality cuts and how many galaxies were removed with each step. One final reduction of this sample proceeded after we attempted to extract radial surface brightness profiles from images (see Sec. 3.1 for details). Certain profile extractions failed (small portion, ∼2.5%) due to issues with the galaxy images such as artificial artifacts or masking issues (see Sec. 3.1.2).

Sample Limit / Quality Cut	**Value Range**	# **Removed**	**Galaxies Remaining**
Initial sample			**17,608,793**
Redshift limit	$0.2 \leq z \leq 1.1$	13,794,634	3,814,159
Stellar Mass limit	$M_\star \geq 10^{9.5} M_\odot$	2,943,427	870,732
`CLASS_STAR_HSC_I` cut	≤ 0.9	212,857	657,875
`OFFSET_MAG_2s` cut	<-1	58,987	598,888
`MASK` cut	=0	83,916	514,972
`ST_TRAILS` cut	=0	599	514,373
Magnitude cut	$m_i \leq 26$ mag	171	514,202
Failed profiles		13,581	500,621
Final sample			**500,621**

Table 2.2: Summary of the sample limits and quality cuts applied to the initial sample of galaxies retrieved from the HSC+CLAUDS catalogues (Desprez et al. 2023).

2.3 Stellar Mass and Redshift Range of Galaxy Sample

Galaxies in our final sample are limited to stellar masses of $M_\star \geq 10^{9.5} M_\odot$ and the redshift range of $0.2 \leq z \leq 1.1$. Figure 2.5 shows the distributions of stellar mass and photometric redshift values for our galaxy sample, divided into the star-forming (blue histograms) and quiescent (red histograms) galaxy population (separation procedure explained in Sec. 2.4).

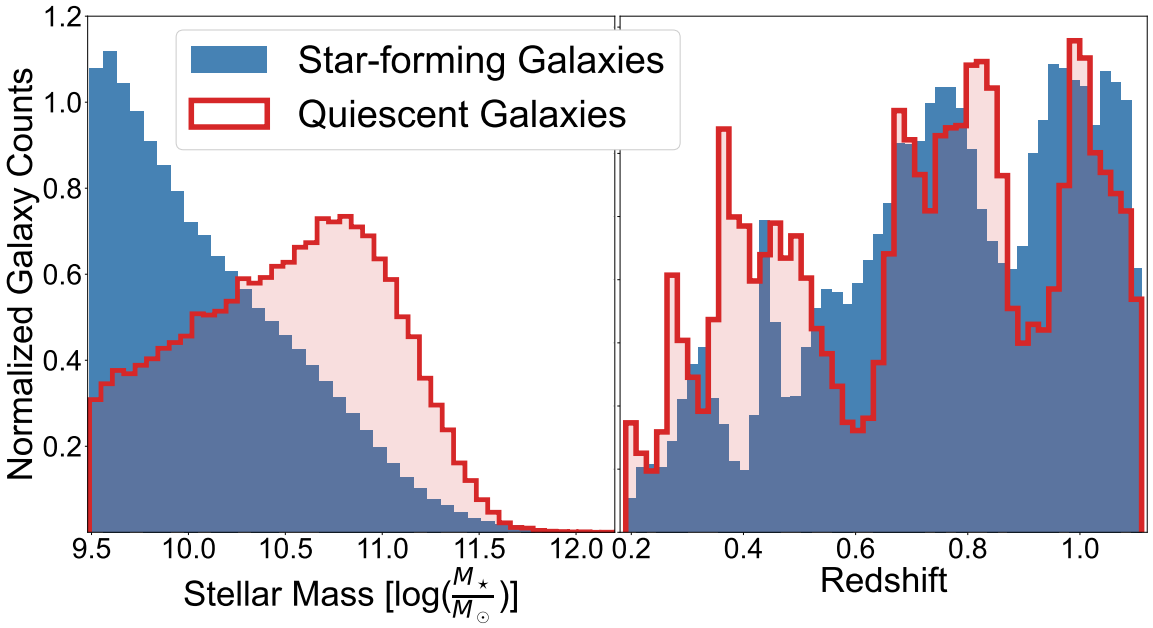

Figure 2.5. Normalized distributions of stellar mass and photometric redshift values for galaxies in our sample, divided into star-forming and quiescent galaxy populations.

Our stellar mass limit was chosen based on stellar mass completeness and the results of Chen (2019), who studied satellite galaxy number density distributions and their detection limits within the HSC+CLAUDS datasets. In all redshift ranges analyzed by Chen (2019), and in both the star-forming and quiescent galaxy population, a stellar mass cutoff at $10^{9.5} M_\odot$ ensures a completeness of at least 90%.

The lower redshift limit ($z = 0.2$) is determined by the uncertainties on the photometric redshift calculations for galaxies in our sample, which were estimated with `LePhare` in the HSC+CLAUDS catalogues (Desprez et al. 2023). With a magnitude limit of $\leq$ 26 mag (see Sec. 2.2.1), the typical uncertainties on the photometric redshift calculations are roughly $\sigma \sim 0.04$[3]. For this reason, we omit any redshifts lower

[3]These redshift uncertainties have been normalized by 1+mean(z), for details see Desprez et al. 2023.

than $z = 0.2$ as the uncertainties will become nearly as large as the redshift values.

The upper redshift limit ($z = 1.1$) is determined by the wavelength coverage of the two surveys (i.e. $U+grizy$ filters, rest-frame ∼2700-10500 Å). One reason for this is the measurement of galaxy stellar masses through SED fitting. In order to compute reliable stellar mass measurements we require emission from rest-frame visible or near-infrared wavelengths (e.g. rest-frame ∼5000-6000 Å). This emission will better trace the total stellar mass in a galaxy as it detects emission from the older and lower-mass stellar populations within a galaxy. In order to calculate accurate stellar masses beyond a redshift of $z \sim 1.1$ through SED fitting, the $U + grizy$ data would need to be complemented with longer wavelength data (Desprez et al. 2023). Additionally, a key analysis strategy adopted in our study is to track rest-frame g-band (∼5000 Å) emission in galaxies across our full redshift range (explained further in Sec. 3.2.1). At a redshift of $z \sim 1.1$ the center wavelength of the g-band filter (4754 Å, Table 2.1) is no longer captured by the reddest filter available (i.e. the HSC y-band filter).

2.4 Separating Star-Forming and Quiescent Galaxies

Galaxies in our final sample are separated into star-forming (420,011) and quiescent (80,610) galaxy populations through a NUVRK colour-colour diagram cut (Fig. 2.6). The NUVRK diagrams (Arnouts et al. 2013) make use of the rest-frame NUV (near-ultraviolet), r (visible), and Ks (near-infrared) magnitudes from the HSC+CLAUDS catalogues (Sec. 2.2). The NUV- and Ks-band magnitudes come from the Ks-filter

($\sim 18400-24500$ Å) of the VIRCAM instrument and UltraVISTA survey (McCracken et al. 2012), and the NUV filter ($\sim 1700-3000$ Å) of the GALEX instrument (Martin et al. 2005). For the galaxies in the catalogues not covered by the additional VIRCAM and GALEX data, their NUV- and Ks-band magnitudes are extrapolated through SED fitting (Picouet et al. 2023). Galaxies within the catalogues have a `STAR_FORMING` parameter which indicates their designation based on the NUVRK diagram selection (1 = star-forming, 0 = quiescent).

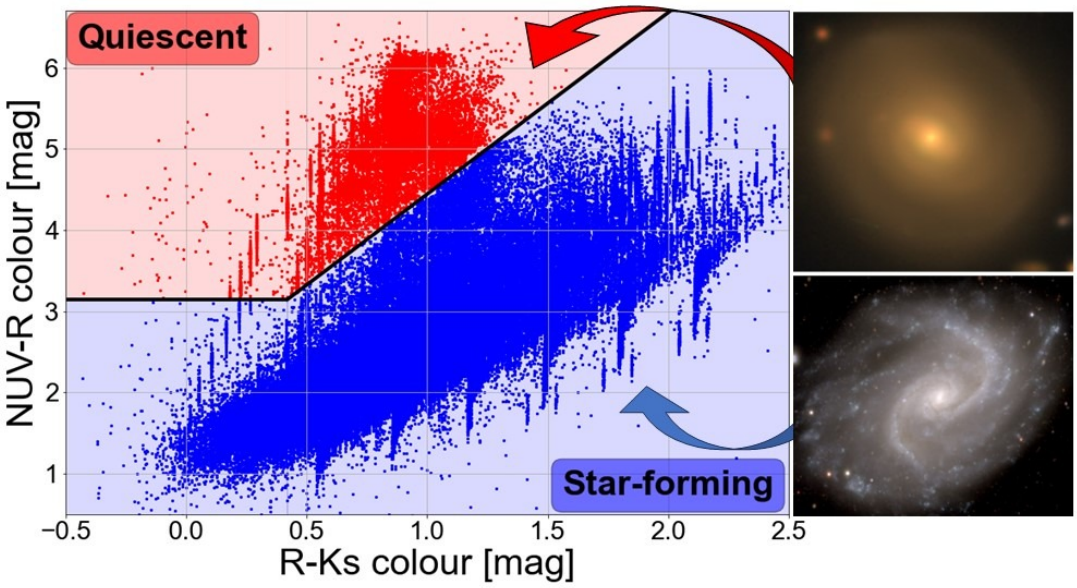

Figure 2.6. NUVRK colour-colour diagram (see Sec. 2.4) we use to split our galaxy sample into separate star-forming (blue dots) and quiescent (red dots) populations. The black line separating the two populations corresponds to a minimum density of points in this rest-frame colour-colour parameter space (calculated by Desprez et al. 2023). Two example galaxies (same from Fig. 1.2) from the HSC-SSP PDR3 observations (Aihara et al. 2022) are shown for context.

These NUVRK diagrams are similar in nature to the slightly more common UVJ diagrams (Williams et al. 2009), where different colour excesses are used as proxies for the level of star formation in a galaxy. NUVRK diagrams are better at distinguishing between the reddening effects of dust and stellar ageing than UVJ diagrams by ex-

tending further into infrared wavelengths (Arnouts et al. 2013; Moutard et al. 2018). The NUV-r colour (y-axis in Fig. 2.6) traces specific star formation rate (sSFR). This provides a way to compare the amount of emission coming from hot newly formed stars (traced by rest-frame NUV), to the emission coming from older and lower mass populations (traced by rest-frame r-band; Arnouts et al. 2013; Moutard et al. 2018, 2020). A galaxy with a very blue NUV-r colour must have had large amounts of recent star formation, in order to replenish the NUV emission required to keep average colours so blue. However, as the presence of dust can also redden these NUV-r colours, the r-Ks colour (x-axis in Fig. 2.6) is used to disentangle the effects of reddening due to stellar ageing and dust (Arnouts et al. 2013; Moutard et al. 2018, 2020). Here the r-Ks colour acts as a tracer for the infrared excess, which probes how much UV emission is being absorbed and re-emitted in the infrared wavelengths by dust. Using these characteristics a NUVRK diagram can help us distinguish between a reddened "dusty" star-forming galaxy, and a truly red quiescent galaxy (Moutard et al. 2018, 2020).

Chapter 3

Methodology

The 1D radial surface brightness profile introduced in Sec. 1.2.1 is the main tool we use to analyze the stellar haloes of galaxies in our study. Throughout Sec. 3.1 we outline our computational procedure for extracting surface brightness profiles from the images of galaxies in our HSC+CLAUDS dataset (Sec. 2.1). Before we extract profiles we perform additional image processing on the galaxy images which include source masking and background subtraction (Sec. 3.1.2), and correcting for the effects of PSFs (Sec. 3.1.3).

Throughout Sec. 3.2 we outline our strategy for analyzing the extracted surface brightness profiles including the binning of our galaxy sample (Sec. 3.2.1), and the computation of median rest-frame g-band surface brightness profiles (Sec. 3.2.2). In Sec. 3.2.3 we describe our procedure for calculating rest-frame U-g colour profiles. In Sec. 3.2.4 we compute effective radii (R_e) for galaxies in our sample in order to study how sizes have evolved over our full redshift range.

3.1 Surface Brightness Profile Extractions

In this section, we give an overview of our surface brightness profile extraction procedure. Extracting the required number of profiles becomes challenging given the large volume of our dataset (i.e. 500,621 individual galaxies imaged in multiple $U + grizy$ filters). In order to accomplish this task we make use of the python package `GalPRIME` and its `KOE` pipeline (Souchereau et al. in prep.).

The `KOE` pipeline extracts surface brightness profiles from real or simulated galaxy images via the elliptical isophote analysis method introduced in Sec. 1.2.1 (and shown in Fig. 1.5). Crucially, the pipeline is designed to work with large astronomical datasets such as our HSC+CLAUDS sample. Thanks to its multi-threading design, `GalPRIME` (and any of its pipelines or functions) can be implemented on any high-performance-computing (HPC) cluster which enables large batches of profile extractions to be completed simultaneously. We use this beneficial feature to its full extent in our study with the help of resources from ACENET and The Digital Research Alliance of Canada. Specifically, profile extraction jobs were run on 32 cores (2-4G per CPU) on the Graham and Cedar servers of ACENET, over time intervals of 24-72 hours depending on job queue congestion.

3.1.1 `GalPRIME` Overview and Configuration

The `KOE` pipeline initially requires a configuration file which stores key file directories and parameter values used throughout the extraction process (discussed here and throughout Sec. 3.1.2). The directories include a folder containing images to be pro-

cessed, and another containing an associated object catalog. For our extractions, these correspond to the individual HSC+CLAUDS patches (4200 x 4200 pixel FITS images) and HSC+CLAUDS photometric catalogues (Desprez et al. 2023). The pipeline begins by forming a list of potential objects from the provided catalogue, which can be filtered based on cuts to catalogue parameters. We limit the extractions with `KOE` only to the stellar mass and redshift range we cover in this work (see Sec. 2.3), as well as the magnitude limit of $\leq$ 26 mag discussed in Sec. 2.2.1.

After `KOE` locates a galaxy in the larger patch images (e.g. Fig. 2.3), it forms a smaller cut-out image of the galaxy. The size of this cut-out can be adjusted with the `SIZE` parameter within the configuration file of `KOE`. This `SIZE` parameter also dictates how far in radius the surface brightness profile is extracted from a given galaxy image, which is half the cut-out size.

For our extractions, we set the cut-out sizes to be 250, 300, or 400 pixels (or ∼42", ∼50", ∼67" with HSC+CLAUDS pixel scale of 0.168"/pixel) depending on the photometric redshift of a given galaxy. In our work, we split our galaxy sample into four redshift bins (see Sec. 3.2.1), and for each redshift bin we assign a different size (larger sizes for lower redshifts). The cut-out sizes we select for each redshift bin yield median surface brightness profiles that extend to a comparable physical range (i.e. ∼150±15 kpc), after converting arcseconds to kiloparsecs using the photometric redshift of a given galaxy and the `kpc_proper_per_arcmin` package from `Astropy` (Astropy Collaboration et al. 2013).

We chose cut-out sizes to be much larger than the sizes of galaxies, to ensure we detect the faintest and most extended possible stellar halo emission in the images.

This physical size range ensures all profiles have a long flat portion at the end (i.e. relatively constant surface brightness with radius) which we use in our determination of profile truncation radii (see Sec. 3.2.2). This extended radius where profiles flatten out indicates where galaxy brightness levels have blended into the background (Iodice et al. 2016, 2017).

Before we extract surface brightness profiles from individual galaxy cut-outs via `KOE`, we perform several important image processing steps beyond what was done at the survey-pipeline level (Sec. 2.1.1). These crucial steps are discussed briefly throughout the following sub-sections and include source masking and background subtraction performed through `GalPRIME` (Sec. 3.1.2), and our own procedure for subtracting the effect of PSFs (Sec. 3.1.3) using `PetroFit` (Geda et al. 2022) and `Astropy` (Astropy Collaboration et al. 2013) packages.

3.1.2 Source Masking and Background Subtraction

When extracting surface brightness profiles from galaxy images we must correct for light contamination coming from foreground and background sources, as well as the sky-subtracted background noise that remains (Li et al. 2021). This excess emission can affect the profiles we extract by artificially brightening the low surface brightness levels in outer regions of galaxies. Figure 3.1 demonstrates this effect on a simulated galaxy light profile that has been contaminated with background emission. From the offset between the red and blue profiles, it is clear we must correct for this light contamination in order to recover the true light distributions of galaxies.

We implement the source masking procedure within `GalPRIME` to block out the

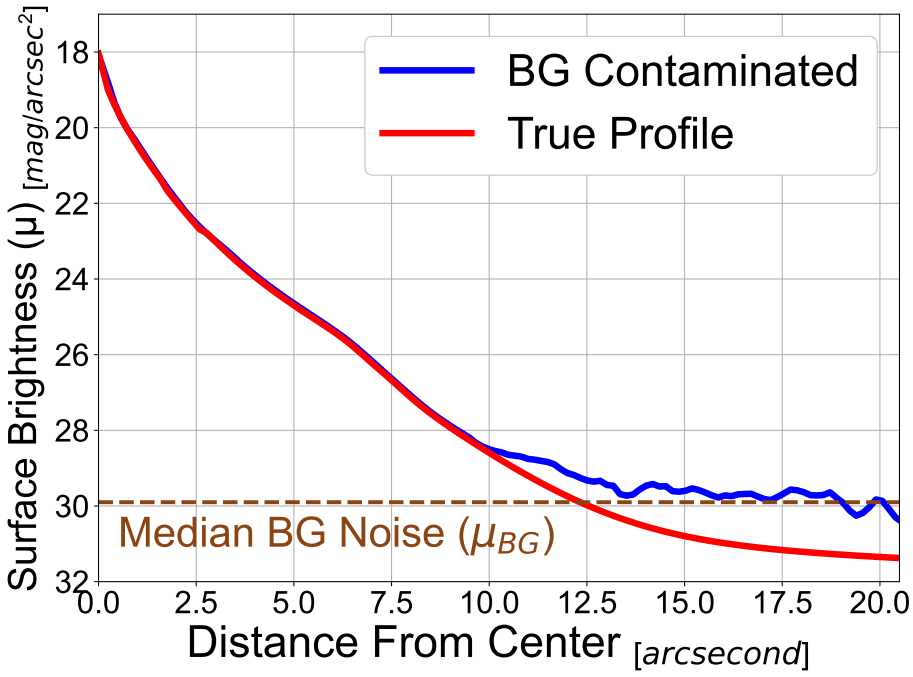

Figure 3.1. Example of how background noise contaminates the outer regions of galaxy surface brightness profiles. The true profile (red) shown here is extracted from a simulated galaxy model (`Astropy Sersic2D`, 2-component model), while the background contaminated profile is shown in blue. Without subtracting the contribution from the background, we will not recover the true light distribution of galaxies, particularly in their outer stellar halo regions.

light from nearby objects in the foreground or background of the individual images of galaxies. To subtract the background emission from images we use the 2D background subtraction procedure (`JW2D`) within `GalPRIME`. We discuss each of these procedures briefly below, and in Fig. 3.2 we illustrate their application to a galaxy image from our sample.

Starting with a raw galaxy cutout (panel A, Fig. 3.2), an initial mask is created for the target galaxy with a `Tophat2DKernel` from `Astropy` (Astropy Collaboration et al. 2013) in order to omit it from the estimation of background levels and further source masking (panel B, Fig. 3.2). This mask is smoothed out by convolving it with a `Gaussian2DKernel` with a width of 2.

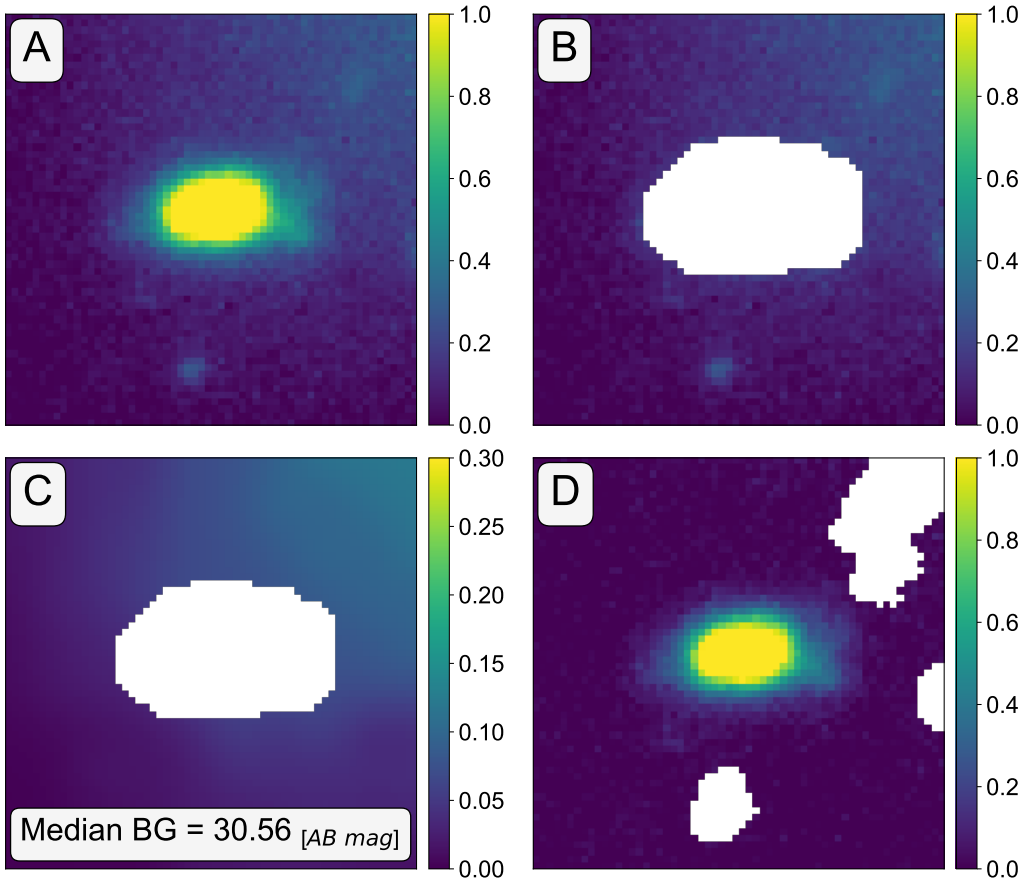

Figure 3.2. Illustration of the source masking and 2D background subtraction procedures applied to galaxy cutouts in `GalPRIME` (explained throughout Sec. 3.1.2). **Panel A:** Original raw galaxy cutout. **Panel B:** Mask created for target galaxy. **Panel C:** 2D background levels estimated from the masked image. **Panel D:** Final background-subtracted galaxy image with foreground and background objects masked. The galaxy shown here is from our star-forming sample ($M_\star = 10^{10.86} M_\odot$ and $z = 0.638$), and the image is taken with the HSC-i filter.

Following this, 2D background subtraction is performed using the `Background2D`[1] package from `Astropy`. This technique performs well when the background or noise levels vary across an image (Astropy Collaboration et al. 2013), as they typically do in real galaxy images (e.g. panel C, Fig. 3.2). In this method, a 2D image of the background levels is created (panel C, Fig. 3.2) by generating a mesh grid over

[1]Detailed code documentation for `Background2D` can be found at https://photutils.readthedocs.io/en/stable/api/photutils.background.Background2D.html.

the image (omitting the source mask of the target object) and computing the median background levels within each box (mesh). The median background levels are obtained using the `sigma_clipped_stats`[2] package from `Astropy`, with $\sigma = 3$ and default settings. This function computes the median background brightness level across all pixels, removes (clips) any pixels that are above or below the background level by some number of standard deviations (i.e. $\sigma = 3$), then recalculates a new median background level (for default 5 iterations). After background levels are calculated in each box, the 2D background image is median filtered to help suppress local over- or underestimations due to overly bright sources in a particular box. Both the box size and filter window size are adjustable parameters within the configuration file of `GalPRIME` (i.e. `BOX_SIZE` and `FILTER_SIZE`), for which we use 41 and 6. These values were determined by Souchereau et al. (in prep.) who tested the `JW2D` background subtraction procedure using simulated galaxies and intrinsic HSC+CLAUDS backgrounds and found they produced optimal results.

Next, the procedure creates a segmentation map of all other sources in the image, where pixels measured to be some number of standard deviations (`NSIGMA`) above the sigma-clipped median background level are flagged as belonging to an object. An object must then have a certain minimum number of flagged pixels that are connected (`NPIX`), in order to be classified as a source that needs masking. All unique sources identified in the segmentation map then have an initial mask created by setting the pixel values to *nan* (panel D, Fig. 3.2), and these masks are smoothed out using a `Gaussian2DKernel` with an adjustable width (`GAUSS_WIDTH`).

[2]Full documentation for `sigma_clipped_stats` found at: https://docs.astropy.org/en/stable/api/astropy.stats.sigma_clipped_stats.html.

The masking routine in `GalPRIME` can be adjusted to be more aggressive, by tuning the three parameters explained here (i.e. `NSIGMA`, `NPIX`, `GAUSS_WIDTH`). The values used for these parameters are important as overly aggressive masking can lead to poorer profile extraction performance over a large sample, where overly large source masks interrupt the isophote fitting process and profiles result in mostly *nan* values. We use 1, 11, and 2 for `NSIGMA`, `NPIX`, and `GAUSS_WIDTH`, respectively. These values were determined by Souchereau et al. (in prep.) during testing of `GalPRIME` and were found to produce optimal results with the HSC+CLAUDS datasets.

3.1.3 Modelling and Subtracting the Effect of the PSF

An important factor to consider when analyzing the outer regions of galaxy images is the redistribution of light caused by filter-specific point-spread functions (PSF). The effect of the PSF will suppress the central surface brightness levels of a galaxy and redistribute this light out to larger radii (Trujillo et al. 2001b; Sandin 2014, 2015; Borlaff et al. 2017). Since galaxy outskirts are regions of low surface brightness, this smearing of light from interior to outer regions can have a significant effect on the outer portions of surface brightness profiles and therefore our analysis of extended stellar halo regions (Szomoru et al. 2012; Sandin 2015; Borlaff et al. 2017).

We correct for PSF-related effects through a forward-modelling procedure, where a PSF-convolved galaxy model is fit to an original raw galaxy image in order to isolate and subtract the effect of the PSF. This method has been tested and used in similar studies that investigated stellar haloes (e.g., Trujillo & Bakos 2013; Trujillo & Fliri 2016; Gilhuly et al. 2022) or galaxy surface brightness profiles in general (e.g.,

Szomoru et al. 2010, 2012; Borlaff et al. 2017). Similar to previous studies, throughout our text we will refer to this forward-modelling PSF correction procedure as a *PSF deconvolution* for simplicity, keeping in mind that a true mathematical deconvolution is not being applied[3].

Our computational implementation of this method is performed by various functions from the `Astropy` (Astropy Collaboration et al. 2013) and `PetroFit` (Geda et al. 2022) python packages. After we perform source masking and background subtraction on a galaxy image (Sec. 3.1.2), we use galaxy coordinates (right ascension and declination) to search a catalogue of filter-specific PSF models to find the closest matching model in terms of position on the sky. We find the closest PSF model because the smearing effect induced by PSFs can vary with position. We obtain the PSF catalogues for the *grizy* filters from the HSC-SSP PDR3 (Aihara et al. 2022) PSF Picker[4] tool. We obtain the CLAUDS U-band PSF models from George (2020) which were created using `PSFEx` (Bertin 2011).

To each PSF model, we fit a combination of `Astropy` models in order to be able to extend the original model to a larger size. For this deconvolution technique to be successful the PSF model must be comparable in size to the galaxy image (de Jong 2008). The HSC+CLAUDS $U + grizy$ PSF models initially start as 42 x 42 pixel images, and we model and extended these to match a given galaxy cutout size during each profile extraction. The specific combination of models we use includes

[3]The deconvolution terminology arises from the fact that images of galaxies have been *convolved* with the filter PSF models, and this correction procedure then subtracts the effect of the convolution.

[4]PSF Picker can be found at the HSC-SSP PDR3 (Aihara et al. 2022) website: https://hsc-release.mtk.nao.ac.jp/psf/pdr3/.

a `Moffat2D` and two `Gaussian2D` models, as they produce the best fit and smallest residuals for all $U + grizy$ filters. Figure 3.3 demonstrates the results of the three-component model fit (residuals in right-hand column) to the i-band filter of HSC-SSP and u-band filter from CLAUDS (remaining filters performed as well as those shown).

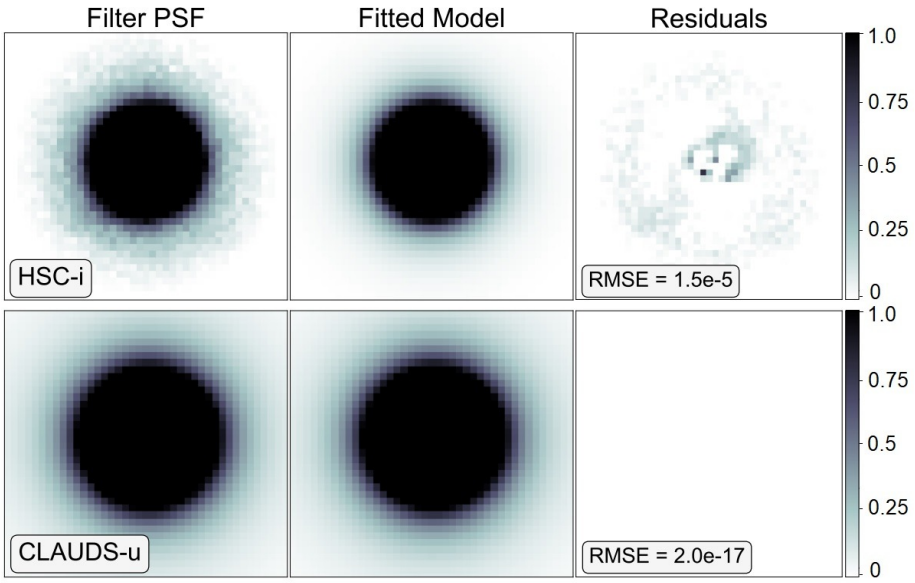

Figure 3.3. Results of our three-component model fit to the initial filter PSF models from the HSC-SSP & CLAUDS datasets. The components are a combination of `Astropy` 2D models, specifically a `Moffat2D` and two `Gaussian2D` models. The remaining $grzy$ filters performed the same as the HSC-i results shown here. See sec. 3.1.3 for details.

Next, we create a simulated galaxy model (for each galaxy separately) using the `Sersic2D`[5] package from `Astropy`. We make two-component Sérsic models for the fitting process because they performed best during the testing of our deconvolution procedure (tests discussed below). We convolve this galaxy model with an extended PSF model and fit it to the original observed galaxy image using the `fit_model` function from `PetroFit`. This fit is improved through iterations using new Sérsic model

[5]Detailed documentation for `Sersic2D` can be found at https://docs.astropy.org/en/stable/api/astropy.modeling.functional_models.Sersic2D.html

parameters until incremental improvements fall below an acceptance[6] level of 10^{-9}. This deconvolution technique is insensitive to the specific Sérsic parameters used for the model (Tal & van Dokkum 2011; Szomoru et al. 2010), and so we allow `PetroFit` to select whichever combination of model parameters best fits the data (regardless of whether these parameter combinations correspond to physical components such as disks or bulges).

Once the procedure converges to the best-fit solution, we subtract the PSF-convolved model from the original observed galaxy image to produce residuals which capture anything important missed by the fitting (e.g., irregular morphology, tidal feature). We add these residuals to the underlying (non-convolved) galaxy model that was created, to produce the final "deconvolved" galaxy image we use for brightness profile extraction. The operations performed are summarized as

$$Residuals = Original\ Raw\ Galaxy\ Image - PSF{*}Convolved\ Model, \tag{3.1}$$

$$Deconvolved\ Image = Underlying\ Model + Residuals, \tag{3.2}$$

which are equivalent to Eq. 5 and 6 from Borlaff et al. 2017.

In order to ensure our computational implementation of this PSF deconvolution technique is robust, we perform a series of tests using simulated galaxy images. By using simulated galaxy models instead of real HSC+CLAUDS observations, we know the initial underlying galaxy light profile prior to any influence of the PSF. This "ground truth" profile can then be compared to the final deconvolved profile we obtain, in

[6]The acceptance level here refers to the *acc* parameter from `Astropy`'s LevMarLSQFitter, which is utilized in `PetroFit`'s `fit_model` function. Documentation found here: https://docs.astropy.org/en/stable/api/astropy.modeling.fitting.LevMarLSQFitter.html

order to measure how successful the deconvolution process was. The performance of the deconvolution is analyzed visually through residual plots and numerically by computing the root-mean-squared errors[7] (RMSE) of the fits.

To perform the tests we create 5000 simulated galaxies using two `Sersic2D` components, based on structural parameters from the 2D bulge+disk decompositions of SDSS galaxies by Simard et al. (2011)[8]. We then add a Gaussian noise distribution to the simulated galaxy models to serve as the background noise following a similar methodology as Borlaff et al. (2017). Finally, we convolve the simulated and noisy galaxy images with one of the $U + grizy$ PSFs, to produce a simulated galaxy image that resembles what we may receive from HSC (Subaru) or MegaCam (CFHT).

With these processed simulated images, we perform the same deconvolution procedure described at the beginning of this subsection (i.e. steps summarized in Eq. 3.1 and 3.2) for all simulated galaxies. We repeat these tests three times using 1, 2, and 3-component Sérsic models during the fitting process, and with each test, we save the RMSE between the deconvolved and original input profile. Figure 3.4 shows an example of the results of one test and the profiles that were obtained. From the difference between the deconvolved profile (blue) and PSF-contaminated profile (red) at recovering the green profile (ground truth), we can see the benefit of correcting for the effects of the PSF.

In Fig. 3.5 we present the results of the entire set of simulation tests for all

[7]The root-mean-square error (RMSE) is the standard deviation of the residuals, and represents the average difference between a set of predicted values and measured data points.

[8]The specific parameter catalogue retrieved from Simard et al. (2011) is the free n_b bulge + disk decompositions.

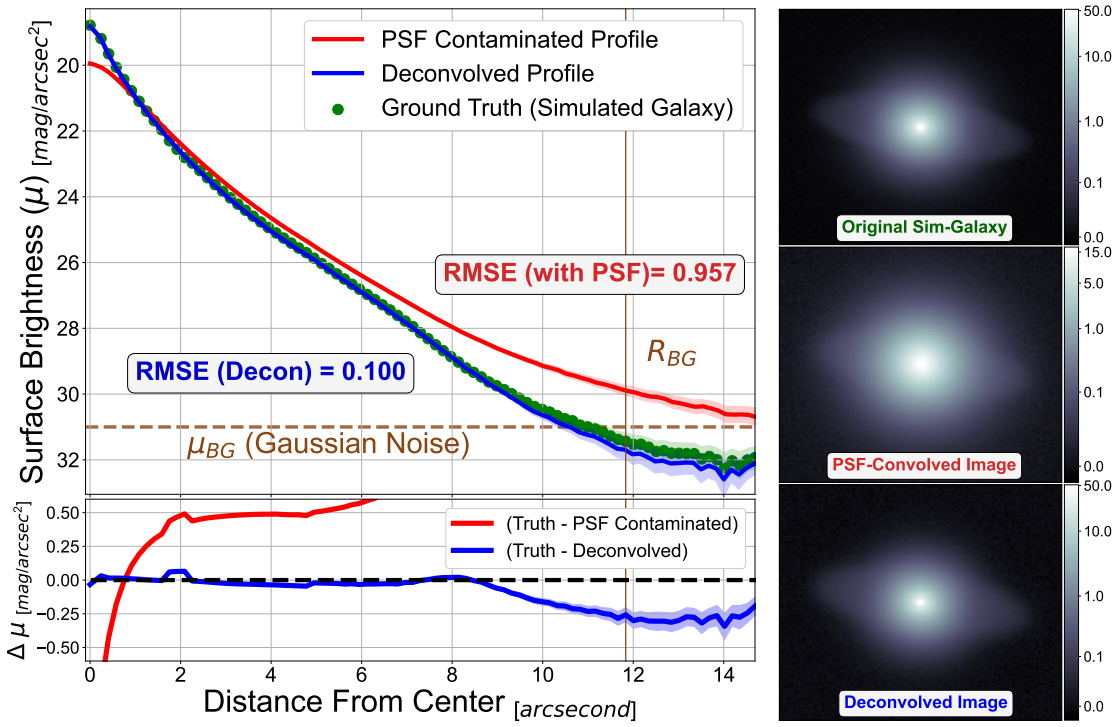

Figure 3.4. Example result from the simulation-based testing of our PSF-correction procedure (discussed in Sec. 3.1.3). The surface brightness profiles on the left are extracted from the images with the same coloured labels on the right. The model galaxy is a 2-component `Sersic2D` model as described in Sec. 3.1.3. The bottom plot displays the residuals of subtracting the PSF contaminated and corrected (*deconvolved*) profile from the ground truth, with RMSE values reported in the top plot. PSF filter used for this specific test is HSC i-band. Shaded areas surrounding profiles indicate the 1σ errors on the profiles.

simulated galaxies we created. The 2D histograms show how RMSE between the deconvolved profile and ground truth profile varied with different galaxy properties or input parameters (obtained from the catalogue of Simard et al. 2011). The results shown in the 2D histograms represent those obtained when a 2-component Sérsic model was used during the fitting portion of the deconvolution process, as it was the best-performing model and the one we use with our main results. The median RMSE obtained when we used a 1 and 3-component model is shown in the text box in Fig. 3.5. We can see that our PSF correction procedure performs very well at recovering the true light distributions across a large sample of galaxies, resulting in a median

RMSE of $\sim$ 0.092. Without the PSF correction, the extracted brightness profiles would be fairly offset from the true light distributions ($\sim$1 mag/arcsec^2, median RMSE = 0.987). From the 2D histograms, we can see that there is a small trend toward higher RMSE values for elliptical galaxies (i.e. higher bulge Sérsic indexes and g-band bulge fractions), and also for smaller galaxy sizes (R_e) regardless of population-type.

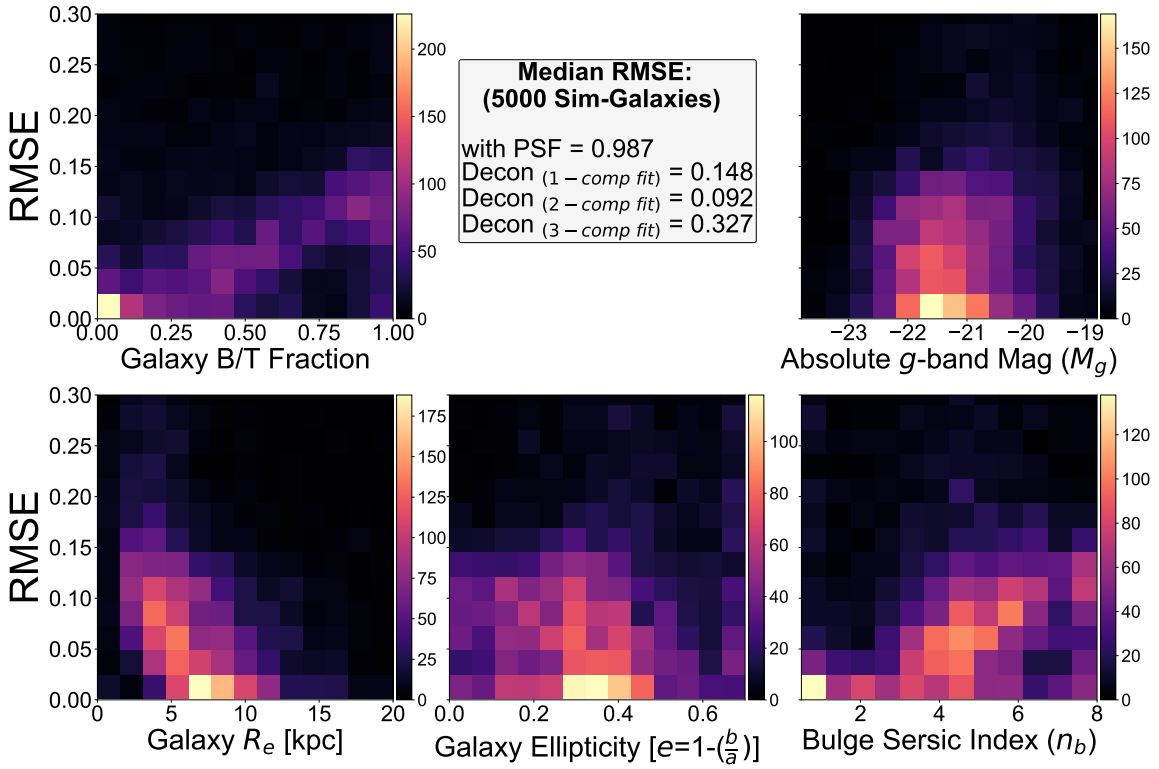

Figure 3.5. Results of the simulation-based tests of our PSF correction procedure (or *deconvolution* as discussed in Sec. 3.1.3). The 2D histograms show RMSE vs. input galaxy properties (obtained from the catalogue of Simard et al. 2011). The parameters shown are the g-band bulge fraction (B/T, top left), absolute g-band magnitude (top right), the galaxy size (R_e, bottom left), ellipticity (bottom center), and the bulge Sérsic index (bottom right). The results in the 2D histograms represent those using a two-component `Sersic2D` model for the fitting during the deconvolution procedure (i.e. the best-performing model and the one chosen for use in our main results). The statistics obtained from using different models or no correction at all are displayed in the central text box. Results here are from tests using HSC i-band filter PSF. Other $U + grzy$ filters performed the same due to the similar fits achieved during the PSF modelling and extension (Sec. 3.1.3).

3.1.4 Additional Profile Adjustments and Unit Conversions

Before proceeding to the analysis of our extracted surface brightness profiles, we correct for cosmological surface brightness dimming ($\propto 1+z^3$ when using AB magnitudes; see derivations in the appendix of Whitney et al. 2020). We also convert the extracted quantities (i.e. pixels and intensities) to physical units. Recall the x-axis of these brightness profiles represent the radial distance from the galaxy center measured along the semi-major axis (Sec. 1.2.1). They are initially extracted in units of pixels, which we then convert to arcseconds using the HSC+CLAUDS pixel scale (0.168 "/pixel), and then into units of kiloparsecs (kpc) using the `kpc_proper_per_arcmin` package (Sec. 3.1.1).

The brightness arrays of the profiles are converted from extracted intensities (I, counts per pixel) into surface brightness units (μ, magnitudes/arcsecond^2) via

$$\mu(I) = -2.5 \log_{10}\left(\frac{I}{A_{pix}^2}\right) + Z_P, \tag{3.3}$$

where A_{pix} is the pixel scale and Z_P refers to the instrument-specific zero-point magnitude offset (27 mag for HSC-SSP, 30 mag for CLAUDS), used to convert values into the AB magnitude system. We also make a second surface brightness array for all profiles in units of $L_\odot$/pc^2 (denoted Σ here simply to distinguish from values in μ units), by converting the magnitudes/arcsecond^2 values (μ) using

$$\Sigma_\lambda(M_{\lambda\odot}, \mu_\lambda) = 10^{0.4(M_{\lambda\odot}+21.572-\mu_\lambda)}, \tag{3.4}$$

where $M_{\lambda\odot}$ represents solar absolute magnitude, and the 21.572 value results from the conversion from arcseconds to parsecs (i.e. distance modulus formula; e.g., Sipols

& Pavlovich 2020). The (λ) subscripts in Eq. 3.4 highlight that this conversion is wavelength dependent and we require a different absolute solar magnitude value for each $U + grizy$ band (obtained from Willmer 2018).

3.2 Profile Analysis Strategy and Additional Data Products

3.2.1 Binning of Galaxy Profiles

In order to study trends in the size growth and stellar mass assembly of different galaxy populations, we divide our galaxy sample into smaller bins based on stellar mass, redshift, and population type (i.e. star-forming or quiescent, Sec. 2.4).

We create our redshift bins based on the decision to track rest-frame g-band emission in galaxies throughout the full redshift interval. Emission at these wavelengths (∼4100-5500 Å, Table 2.1) is a good tracer of the total stellar mass within a galaxy, as the emission from older and lower-mass stellar populations dominates at these wavelengths (Bruzual & Charlot 2003; Moutard et al. 2018; Huang et al. 2018a). This emission provides a detailed look into the stellar halo regions of galaxies, and a more accurate analysis of their stellar mass assembly histories (Huang et al. 2018a).

In order to track the rest-frame g-band emission across our full redshift range, galaxy images in different filters ($U + grizy$) are used to shift observed wavelengths[9] back into rest-frame g-band range. For example, for a galaxy at a redshift of $z \sim 0.24$

[9]Calculation for wavelength shift due to cosmological redshift: λ_{obs}=$\lambda_{emit}(1 + z)$.

rest-frame g-band emission corresponds to light coming from a r-band image. For a galaxy at a redshift of $z \sim 0.54$, rest-frame g-band emission instead corresponds to light coming from an i-band image. When deciding redshift bin intervals we also ensure that there are no galaxies in a given redshift bin where a single filter covers both rest-frame g-band ($\sim$5000 Å) and U-band ($\lesssim$4000 Å) emission. This is to avoid overlap when constructing rest-frame U-g colour profiles (see Sec 3.2.3). Table 3.1 shows the exact redshift bins we create and the number of galaxies contained in each. The four specific filters used for the rest-frame g-band tracking process are the r, i, z, and y-band images (going from low to high redshift bins).

We also divide galaxies into four separate stellar mass bins (listed in Table 3.1). We chose specific stellar mass bin limits to align with previous works in the literature and facilitate easy comparisons of results. For example, in Sec. 5.4 we present a comparison with the works of van Dokkum et al. (2010) and Conselice et al. (2022) in order to discuss the stellar mass assembly of massive (i.e. $M_\star \geq 10^{11} M_\odot$) galaxies.

Another influential factor in our determination of stellar mass bins is the *pivot mass* (M_p) that some studies have found when fitting galaxy size-stellar mass relations (e.g., Lange et al. 2015; Mowla et al. 2019a; Kawinwanichakij et al. 2021; Damjanov et al. 2022a). This pivot mass (typically found to be $M_p \sim 10^{10.5\pm0.5} M_\odot$) marks the transition into a steeper size-stellar mass relation slope for more massive galaxies (e.g., Naab et al. 2009; Trujillo et al. 2011; Mowla et al. 2019a; Kawinwanichakij et al. 2021). The explanation for the steeper slopes is usually attributed to an increased influence from ex-situ related assembly, which is also predicted by galaxy simulations in the form of higher ex-situ fractions above the pivot mass (e.g., Rodriguez-Gomez et al. 2016; Tacchella et al. 2019; Huško et al. 2022; Davison et al. 2020). We investigate

the link between the pivot mass range and ex-situ driven assembly in galaxies, by constructing two stellar mass bins on either side of the pivot mass. We refer to those bins as *low-mass* ($10^{9.5} M_{\odot} \leq M_{\star} < 10^{10.5} M_{\odot}$) and *high-mass* ($M_{\star} \geq 10^{10.5} M_{\odot}$) galaxies throughout the remainder of this text. Table 3.1 lists all four stellar mass bin intervals and the number of galaxies contained in each.

Stellar Mass & Redshift Bin	**Quiescent**	**Star-forming**	**Total**
0.2≤ z <0.35	**6891**	**27693**	**34584**
9.5≤ $M_{\star}$ <10	1492 (21.6%)	15766 (56.9%)	17258 (49.9%)
10≤ $M_{\star}$ <10.5	2095 (30.4%)	8546 (30.8%)	10641 (30.7%)
10.5≤ $M_{\star}$ <11	2607 (37.8%)	3129 (11.3%)	5736 (16.6%)
11≤ $M_{\star}$	704 (10.2%)	252 (1%)	956 (2.8%)
0.35≤ z <0.7	**29639**	**126871**	**156510**
9.5≤ $M_{\star}$ <10	4416 (14.9%)	59719 (47.1%)	64135 (41.0%)
10≤ $M_{\star}$ <10.5	6983 (23.5%)	39210 (30.9%)	46193 (29.5%)
10.5≤ $M_{\star}$ <11	11963 (40.4%)	23061 (18.2%)	35024 (22.4%)
11≤ $M_{\star}$	6277 (21.2%)	4881 (3.8%)	11158 (7.1%)
0.7≤ z <0.9	**24537**	**120621**	**145158**
9.5≤ $M_{\star}$ <10	4435 (18.1%)	57294 (47.5%)	61729 (42.5%)
10≤ $M_{\star}$ <10.5	6117 (24.9%)	35114 (29.1%)	41231 (28.4%)
10.5≤ $M_{\star}$ <11	8614 (35.1%)	20542 (17.0%)	29156 (20.1%)
11≤ $M_{\star}$	5371 (21.9%)	7671 (6.4%)	13042 (9.0%)
0.9≤ z <1.1	**19536**	**144826**	**164362**
9.5≤ $M_{\star}$ <10	5427 (27.8%)	71325 (49.3%)	76752 (46.7%)
10≤ $M_{\star}$ <10.5	6945 (35.5%)	41322 (28.5%)	48267 (29.3%)
10.5≤ $M_{\star}$ <11	5235 (26.8%)	22161 (15.3%)	27396 (16.7%)
11≤ $M_{\star}$	1929 (9.9%)	10018 (6.9%)	11947 (7.3%)
Full Sample	**80610**	**420011**	**500621**

Table 3.1: Full sample of star-forming and quiescent galaxies studied in this work, broken down into the stellar mass ($M_{\star}$ is in units of $\log[M_{\star}/M_{\odot}]$) and redshift bins outlined in Sec. 3.2.1. The percentiles in brackets within each stellar mass bin represent the fraction of galaxies contained in that stellar mass bin out of the total contained in a single redshift range (bolded rows above).

3.2.2 Median Surface Brightness Profiles and Truncation

In this work, we are interested in studying galaxy assembly and stellar halo buildup on a population level. Therefore, rather than studying individual galaxy light profiles, we compute the median rest-frame g-band surface brightness profile (Fig. 3.6) for each galaxy bin (i.e. bins from Table 3.1) in order to study median trends across different galaxy sub-populations. Median profiles are representative of the majority of individual profiles for a given galaxy sub-population (e.g. the red profile traces the densest part of grey profiles in Fig. 3.6), where the scatter in individual profiles can provide us information on the different assembly histories of galaxies in each bin (i.e. sub-population). Using a median profile over a mean profile is beneficial as the median is more robust against outliers (e.g. brightest or faintest grey profiles in Fig. 3.6).

We compute two different sets of uncertainties on these median surface brightness profiles. The first set is bootstrapped uncertainties on the median profile calculated via the `resample` package from `Scikit-learn` (Pedregosa et al. 2012). This bootstrap method simply refers to sampling with replacement, where 10,000 bootstrapped samples and median profiles were computed and the standard deviation of that distribution is used as the bootstrapped error (i.e. 1σ) on the median profile. These bootstrapped errors represent the true statistical measurement errors on the median profiles and are very small (e.g. roughly the width of the median profile in Fig. 3.6). The other set of uncertainties we calculate is percentiles (16/84%), which are more representative of the spread in a distribution of galaxy profiles within a given sub-population rather than a measurement error.

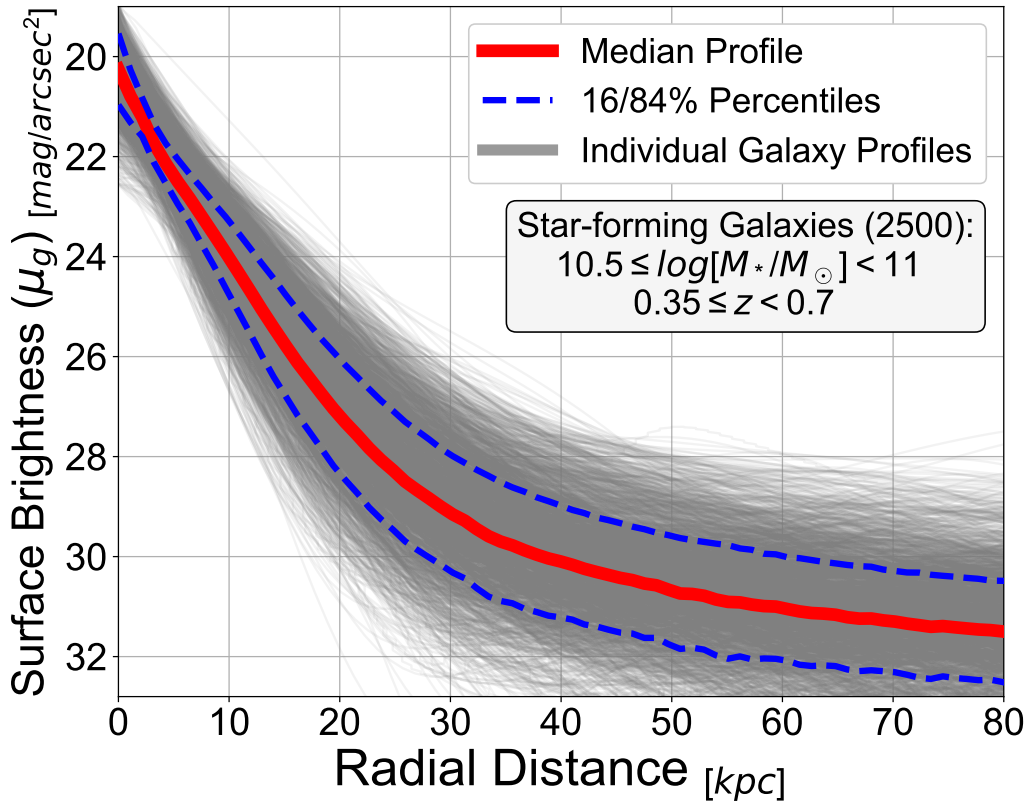

Figure 3.6. Example of a median surface brightness profile (red line) calculated from a sub-sample of 2500 individual star-forming galaxy profiles (grey lines), with their stellar mass and redshift range listed in the grey text box. The dashed blue profiles represent the 16/84 percentiles, while the width of the median profile itself demonstrates the typical bootstrapped errors on the median profiles.

To truncate the median surface brightness profiles, we follow a similar methodology as Iodice et al. (2016, 2017, 2019). In this truncation method, we use a limiting profile gradient to define a truncation radius where the light profile flattens out (i.e. has relatively constant surface brightness with increasing radius), as the galaxy light blends into the background level. Figure 3.7 demonstrates this process with an example median rest-frame g-band surface brightness profile (left), and the corresponding profile gradient as a function of radial distance on the right. To determine the truncation radii (R_{lim}) for our median surface brightness profiles, we find the radius where the profile gradient reaches its minimum for at least three successive indices in the

data arrays (to account for random fluctuations).

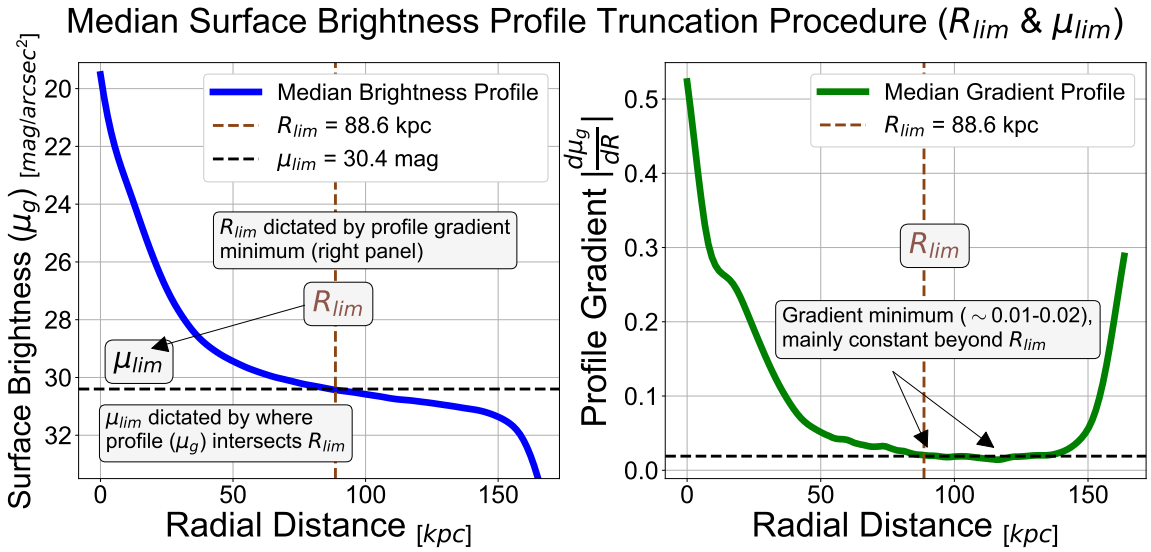

Figure 3.7. Illustration of the truncation procedure for our median rest-frame g-band surface brightness profiles. A median surface brightness profile is shown on the left (blue), with the corresponding gradient profile (i.e. gradient as a function of radius from galaxy center) shown on the right (green). Explanations for the determination of (R_{lim}) and (μ_{lim}) are summarized in the grey text boxes, and discussed further throughout Sec. 3.2.2.

We then define the surface brightness limit (μ_{lim}) as the surface brightness value of the profile at R_{lim}. The specific surface brightness limits we reach vary between our redshift bins, where profiles are limited to 30.92, 31.03, 31.52, and 31.67 mag/arcsecond^2 for the high to low redshift bins respectively (Table 3.1). This is due to the brightness level of the background, and the use of different $U + grizy$ filters (which have different depths, Table. 2.1) to track rest-frame g-band emission across redshift (Sec. 3.2.1). Nevertheless, we are able to reach very low surface brightness levels across our entire redshift range ($\sim$ 31 mag/arcsec^2), which is important for the detection of extended stellar material and the analysis of stellar halo assembly (Trujillo & Fliri 2016).

3.2.3 Median Rest-Frame U-g Colour Profiles

As discussed in Sec. 1.2.1, radial colour profiles provide an additional way to study galaxies and their stellar halo assembly (e.g., Huang et al. 2018a; Hirschmann et al. 2015; Buitrago et al. 2017). Following the same technique used to construct our rest-frame g-band surface brightness profiles (Sec. 3.2.1), we use galaxy images in different $U + grizy$ filters to shift observed wavelengths into the rest-frame U-band regime ($\sim$3000 Å) and extract rest-frame U-band surface brightness profiles. The specific filters used for this purpose for our four redshift bins are the U, g, and r-band filters for the low to high redshift bins respectively[10].

With the rest-frame U- and g-band surface brightness profiles, we construct rest-frame U-g colour profiles for a large portion ($\sim$76.5%) of our final sample. The reason for not extracting 100% of the sample is that not all galaxies had images or successful profile extractions in the rest-frame U-band. In order to understand if this missing portion introduces any bias in our results, we perform a series of Kolmogorov-Smirnov tests (using `kstest` package from `SciPy` Virtanen et al. 2020) on the distributions of certain galaxy properties between the two samples (i.e. those galaxies with and without successful colour profile extractions). We found that there is a small bias towards missing faint, low-mass, and red-coloured galaxies (i.e. quiescent, or reddened star-forming galaxies such as edge-on disks).

As with the rest-frame g-band light profiles, we compute the median U-g colour profile for each galaxy bin (bins from Table 3.1) as well as bootstrapped errors on the

[10]For reference, the four redshift bins are $(0.2 \leq z < 0.35)$, $(0.35 \leq z < 0.7)$, $(0.7 \leq z < 0.9)$, and $(0.9 \leq z \leq 1.1)$.

median colour profile. Fig. 3.8 shows an example of a median *U-g* colour profile and bootstrapped errors (blue and green lines) for a particular sub-sample of galaxies. Fig. 3.8 also highlights the variation in individual colour profiles amongst a given sub-population of galaxies (i.e. the spread in the distribution of grey profiles). This large variation is very similar to the variation seen in the light profiles in Fig. 3.6, demonstrating the need for computing median colour profiles to study population trends.

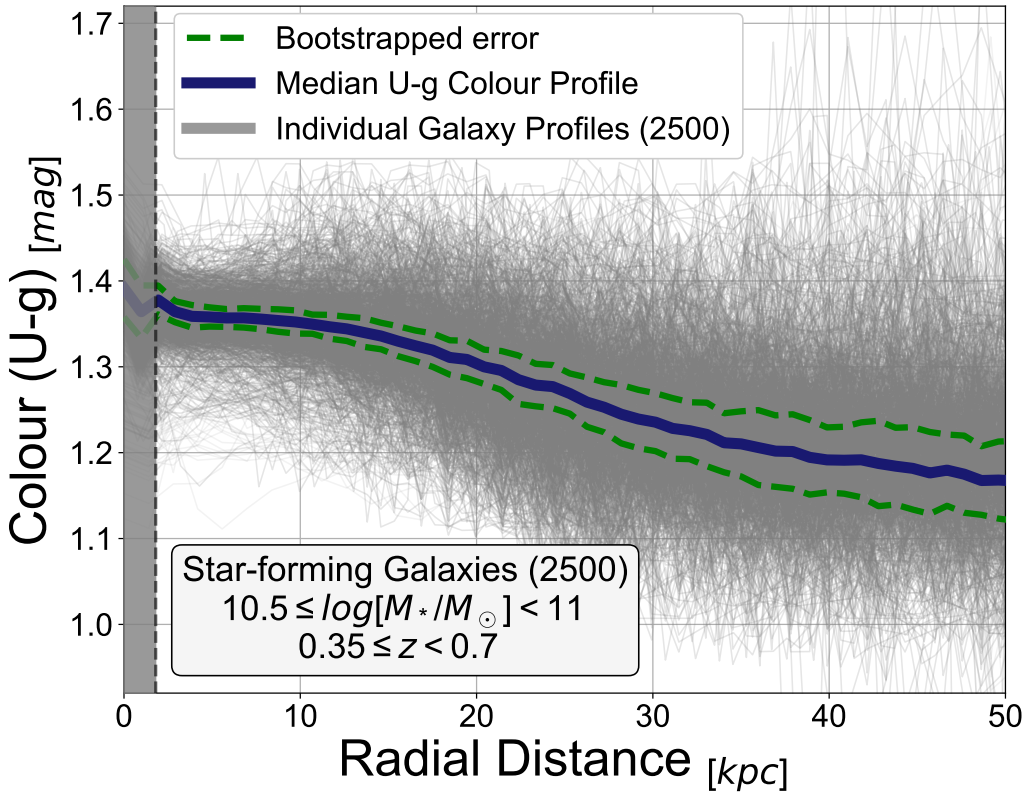

Figure 3.8. Example of a median *U-g* colour profile (blue) being computed from the individual profiles (grey) of a sub-sample of star-forming galaxies (properties listed in light grey text box). The bootstrapped errors on the median profile are shown as dashed green lines. As discussed in Sec. 3.2.3, the inner grey shaded region represents the portion of colour profiles omitted from analysis due to unreliable central surface brightness measurements.

The choice of truncation radius for these median colour profiles is based on

the previously discussed median surface brightness profile truncation procedure (Sec. 3.2.2), performed on the rest-frame U- and g-band light profiles separately. As truncation radii for U-band profiles are smaller, the U-g colour profiles only extend to those smaller radii. We also omit the innermost regions ($R < 0.5R_e$) of colour profiles from analysis (grey horizontal band in Fig. 3.8), as has been done by others studying galaxy colour profiles (e.g., Hirschmann et al. 2015; Huang et al. 2018a; Miller et al. 2023). This is due to the larger uncertainties of central surface brightness levels, and also due to the different PSFs of the $U + grizy$ filters used for colour profile construction. Despite the PSF correction we have applied (Sec. 3.1.3) some residual PSF smearing may remain, which has been shown to affect central galaxy colours (Huang et al. 2018a).

3.2.4 Galaxy Size Measurements

The additional data product that we obtain from our rest-frame g-band surface brightness profiles is sizes for galaxies in our sample, measured as the effective radius (R_e). This is the radius that contains 50% of the integrated light of a galaxy. Measuring galaxy sizes at different redshifts allows us to quantify the rate of size growth galaxies experience over time, and what sort of processes may be driving this evolution in size. We compute effective radii (R_e) for individual galaxies based on a curve of growth procedure (depicted in Fig. 3.9), where the total luminosity (L) within some radius (R) is defined as

$$L(R) = \int_0^R I(r) 2\pi r \, dr, \tag{3.5}$$

with I representing the surface brightness of the galaxy (blue profile in Fig. 3.9) and

the $2\pi rdr$ factor is the surface area element. Galaxy effective radii are then calculated by finding the radius (along the semi-major axis) where the integrated area under the brightness profile has reached half of the total area (intersection of red dashed lines in right-hand plot of Fig. 3.9).

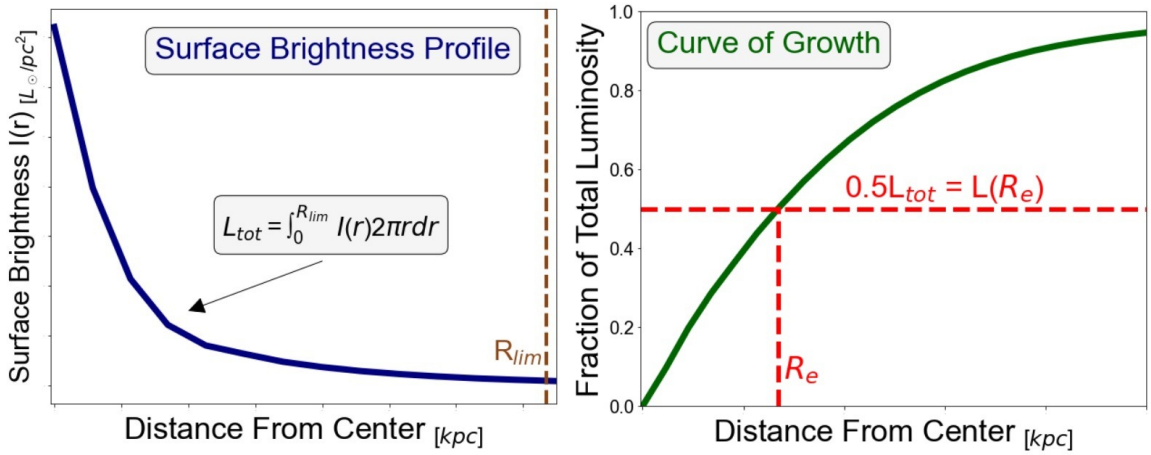

Figure 3.9. Demonstration of our galaxy size measurement procedure. Here we calculate an effective radius (R_e) by finding where the integrated curve of growth (green) has reached half of its maximum value ($0.5L_{tot}$). This curve of growth is calculated via Eq. 3.5 (also shown in light grey text box), where $I(r)$ represents the surface brightness values from the brightness profile (blue) shown on the left.

We compute median sizes for each of our galaxy bins and report the median rest-frame g-band sizes in Table 3.2 (star-forming galaxies) and Table 3.3 (quiescent galaxies). To check whether our size measurement procedure is robust, as median sizes play a key role in the analysis of our results (discussed in Sec. 3.2.5), we verified that the total magnitudes obtained from the curves of growth of individual galaxies agreed with the magnitudes reported in the HSC+CLAUDS catalogues (Sec. 2.2). The magnitudes we obtained from the curves of growth were offset from those of the catalogues by no more than $\sim$0.3 mag. This offset increases considerably ($\gtrsim$1 mag) if we use shorter profile truncation radii than those calculated through our procedure outlined in Fig. 3.7 (i.e. profiles must reach the flat portion where brightness levels

blend into the background).

We also further compared our median sizes with those from the literature. For this comparison, we show median sizes (R_e) as a function of redshift in Fig. 3.10 with different panels showing different galaxy sub-populations. We find our sizes are in good agreement with those from previous studies across our full redshift range (coloured points lie between grey symbols in Fig. 3.10). The median sizes of each of our galaxy sub-populations also follow a similar trend with decreasing redshift as one or more studies (i.e. tracks slope upward by $z \sim 0.2$). Some of the small differences between our sizes and those from the literature could simply be due to the different procedures used to fit surface brightness distributions and calculate the effective radii.

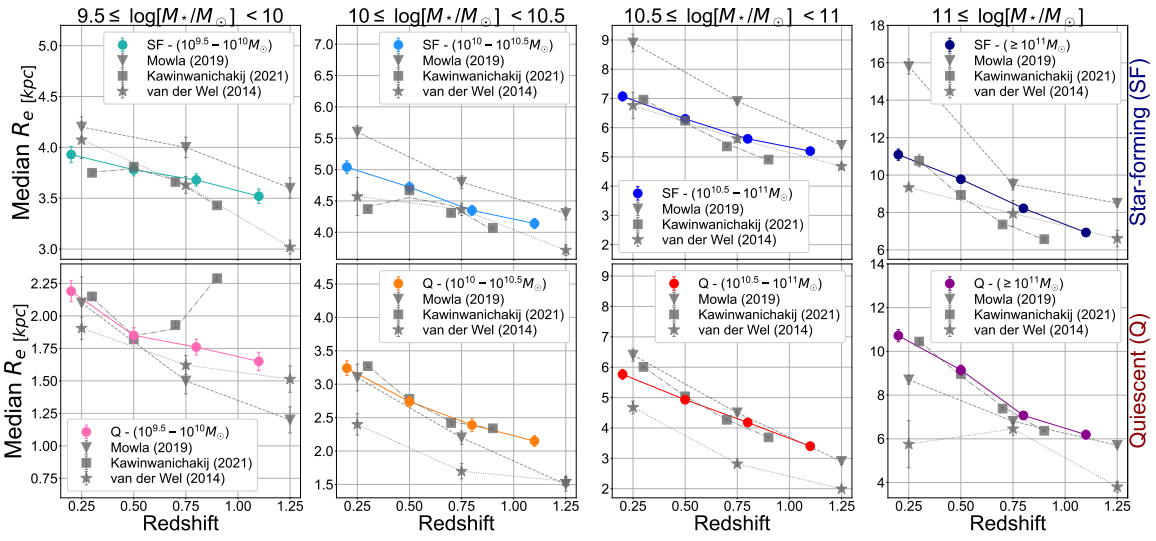

Figure 3.10. Median sizes (R_e) as a function of redshift for star-forming (top row) and quiescent (bottom row) galaxies, Stellar mass ranges are listed along the top, with left-to-right tracking low to high stellar masses. Different grey symbols represent median size measurements from the literature for comparison, showing grey stars (van der Wel et al. 2014), squares (Kawinwanichakij et al. 2021), and triangles (Mowla et al. 2019b).

Stellar Mass $[log(M_\star/M_\odot)]$	**0.2≤ z <0.35** R_e $[kpc]$	**0.35≤ z <0.7** R_e $[kpc]$	**0.7≤ z <0.9** R_e $[kpc]$	**0.9≤ z ≤1.1** R_e $[kpc]$
$9.5 \leq M_\star < 10$	3.93 ± 0.08	3.78 ± 0.06	3.68 ± 0.06	3.52 ± 0.07
$10 \leq M_\star < 10.5$	5.04 ± 0.1	4.72 ± 0.08	4.35 ± 0.08	4.14 ± 0.08
$10.5 \leq M_\star < 11$	7.07 ± 0.15	6.30 ± 0.1	5.62 ± 0.1	5.20 ± 0.12
$11 \leq M_\star$	11.09 ± 0.3	9.78 ± 0.2	8.22 ± 0.15	6.93 ± 0.2

Table 3.2: Median rest-frame g-band sizes (R_e) for our star-forming galaxy sample.

Stellar Mass $[log(M_\star/M_\odot)]$	**0.2≤ z <0.35** R_e $[kpc]$	**0.35≤ z <0.7** R_e $[kpc]$	**0.7≤ z <0.9** R_e $[kpc]$	**0.9≤ z ≤1.1** R_e $[kpc]$
$9.5 \leq M_\star < 10$	2.19 ± 0.08	1.85 ± 0.06	1.76 ± 0.06	1.65 ± 0.07
$10 \leq M_\star < 10.5$	3.24 ± 0.11	2.74 ± 0.08	2.39 ± 0.1	2.15 ± 0.08
$10.5 \leq M_\star < 11$	5.77 ± 0.16	4.93 ± 0.11	4.18 ± 0.1	3.40 ± 0.13
$11 \leq M_\star$	10.72 ± 0.28	9.15 ± 0.22	7.07 ± 0.18	6.19 ± 0.2

Table 3.3: Median rest-frame g-band sizes (R_e) for our quiescent galaxy sample.

3.2.5 Studying and Comparing Profile Evolution

Our strategy for how to effectively analyze the median rest-frame g-band surface brightness (Sec. 3.2.2) and $U-g$ colour (Sec. 3.2.3) profiles and compare their evolution with redshift, is to define different radial regions and measure profile gradients within each region. The idea behind this strategy, as discussed in Sec. 1.2.1, is that the gradients of both these profiles are influenced by galaxy assembly processes in various ways. By analyzing how brightness or colour profile gradients in different regions (e.g. bulge, disk, outer stellar halo) evolve with redshift, we can probe the processes driving galaxy assembly and the buildup of stellar haloes (Hopkins et al. 2010; Cook et al. 2016; Spavone et al. 2021).

This approach has been used extensively in both observational (e.g., Spavone et al. 2020, 2021; D'Souza et al. 2014; González Delgado et al. 2015) and simulation-based (e.g., Cook et al. 2016; Hirschmann et al. 2015; Pillepich et al. 2014) studies of

galaxies and their light and colour profiles. Following a similar methodology as the literature (Cook et al. 2016; Hirschmann et al. 2015; González Delgado et al. 2015), we use multiples of the effective radius (R_e) in order to separate different regions. Figure 3.11 illustrates specific galaxy regions we define in this work, and for which we measure profile gradients. The coloured text (i.e. red, blue, and brown text in Fig. 3.11) provides examples of physical galaxy components that may be contained within these different regions depending on the population type (i.e. star-forming or quiescent) and morphology of a galaxy.

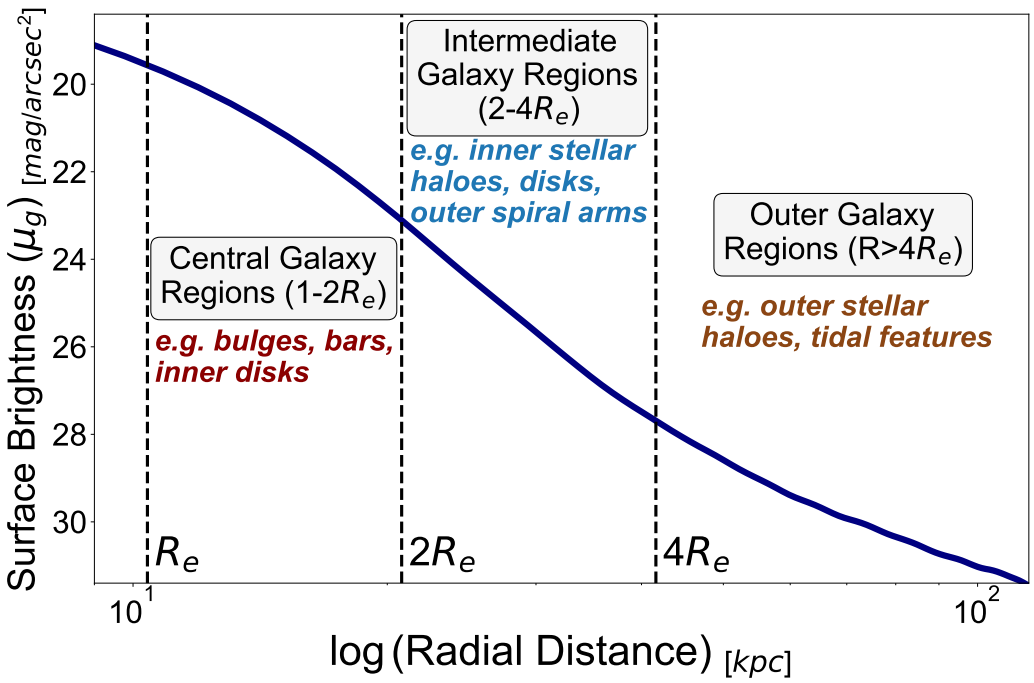

Figure 3.11. Illustration of the galaxy regions we define in Sec. 3.2.5, for which profile gradients are measured and presented throughout Sec. 4.2. The broad names of regions are in the white text boxes, along with the specific radial range associated with them (in multiples of R_e, dashed vertical lines). The coloured text in each region provides some examples of physical galaxy structural components which may be contained in that region, depending on the population type (i.e. star-forming or quiescent) and morphology of a galaxy.

We define the central (1-2R_e) and intermediate (2-4R_e) regions to align with previous studies, in order to facilitate comparisons with our observed results and

theoretical predictions regarding ex-situ assembly (one of our main research objectives outlined in Sec. 1.3). The intermediate region is where we first encounter the "stellar halo region" of galaxies (e.g. *inner stellar halo* in the blue text of Fig. 3.11), as it aligns with the stellar halo region identified in some simulations (e.g., Cook et al. 2016; Hirschmann et al. 2015). The outer region we have defined ($R > 4R_e$) is probing more extended emission (i.e. *outer stellar halo* in brown text of Fig. 3.11), and corresponds to more conservative definitions of the stellar halo region in the literature (e.g., Pillepich et al. 2014; Merritt et al. 2016; Elias et al. 2018; Gilhuly et al. 2022).

To calculate the profile gradients in each radial region we utilize the `gradient` function from `NumPy` (Harris et al. 2020) on the portion of the median brightness or colour profiles contained within that region and compute the mean gradient from the resulting output array (i.e. a list of gradient values for a portion of the profile). When measuring the outer region gradients ($R > 4R_e$), we limit the measurement of surface brightness profile gradients to $10R_e$ (not shown here in Fig. 3.11), as this is within the bounds of all median profiles in our data (i.e. within R_{lim}, Fig. 3.7). This same concept is applied to the median U-g colour profiles and colour gradients measured in the outer regions, however, because of their smaller truncation radii (discussed in Sec. 3.2.3) we limit the outer colour gradient measurements to $8R_e$ (not shown here). Finally, the reason for omitting the 0-1R_e region (grey band in Fig. 3.11) from the analysis is due to the larger uncertainties of central surface brightness values, along with potential residual PSF smearing (remaining after our correction procedure in Sec. 3.1.3) that can affect the innermost brightness values we extract.

Chapter 4

Results

We present the main results of our work throughout the following subsections. We start by presenting the main tools we use to study stellar halo assembly in our work in Sec. 4.1, which are the median rest-frame g-band surface brightness profiles for our galaxy sample.

In Sec. 4.2 we analyze light profile gradients measured within specific radial regions as described in Sec. 3.2.5, in order to probe the processes driving the assembly of galaxies in our sample. The different regions correspond to central (1-2R_e, Sec. 4.2.1), intermediate (2-4R_e, Sec. 4.2.2), and outer (4-10R_e, Sec. 4.2.3) galaxy regions.

In Sec. 4.3 we study stellar haloes through colour profiles and show the median rest-frame U-g colour profiles of our galaxy sample. In Sec. 4.3.1 we analyze these galaxy colour profiles further by measuring colour gradients within small radial regions.

Finally, in Sec. 4.4 we normalize the median rest-frame g-band surface brightness

profiles of our different galaxy sub-populations to more easily compare their evolution with redshift. Then in Sec. 4.4.1 we present the assembly of the stellar halo regions over our full redshift range and measure the increases to the total integrated stellar halo light (i.e. L_{halo}) for different galaxy sub-populations.

4.1 Median Rest-Frame g-Band Surface Brightness Profiles

Figures 4.1 and 4.2 show the median rest-frame g-band surface brightness profiles for our entire galaxy sample. The median profiles are split into the stellar mass and redshift bins they represent (see Sec. 3.2.1 and Table 3.1), and we show them together in matrix form to more easily compare the profiles of different galaxy sub-populations. In Fig. 4.3 and Fig. 4.4 we display the same results but with the x-axis (i.e. radial distance from galaxy center) in log units, to help better highlight the outer portions of profiles and the buildup of the stellar halo regions (i.e. $R \gtrsim 4R_e$) over time.

We find that all galaxy sub-populations (i.e. rows in Fig. 4.1 and Fig. 4.2) display some form of profile growth (i.e. an increase in rest-frame g-band surface brightness) from high to low redshift (left-to-right columns in Fig. 4.1 and Fig. 4.2). More massive galaxies exhibit more profile buildup over the full redshift range, and this implies stellar material is either being formed (e.g. in-situ star-formation, Sec. 1.1.1) or acquired (e.g. ex-situ accretion, Sec. 1.1.2) over time. It is also possible that some of the increase in brightness is resulting from the evolution of stellar populations, in the form of changing stellar mass-to-light ratios (in rest-frame g-band). This

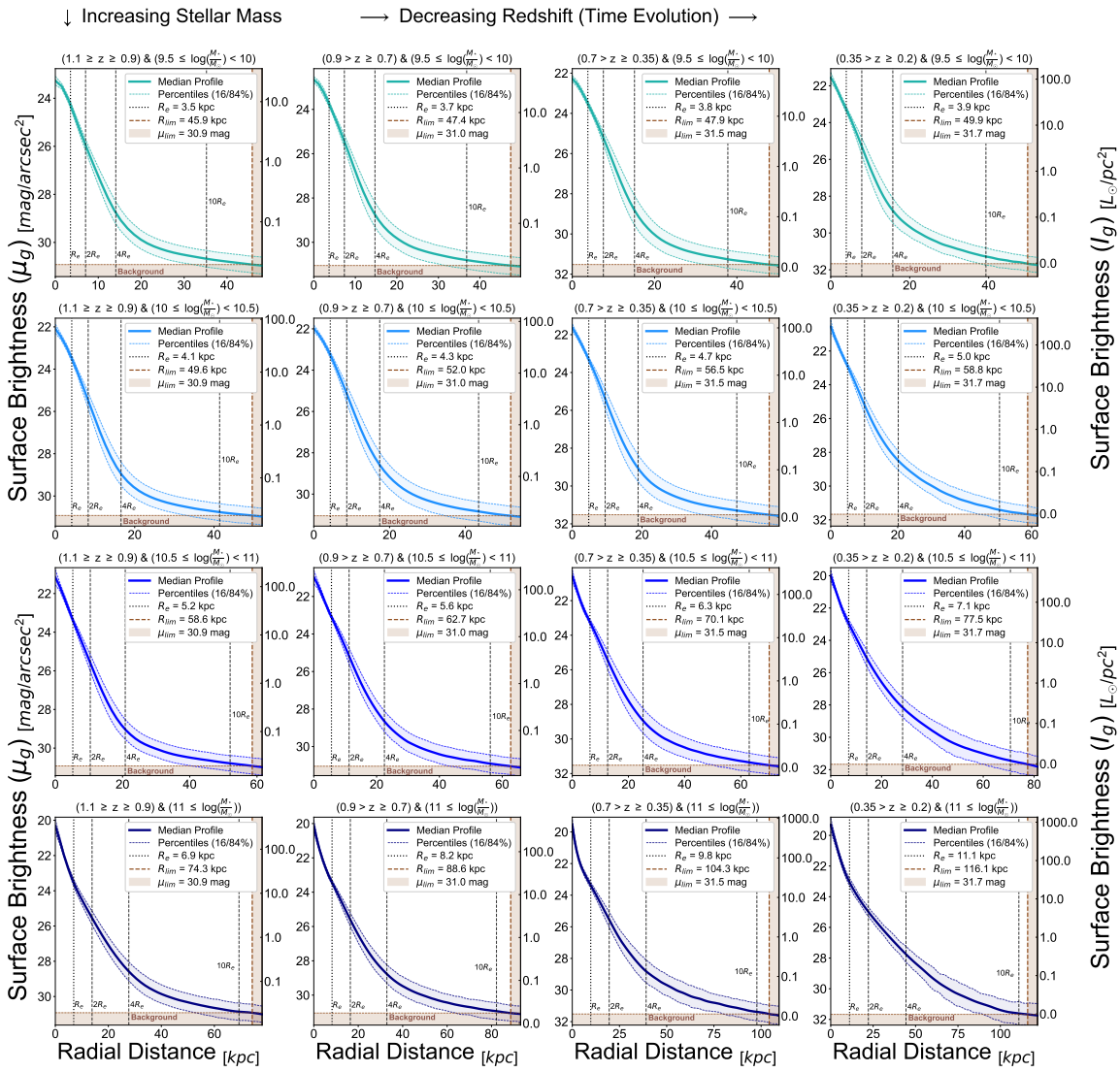

Figure 4.1. Median rest-frame g-band surface brightness profiles of the entire star-forming galaxy sample. Different stellar mass bins are separated into different rows and colours, while separate columns show different redshift ranges (both listed in the titles of each panel). In each panel, the median profile is the solid coloured line (the width of profiles represent bootstrapped errors), and the coloured shaded regions represent the 16 and 84 percentiles of the whole sub-population. The brown shaded regions indicate where profiles have been truncated (i.e. R_{lim}) as they have reached background surface brightness levels (μ_{lim}, see Sec. 3.2.2). Vertical dashed black lines show 1, 2, 4, and 10 R_e, and the x-axis of each panel displays radial distance in units of kpc so physical scales can be compared across redshift (i.e. across columns).

would preferentially affect quiescent galaxies more than star-forming galaxies, but as demonstrated by Hopkins et al. (2010), changing $M_\star/L$ ratios would not be able to

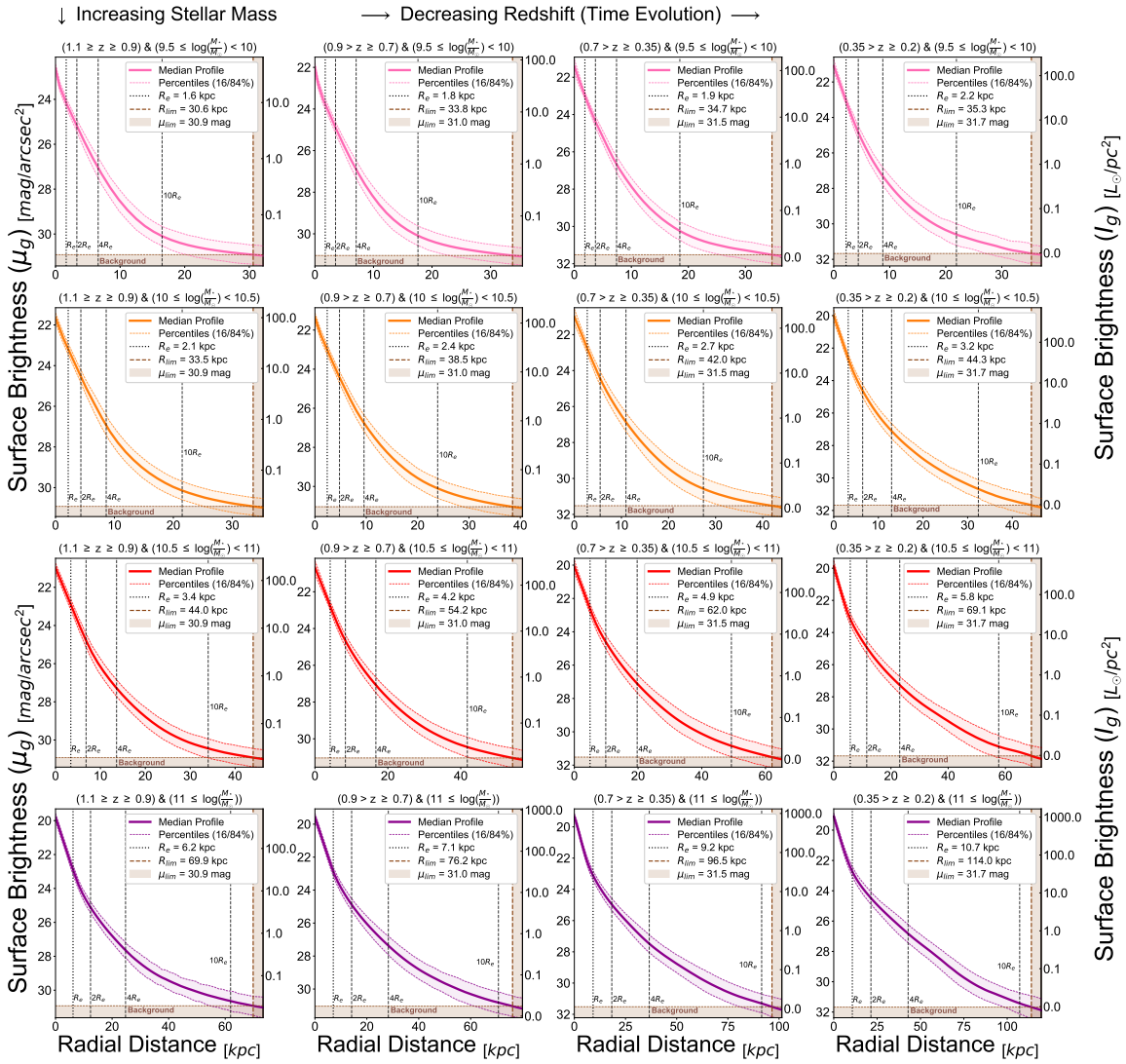

Figure 4.2. Same plot design as Fig. 4.1, but for the quiescent galaxy sample.

produce as much brightness profile growth as ex-situ accretion, particularly in the outer regions of profiles (see their Fig. 2).

The profile buildup is particularly apparent in the outer stellar halo regions ($R \geq 4R_e$), which can be seen more clearly in Fig. 4.3 and Fig. 4.4 where radial distances are log-scaled. The buildup we observe in the outer profile regions of different galaxy sub-populations in our sample would agree with the broad picture of extended stellar

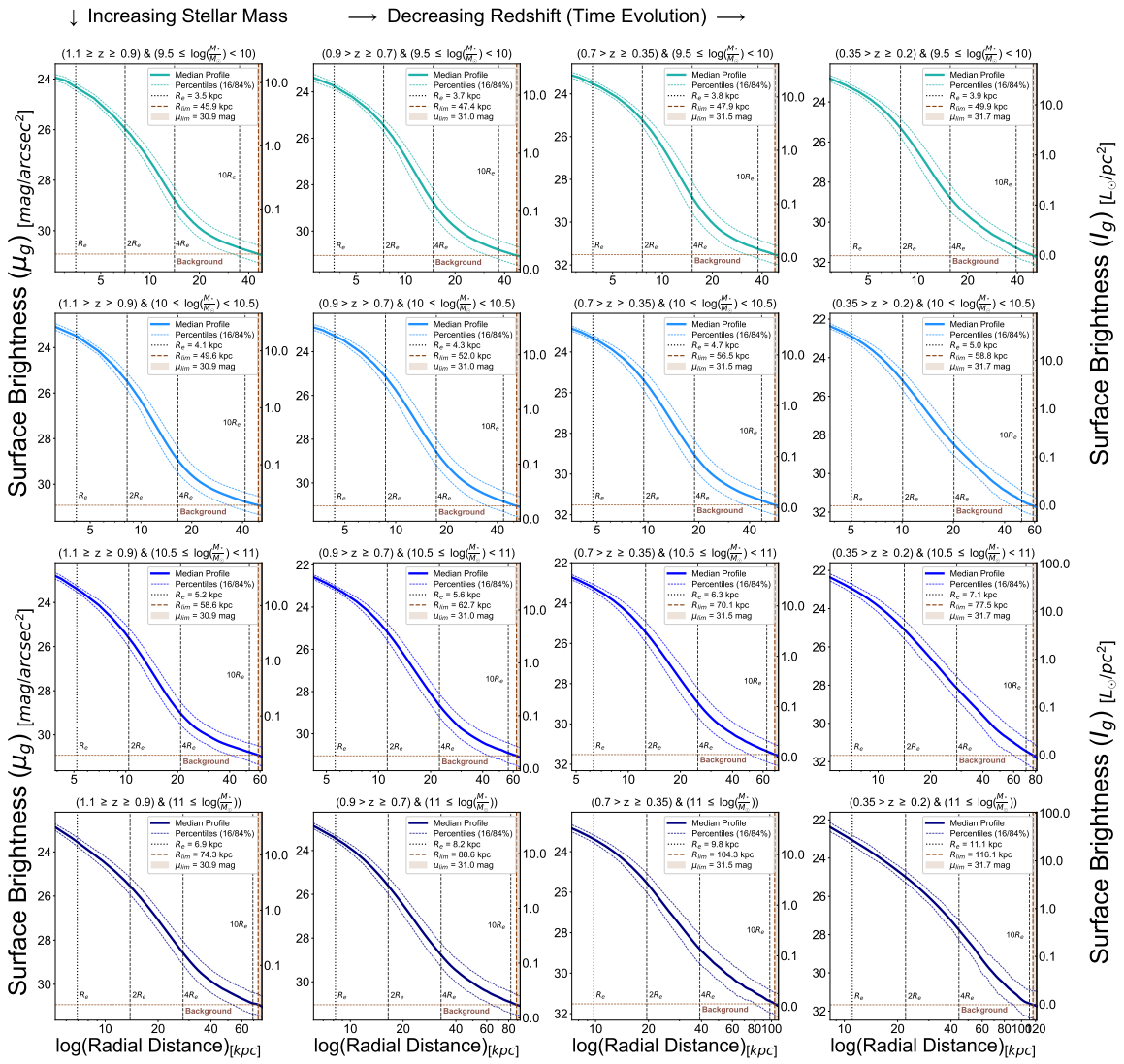

Figure 4.3. Same plot design and profiles as Fig. 4.1, but with radial distance (x-axis) in log units. The plot limits in each panel have also been adjusted slightly inwards to better focus on the sub-divided galaxy regions (1-2-4-10 R_e), which are analyzed in further detail throughout Sec. 4.2.

haloes being gradually built up around galaxies over time (Oser et al. 2010; Cook et al. 2016; Buitrago et al. 2017; Huang et al. 2018a; Rey & Starkenburg 2022; Huško et al. 2022).

However, it is clear from our results that this buildup is not equal across all galaxies, and scales strongly with stellar mass for both the star-forming and quiescent

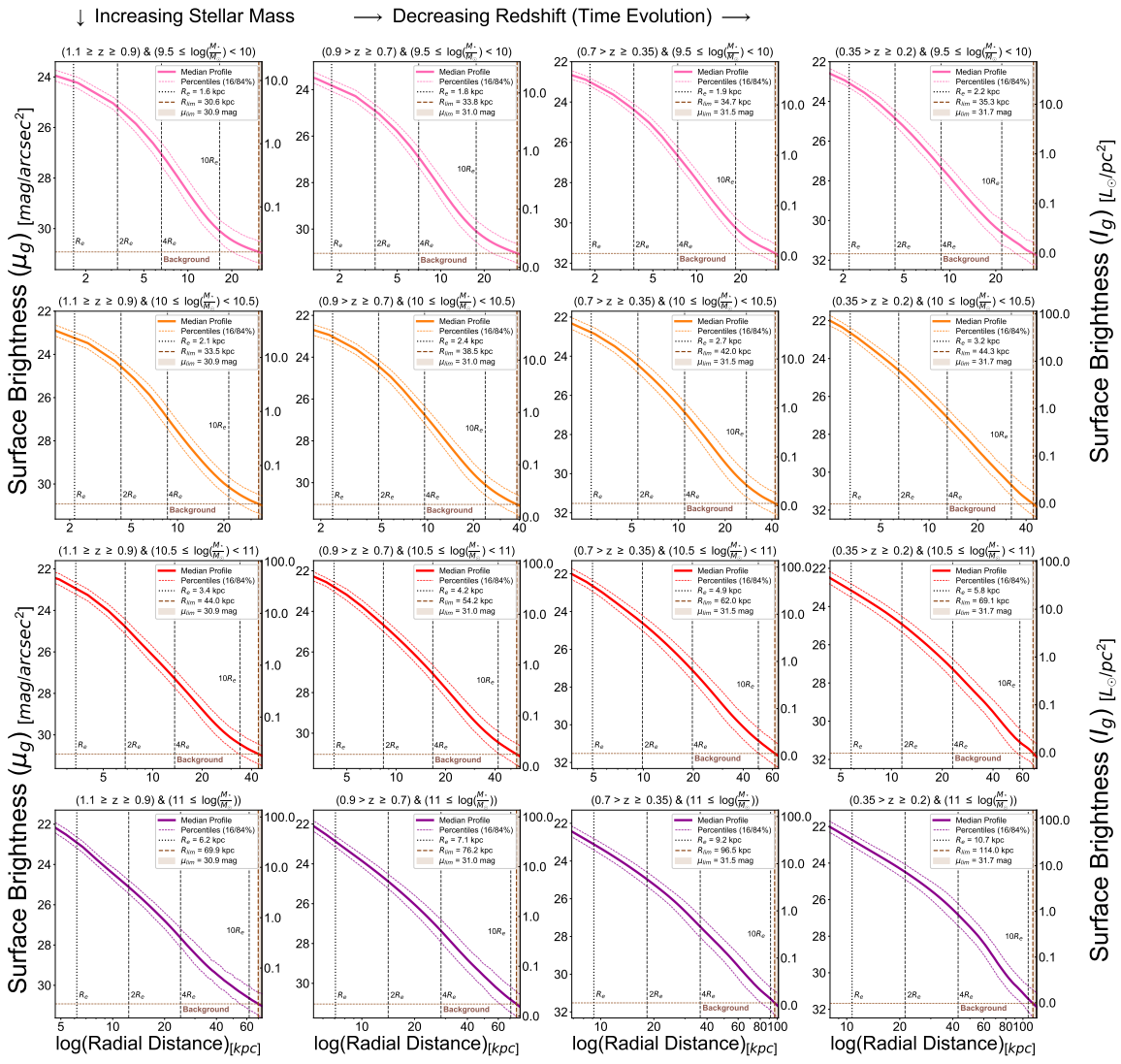

Figure 4.4. Same as Fig. 4.3 but for the quiescent galaxy sample.

populations - i.e. *higher mass galaxies build up stellar haloes that are much brighter and more extended in size over 0.2 ≤ z ≤ 1.1.* This can be inferred from the difference in outer profile growth ($R \geq 4R_e$) between the higher and lower stellar mass bins (upper and lower rows in Fig. 4.3 and Fig. 4.4) across the whole redshift range (left-to-right columns). We also analyze this outer profile growth in greater detail in Fig. 4.14 (Sec. 4.4.1), where we normalize and display median light profiles from different

redshift ranges together in the same plots.

For the majority of quiescent galaxies in our sample (galaxies of $M_\star < 10^{11} M_\odot$), a possible explanation for the amount of buildup in their outer profile regions is stellar halo assemblies driven mainly by minor and very minor mergers (see Sec. 1.1.2 and Fig. 1.3). For the most massive quiescent galaxies ($M_\star \geq 10^{11} M_\odot$), the considerable amount of growth seen in their outer profile regions may indicate that some major mergers have also occurred within the population since $z \sim 1.1$. These scenarios are corroborated by the work of Hilz et al. (2013) and Hopkins et al. (2010), who demonstrated the predicted effects of different merger types on the brightness profiles of simulated galaxies. They demonstrated that both minor and major mergers can build up outer profile regions similar to what we see here in Fig. 4.1-4.4, but major mergers add more growth.

For star-forming galaxies, it is possible that star formation is contributing a portion of this stellar material buildup in addition to ex-situ accretion from merger activity. In Sec. 5.1 we explore this possibility and disentangle the relative contributions to stellar halo growth from different processes (i.e. in-situ and ex-situ fractions). In Sec. 5.1 we also explore how much of the stellar halo growth in quiescent galaxies can be attributed to the effect of progenitor bias.

When we analyze the profile buildup in central (1-2R_e) and intermediate (2-4R_e) regions since $z \sim 1.1$, we see that the high-mass galaxies ($M_\star \geq 10^{10.5} M_\odot$, lower two rows in Fig. 4.1 and Fig. 4.2) exhibit much more growth than low-mass galaxies ($10^{9.5} M_\odot \leq M_\star < 10^{10.5} M_\odot$, upper two rows in Fig. 4.1 and Fig. 4.2). This contrast between the two stellar mass regimes becomes even more apparent in the analysis of

profile gradients which we present in Sec. 4.2.1 (central region gradients) and Sec. 4.2.2 (intermediate region gradients).

Substantial profile growth in these innermost regions has been linked to a significant increase in merger-related accretion (e.g., Pillepich et al. 2014; Cook et al. 2016; Spavone et al. 2021), and may be particularly affected by stellar mass assembly through major mergers (Spavone et al. 2017; Genina et al. 2023). The assembly of stellar mass in the inner regions of galaxies can also be affected by various internal processes like in-situ star formation (Sec. 1.1.1), or feedback mechanisms (AGN or stellar feedback, Sec. 1.1.3). However, these processes are predicted to cause different effects on the inner portions of galaxy light profiles as we demonstrate in the following section through the analysis of profile gradients (Sec. 4.2).

4.2 Median Surface Brightness Profile Gradients

In order to disentangle the physical processes that are driving the evolution seen in our median surface brightness profiles we must move beyond a simple visual inspection and qualitative analysis. As discussed in Sec. 3.2.5, a commonly used approach is to measure surface brightness profile gradients within specific radial regions (e.g., Cook et al. 2016; González Delgado et al. 2015; D'Souza et al. 2014; Spavone et al. 2021). The gradients of surface brightness profiles are predicted to exhibit different changes (e.g., become flatter or steeper) depending on the processes affecting the assembly of material in galaxies (Hopkins et al. 2010; Hilz et al. 2013; Cook et al. 2016).

We have defined three separate regions where we measure the gradients (pro-

cedure outlined in Sec. 3.2.5) of our median rest-frame g-band surface brightness profiles, which include central (1-2R_e, Sec. 4.2.1), intermediate (2-4R_e, Sec. 4.2.2), and outer (4-10R_e, Sec. 4.2.3) galaxy regions. The gradient values for all three regions are summarized in Table A.1 (quiescent galaxies) and Table A.2 (star-forming galaxies) in the Appendix.

4.2.1 Gradients of Central Galaxy Regions $(1 - 2R_e)$

In Fig. 4.5 we show the redshift evolution of the median rest-frame g-band light profile gradients measured within central regions (1-2R_e), with colours corresponding to the same galaxy sub-populations as the matrix plots in Sec. 4.1 (Fig. 4.1-4.4).

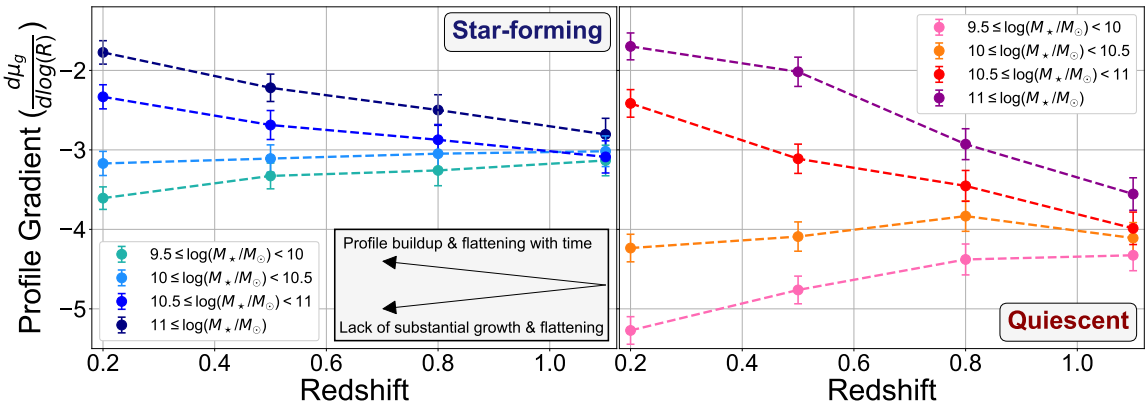

Figure 4.5. Profile gradients as a function of redshift, measured from the central regions (1-2 R_e) of the median rest-frame g-band surface brightness profiles (Fig. 4.1 and 4.2). Different stellar mass bins for the star-forming (left) and quiescent (right) samples are shown in different colours. Errors on gradient values come from the median brightness profile percentiles (16/84%), see Sec. 3.2.2.

We find that more massive galaxies display flatter central gradients in both the star-forming and quiescent populations (e.g., darker colours above lighter colours in Fig. 4.5). We see a contrast in evolution with redshift between the central gradients

of high-mass ($M_\star \geq 10^{10.5} M_\odot$) and low-mass ($10^{9.5} M_\odot \leq M_\star < 10^{10.5} M_\odot$) galaxies. The two higher stellar mass bins in both the quiescent and star-forming population evolve towards flatter central gradients at low redshift ($z \sim 0.2$). Conversely, the two lower stellar mass bins in both populations display the opposite trend towards steeper central gradients at low redshift.

This contrast in the redshift evolution of central gradients is more easily seen in Fig. 4.6, where gradients are normalized to their lowest redshift value (i.e. the $z = 0.2$ data points in Fig. 4.5). This brings the gradient values onto the same relative scale, and now the difference between a *steepening* or *flattening* trend with decreasing redshift is obvious from the comparison with the horizontal dashed line at $y = 1$ (a *flat* trend).

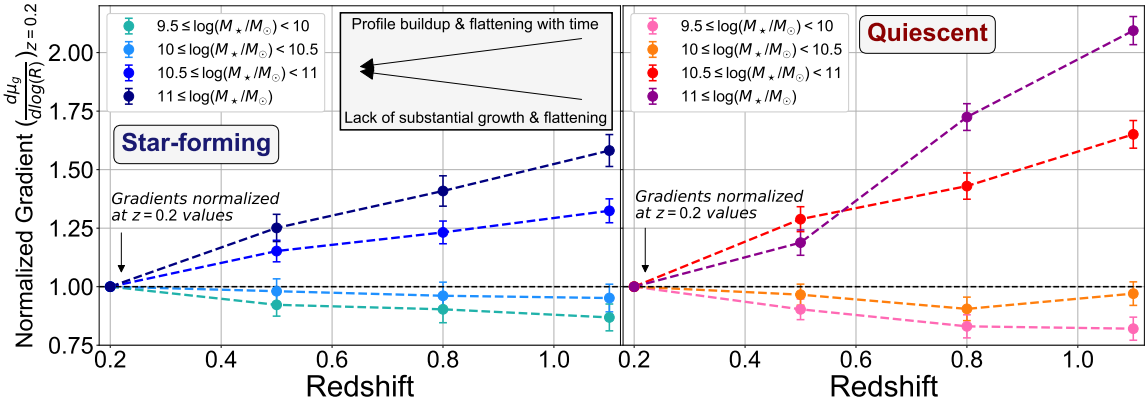

Figure 4.6. Same gradients as in Fig. 4.5, except now normalized to their $z = 0.2$ values to better highlight and compare the trends with redshift.

Flattening of light profile gradients in central regions has been linked with merger interactions and increased ex-situ accretion in simulated galaxies (Hilz et al. 2013; Hopkins et al. 2010; Cook et al. 2016; Pillepich et al. 2014; Cannarozzo et al. 2022). This may indicate that the high-mass galaxies ($M_\star \geq 10^{10.5} M_\odot$) in our sample have

experienced more mergers and accreted more material since $z \sim 1.1$ than the less massive galaxies ($10^{9.5} M_{\odot} \leq M_{\star} < 10^{10.5} M_{\odot}$). This result is in agreement with predictions from numerous simulations (e.g., Cook et al. 2016; Rodriguez-Gomez et al. 2016; Tacchella et al. 2019; Huško et al. 2022).

The high-mass ($M_{\star} \geq 10^{10.5} M_{\odot}$) quiescent galaxies show greater evolution (flattening) in the central light profile gradients since $z \sim 1.1$ than star-forming galaxies of similar high masses. The central gradients of these massive quiescent galaxies (upper two mass bins) are ∼65% and ∼109% steeper at $z \sim 1.1$ compared to their low redshift ($z \sim 0.2$) value. In comparison, the central gradients of the massive star-forming galaxies are only 32% and 58% steeper at high redshift (see right-hand data points in Fig. 4.6). This implies massive ($M_{\star} \geq 10^{10.5} M_{\odot}$) quiescent galaxies may be growing more through ex-situ accretion than massive star-forming galaxies in our sample, which would align with predictions from Davison et al. (2020) based on ex-situ fractions of galaxies in the EAGLE simulation.

The low-mass galaxies ($10^{9.5} M_{\odot} \leq M_{\star} < 10^{10.5} M_{\odot}$, both star-forming and quiescent galaxies) do not show any substantial flattening in the central regions of their brightness profiles (upper two rows in Fig. 4.1-4.4, between 1-2R_e), and instead show trends towards slightly steeper gradients at lower redshifts in Fig. 4.6 (roughly ∼10-20% flatter at high redshift). Steeper inner light profile gradients have been shown to arise from internal processes operating within a galaxy rather than from buildup due to ex-situ accretion. These processes can include in-situ star-formation (for star-forming galaxies), AGN activity (Silk 2013; Cook et al. 2016; Davies et al. 2022), or stellar feedback (Cook et al. 2016). Additionally, the stellar migration described by Boecker et al. (2023) may lead to steeper inner light profiles as the authors

demonstrate that stars can migrate to the very centers of galaxies (e.g., < 1 kpc).

The results from this analysis of central light profile gradients and their evolution over $0.2 \leq z \leq 1.1$ imply that the stellar mass assembly in central regions (1-2R_e) is proceeding differently for low-mass galaxies ($10^{9.5} M_{\odot} \leq M_{\star} < 10^{10.5} M_{\odot}$) than high-mass galaxies ($M_{\star} \geq 10^{10.5} M_{\odot}$). Low-mass galaxies are lacking any substantial light profile growth in central regions and their inner assembly may be more influenced by internal physical processes or feedback mechanisms. The high-mass galaxies are exhibiting significant light profile growth in these central regions, particularly in the quiescent population, and this growth is likely fueled by ex-situ accretion based on theoretical predictions of profile behaviour (Hopkins et al. 2010; Hilz et al. 2013; Cook et al. 2016).

4.2.2 Gradients of Intermediate Galaxy Regions ($2 - 4R_e$)

Galaxy simulations have shown that light profile buildup and subsequent gradient flattening in these intermediate galaxy regions (2-4R_e) are also highly correlated with an increase in accreted material and merger activity (Hopkins et al. 2010; Hilz et al. 2013; Pillepich et al. 2014; Cook et al. 2016). This may be even more true for these intermediate regions than for the central regions (1-2R_e, Sec. 4.2.1) as demonstrated by Cook et al. (2016) and Rodriguez-Gomez et al. (2016), who found higher ex-situ fractions in these more extended intermediate regions compared to the central regions of galaxies. In Fig. 4.7 we show our observed median rest-frame g-band surface brightness profile gradients measured within intermediate (2-4R_e) regions as a function of redshift.

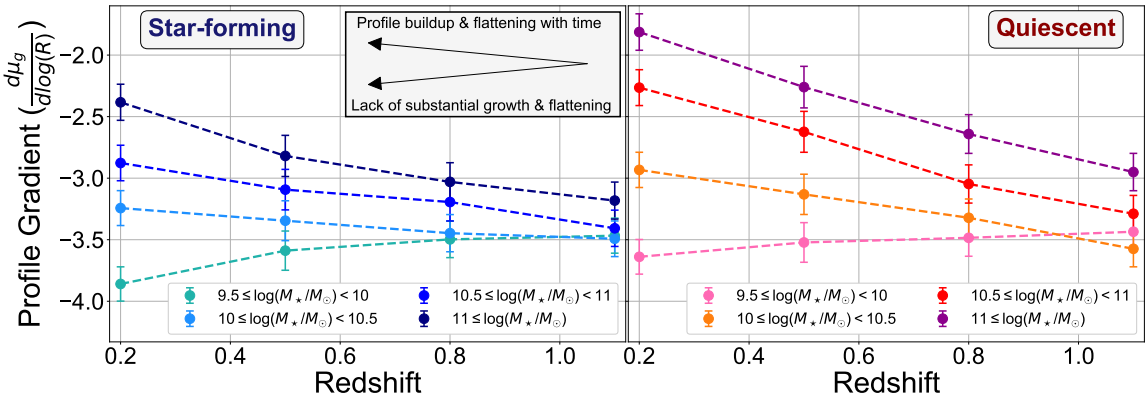

Figure 4.7. The same figure design as Fig. 4.5, but with median surface brightness profile gradients measured within intermediate galaxy regions (2-4 R_e).

We see similar trends in the redshift evolution of intermediate region gradients (Fig. 4.7) as in the central region gradients (Fig. 4.5). More massive galaxies (i.e. higher stellar mass bins) in both our star-forming and quiescent sample have flatter brightness profile gradients, particularly by $z \sim 0.2$ (i.e. darker colours in Fig. 4.7 have flatter gradients). Similar to Sec. 4.2.1, in Fig. 4.8 we show gradients normalized to their low redshift value (i.e. $z = 0.2$ data points in Fig. 4.7).

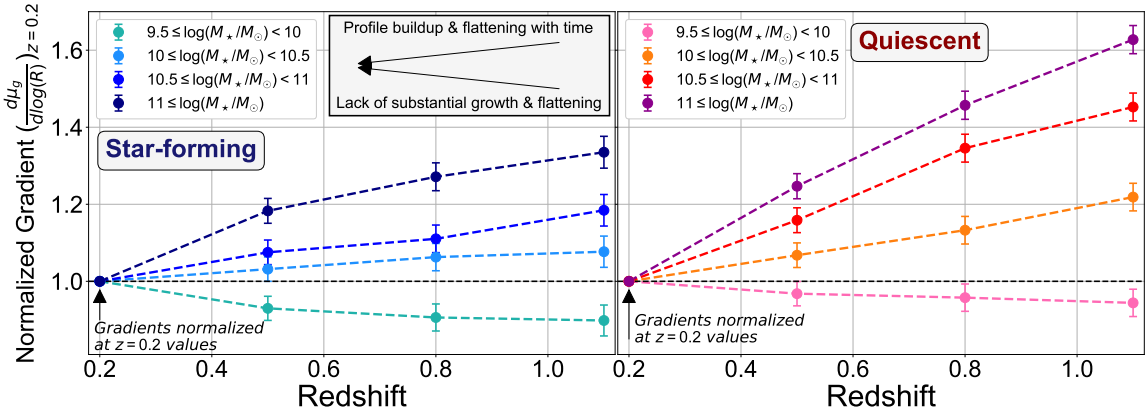

Figure 4.8. The same gradients and figure design as in Fig. 4.7, except now normalized to their $z = 0.2$ values to better highlight and compare the trends with redshift.

Tracks in Fig. 4.8 show that high-mass galaxies ($M_\star \geq 10^{10.5} M_\odot$) again show

a trend towards flatter gradient values at lower redshifts (i.e. darker colours show a flattening trend in Fig. 4.8 as they did in Fig. 4.6). The lowest stellar mass bin ($10^{9.5}M_{\odot} \leq M_{\star} < 10^{10}M_{\odot}$) also displays the same trend towards steeper gradient values at low redshift (light aqua and pink lines in Fig. 4.8) similar to their central gradients (same colours in Fig. 4.6).

However, there is a change in evolutionary behaviour for the second lowest stellar mass bin ($10^{10}M_{\odot} \leq M_{\star} < 10^{10.5}M_{\odot}$) in both the star-forming and quiescent populations. In the central gradients of the previous section, both populations displayed a steepening trend (light blue and orange in Fig. 4.6). Now with the intermediate region gradients (same colours in Fig. 4.8) the quiescent galaxies of this mass range show a small trend towards flatter gradients at low redshift, and the star-forming sample displays a flat trend (roughly constant gradient with redshift).

This stellar mass range (i.e. $10^{10}M_{\odot} \leq M_{\star} < 10^{10.5}M_{\odot}$) is just below the pivot mass ($M_p = 10^{10.5}M_{\odot}$) discussed in Sec. 3.2.1, which studies have argued marks the transition from the in-situ to the ex-situ dominated stage of galaxy assembly (e.g., Mowla et al. 2019a; Kawinwanichakij et al. 2021). The change in the evolution of light profile gradients we see (from a *steepening* trend to a small *flattening* trend) may indicate that the contribution of accreted ex-situ material is starting to become important for galaxies in this stellar mass range and at these intermediate distances 2-4R_e. This result could arise from assembly through minor and very minor mergers (Sec. 1.1.2). These minor interactions could account for the buildup and gradient flattening in intermediate regions (Fig. 4.8), while also accounting for the lack of growth and the gradient steepening (i.e. Fig. 4.6) in central regions (Hopkins et al. 2010; Hilz et al. 2013; Spavone et al. 2021; Genina et al. 2023).

If we consider galaxies of $M_\star \geq 10^{10} M_\odot$ (darker colours in Fig. 4.8, those with flattening trends), we find that gradient values of quiescent galaxies evolve more (grow flatter) since $z \sim 1.1$ than star-forming galaxies. For the star-forming galaxies, the profile gradients in intermediate regions (2-4R_e) are 8%, 18%, and 34% steeper at high redshift ($z \sim 1.1$) compared to their low redshift ($z \sim 0.2$) values. In comparison, the intermediate region gradients of the quiescent galaxy profiles are 22%, 45%, and 63% steeper at high redshift.

If light profile buildup and flatter slopes in these intermediate regions are indeed caused by an increase in accreted ex-situ material (Pillepich et al. 2014; Cook et al. 2016; Spavone et al. 2021), then our results would imply that ex-situ accretion is heightened in quiescent galaxies of $M_\star \geq 10^{10} M_\odot$ compared to star-forming galaxies. This result agrees with predictions of ex-situ fractions from the EAGLE simulation (Davison et al. 2020).

4.2.3 Gradients of Outer Galaxy Regions $(4 - 10R_e)$

The final region where we measure profile gradients from the median rest-frame g-band surface brightness profiles of our sample is the outer *stellar halo* region (4-10 R_e). Figure 4.9 shows the outer gradients as a function of redshift for the different sub-populations, following the same figure design as previous gradient plots.

For both the star-forming and quiescent populations, we find that more massive galaxies have flatter profile gradients (darker colours have flatter gradients in Fig. 4.9). Based on predictions from simulations this would imply that more massive galaxies build up more stellar material in these outer regions through ex-situ accretion

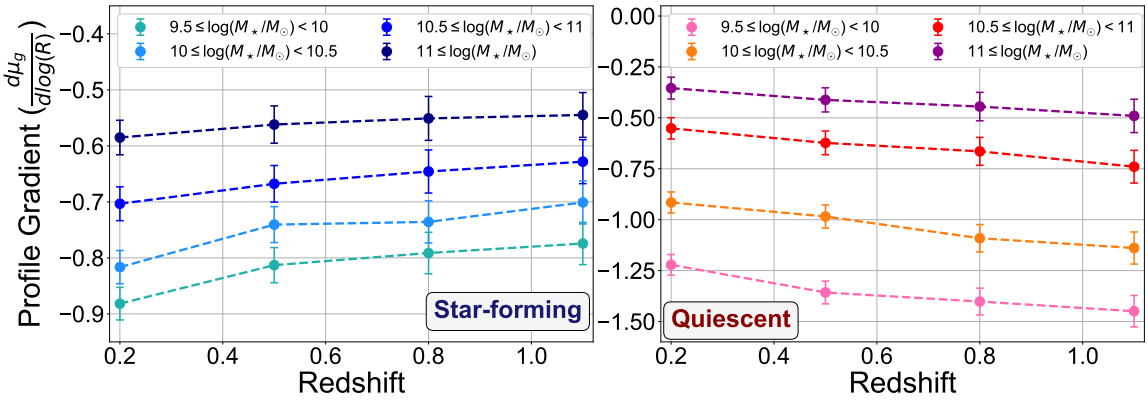

Figure 4.9. Same figure design as Fig. 4.5, but with median surface brightness profile gradients measured within outer galaxy regions (4-10R_e).

than less massive galaxies (Hilz et al. 2013; Hopkins et al. 2010; Pillepich et al. 2014; Cook et al. 2016).

Figure 4.10 shows the gradients normalized to their low redshift value (i.e. $z = 0.2$ data points from Fig. 4.9) as was done in previous sections.

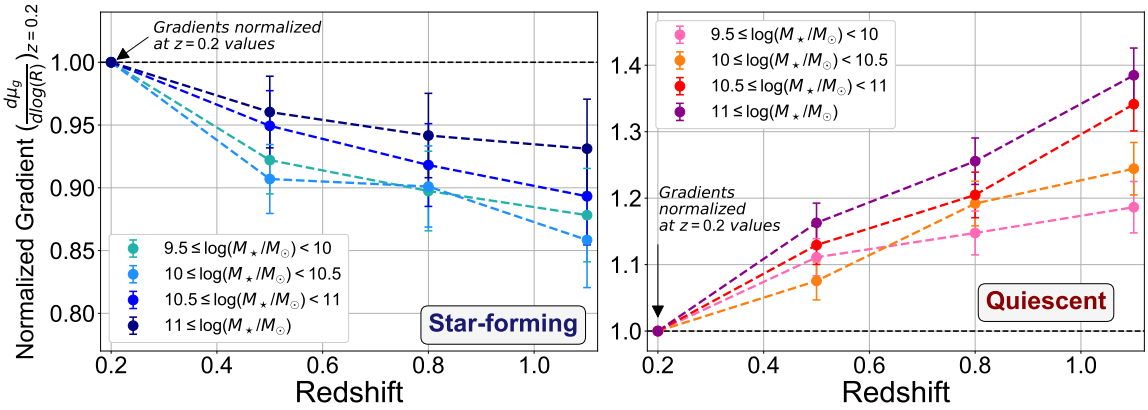

Figure 4.10. Same gradients as in Fig. 4.9, normalized to their $z = 0.2$ values to better highlight and compare any trends with redshift.

From the normalized gradients, we can see that the star-forming and quiescent galaxies display different behaviour in their evolution with redshift. The outer light profile gradients of star-forming galaxies become steeper with decreasing redshift,

while the quiescent galaxies display flatter gradients at lower redshifts. Based on predictions from Cook et al. (2016), the trend towards steeper outer profile gradients at lower redshifts in our star-forming galaxy sample is the result of galaxy assembly driven by internal processes and in-situ star formation. For quiescent galaxies, the trend towards flatter outer profile gradients with decreasing redshift seen in all four stellar mass bins is likely arising from ex-situ accretion based on theoretical predictions (e.g., Hopkins et al. 2010; Hilz et al. 2013; Cook et al. 2016).

We also find a trend in stellar mass with the normalized outer gradients in Fig. 4.10. The gradients of less massive star-forming galaxies grow steeper over the full redshift range, where gradients are $\sim$ 12%, 14%, 11%, and 7% flatter at high redshift (low to high stellar mass bins respectively). This may be the result of more massive star-forming galaxies growing through both in-situ and ex-situ assembly, which would reduce the amount of gradient steepening expected from in-situ assembly alone. For quiescent galaxies, the gradients of more massive galaxies grow flatter with decreasing redshift than lower mass galaxies, where gradients are 18%, 24%, 34%, and 38% steeper at high redshift (low to high stellar mass bins respectively). This trend in stellar mass for the quiescent sample aligns with predictions of ex-situ assembly, where more massive galaxies are predicted to have higher ex-situ fractions in these outer regions which would induce flatter gradients over time (e.g., Cook et al. 2016; Rodriguez-Gomez et al. 2016; Tacchella et al. 2019).

4.3 Median Rest-Frame U-g Colour Profiles

As discussed in Sec. 3.2.3, we have extracted and computed median rest-frame U-g colour profiles for our galaxy sample. Figure 4.11 shows these median colour profiles for both the star-forming and quiescent populations, following the same matrix plot design (and coloured galaxy bins) as the median rest-frame g-band surface brightness profiles shown in Fig. 4.1 and Fig. 4.2.

When we examine the median rest-frame U-g colour profiles of different galaxy sub-populations (panels of Fig. 4.11), we see that colour profiles of quiescent galaxies always display redder colours than those of star-forming galaxies of a similar stellar mass and redshift range (i.e. the colour profiles of the two populations never overlap). This is expected given our method of separating galaxies via a colour-colour diagram cut (Sec. 2.4).

We also note colours get redder over time (decreasing redshift), but as mentioned in Chap. 1, galaxy colours are influenced by a number of factors making it difficult to say with certainty what is driving the evolution in colours and reddening. Two of the largest unknowns are how stellar metallicities and ages are impacting our results, as these can have a significant influence on the colours of galaxies (i.e. higher metallicities and older ages cause redder colours in galaxies; e.g., Gustafsson 1989; Gilmore et al. 1989; Ferreras & Silk 2000; Streich et al. 2014; Hirschmann et al. 2015). There is also the effect of dust, which will preferentially affect star-forming galaxies more than quiescent galaxies.

However, as demonstrated in the simulations by Hirschmann et al. (2015), even

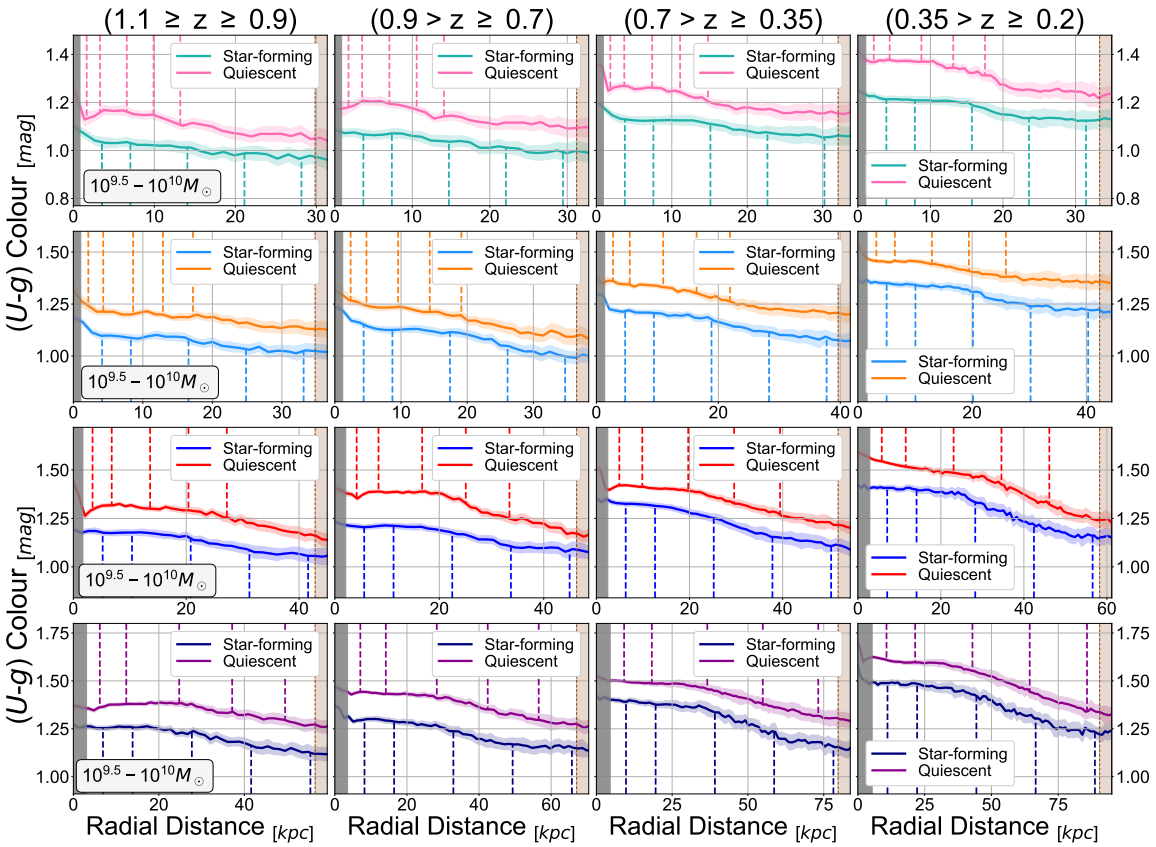

Figure 4.11. Median rest-frame U-g colour profiles (procedure discussed in Sec. 3.2.3) for star-forming (bluer colours) and quiescent (redder colours) galaxies in our sample. Different rows show different stellar mass bins (listed in grey text boxes, lower rows are higher stellar masses), and columns represent different redshift bins (listed in titles). Shaded coloured regions surrounding profiles represent bootstrapped errors on the median colour profiles. The grey-shaded horizontal regions show the innermost portions of profiles ($R \lesssim 0.5R_e$) which are omitted from analysis (see Sec. 3.2.3). The brown-shaded region indicates the truncation limit of the colour profiles. The dashed coloured lines in each panel indicate 1, 2, 4, 6, and $8R_e$ for that particular stellar mass and redshift range.

when we account for evolution in stellar properties there remains an identifiable difference in colour gradients that results from different types of merger activity. We discuss this further in Sec. 5.3 with a comparison with the results of (Hirschmann et al. 2015).

The median rest-frame U-g colour profiles of all galaxy sub-populations in our sample become steeper by low redshift ($z \sim 0.2$) and exhibit negative colour gradients

(i.e. redder interiors, bluer outskirts). The median colour profiles are also flatter for lower stellar mass galaxies (upper rows in Fig. 4.11).

Minor and very minor mergers (Sec. 1.1.2) have been linked with more negative colour gradients (e.g., Hirschmann et al. 2015; Lambas et al. 2012; Bernardi et al. 2011). These minor interactions could induce these trends from flatter colour profiles at high redshift ($z \sim 1.1$) to steeper (more negative) profiles at low redshift ($z \sim 0.2$). This may indicate these minor interactions are playing an important role in driving the evolution of colours in the outskirts of galaxies since $z \sim 1.1$. We analyze these colour gradients in more detail in Sec. 4.3.1.

4.3.1 Median Colour Profile Gradients

We measure colour gradients of our median rest-frame U-g colour profiles (Fig. 4.11) within consecutive radial ranges (1-2, 2-4, 4-6, and 6-8R_e). We show these gradients as a function of redshift in Fig. 4.12, with different columns showing different radial regions. The colours represent the same galaxy sub-populations from the colour profile matrix plot (Fig. 4.11). The colour gradients for all regions are also compiled in Table B.1 (star-forming galaxies) and Table B.2 (quiescent galaxies) in the Appendix.

Immediately noticeable is that colour gradients evolve very little in the inner regions over $0.2 \leq z \leq 1.1$ (1-2, 2-4R_e, left two columns in Fig. 4.12). Colour gradients for both star-forming and quiescent galaxies stay within ± 0.2 mag/dex of zero (i.e. a flat colour gradient) over the full redshift range, and there is no trend with stellar mass.

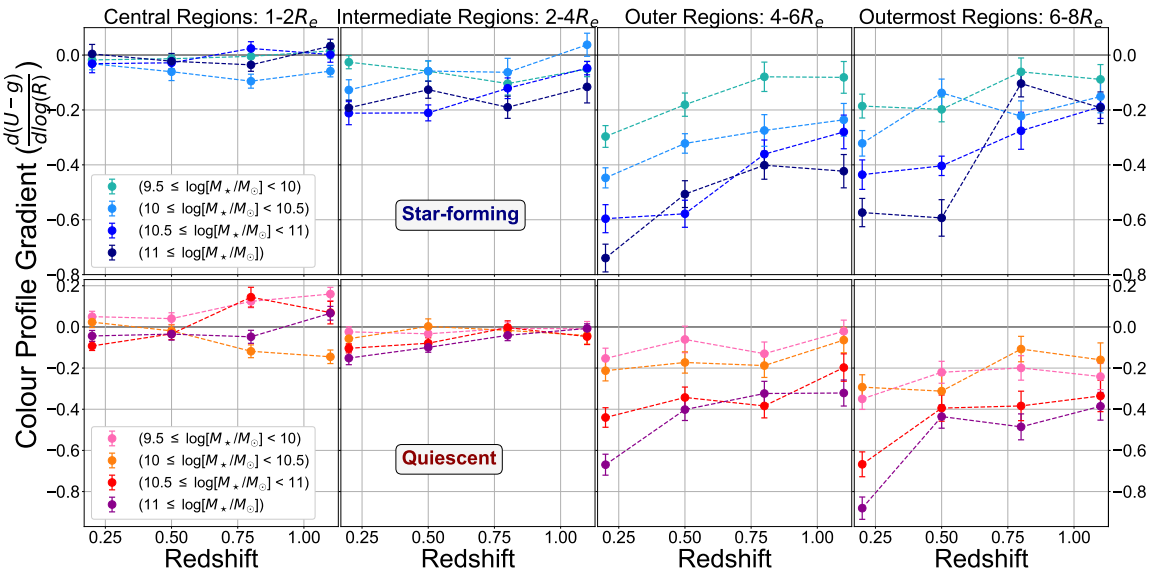

Figure 4.12. Colour gradients of our median rest-frame U-g colour profiles (Fig. 4.11) as a function of redshift, measured between different radial regions (listed in titles). Colours represent different stellar mass bins, with star-forming galaxies along the top and quiescent galaxies along the bottom. The y-axis is shared amongst panels in a row, to compare how gradients in the inner and outer regions are changing relative to one another. The evolution of the gradients is discussed in Sec. 4.3.1.

At larger distances (4-6, 6-8R_e, right two columns in Fig. 4.12), the colour gradients display more evolution across the redshift range. The outer colour gradients grow more negative with decreasing redshift and this scales with stellar mass for both the star-forming and quiescent population (darker colours have steeper colour gradients). These results imply that for galaxies in our sample, *more massive galaxies exhibit more negative colour gradients in their outer stellar halo regions, and these grow more negative over* $0.2 \leq z \leq 1.1$.

The presence of negative colour gradients has been linked to various processes that affect the evolution of galaxies. For star-forming galaxies, negative colour gradients have been used as evidence of inside-out quenching (e.g., Nelson et al. 2021). This occurs when inner galaxy regions quench first (e.g., through AGN feedback)

turning inner colours red, while outer regions remain blue and star-forming for longer (e.g., disk not yet destroyed). Considering this, our results suggest that quenching may be operating in an inside-out fashion for the star-forming galaxies in our sample.

As mentioned in Sec. 1.2.1, negative colour gradients are also linked to the accretion of stellar material during minor and very minor mergers (e.g., Lambas et al. 2012; Huang et al. 2018a; Hirschmann et al. 2015). This would be able to explain the negative colour gradients in our quiescent sample in Fig. 4.12, as the inside-out quenching scenario is less applicable to these already quenched galaxies. During a minor or very minor merger, the larger galaxy accretes bluer stellar populations from the low-mass merging companion, arising from the lower metallicities (and often younger stellar ages) associated with lower stellar mass galaxies. This material will be distributed throughout the stellar halo of the larger galaxy, causing the outer portions of colour profiles to become bluer relative to colours in the interior regions.

If accretion through minor interactions is responsible for the evolution in outer colour gradients since $z \sim 1.1$, it could explain why we see steeper more negative colour gradients in more massive galaxies in our sample. Simulations have shown the number of minor mergers experienced by galaxies should increase at higher stellar masses (e.g., Rodriguez-Gomez et al. 2016; Tacchella et al. 2019; Huško et al. 2022), which would lead to more negative colour gradients. In Sec. 5.3 we explore this impact of mergers on galaxy colour gradients further.

4.4 Normalized Rest-Frame g-Band Surface Brightness Profiles

In this section we normalize the median rest-frame g-band surface brightness profiles of different galaxy sub-populations, making it easier to directly compare profile evolution across redshift. Comparing surface brightness levels (e.g. in mag/arcsecond^2 units) in profiles from different redshift ranges is made difficult due to higher redshift images being noisier and from using different filters to trace the same rest-frame emission. Using different filters to trace rest-frame g-band emission (Sec. 3.2.1) may influence specific surface brightness values in our median profiles due to differences in filter design (see Sec. 2.1 and Fig. 2.1), and residual effects from filter-specific PSF smearing (remaining after our PSF correction procedure, Sec. 3.1.3).

To address these issues we normalize the median rest-frame g-band surface brightness profiles (Fig. 4.1 and Fig. 4.2) by their central surface brightness (μ_o), to adjust the median light profiles of different redshift ranges onto a common and relative surface brightness scale. In Fig. 4.13 we show the results of this procedure and the normalized median rest-frame g-band light profiles of our full sample. Each panel is a single stellar mass bin from either the star-forming (top row) or quiescent (bottom row) populations and shows how the median surface brightness profiles have evolved across our redshift range for that particular sub-population.

We also truncate the normalized median profiles of different redshift ranges at the same radius, using R_{lim} (see Sec. 3.2.2) for the lowest redshift bin ($z = 0.2-0.35$). This choice means some minor residual background emission might contaminate the

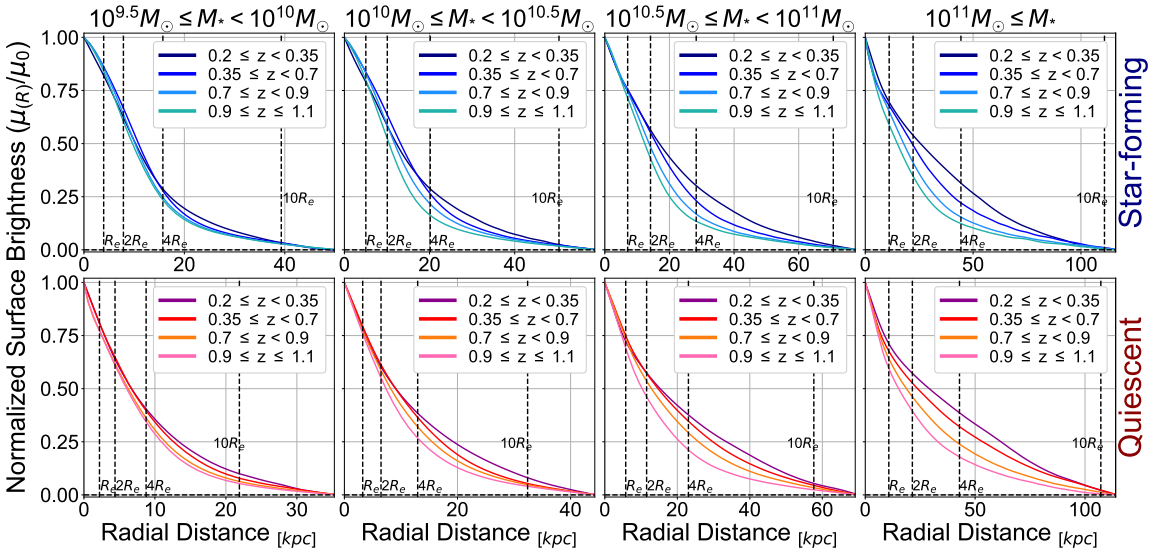

Figure 4.13. Normalized median rest-frame g-band surface brightness profiles for our entire galaxy sample. Each panel represents a different stellar mass bin (star-forming on top and quiescent on bottom) and contains the median profiles of all four redshift ranges. The dashed vertical lines show 1, 2, 4, and $10R_e$ for the lowest redshift bin, and normalized profiles are all truncated to the R_{lim} of this lowest redshift bin ($z = 0.2 - 0.35$). See Sec. 4.4 for procedural details.

outermost regions of the higher redshift profiles. However, this decision ensures we introduce no large artificial surface brightness differences in profile outskirts (which may be misinterpreted as true stellar mass assembly), by having sharp early truncations of the higher redshift profiles.

From the normalized profiles in Fig. 4.13 we can see that more massive galaxies (right-hand columns) exhibit more buildup in their light profiles since $z \sim 1.1$. The majority of this buildup occurs at larger radii (i.e. $R \gtrsim 4R_e$) for all galaxies, which we analyze in greater detail in Sec. 4.4.1. Only the high-mass galaxies ($M_\star \geq 10^{10.5}M_\odot$, two right-hand columns in Fig. 4.13) display any significant growth in the central (1-2R_e) and intermediate (2-4R_e) regions of their normalized median light profiles. Based on predictions from Hopkins et al. (2010) and Hilz et al. (2013), for high-mass quiescent galaxies this significant inner profile growth (i.e. buildup within 1-

$4R_e$) may be the result of accretion through major mergers. For high-mass star-forming galaxies, it is more likely that the growth is coming from minor and very minor mergers since star formation will also be contributing to the buildup of stellar material, and also because major mergers are more likely to destroy disk components and lead to elliptical morphologies (Sec. 1.1.2).

4.4.1 Normalized Stellar Halo Assembly

In this sub-section, we quantify the growth seen in the stellar halo regions ($R \gtrsim 4R_e$) of the normalized median rest-frame g-band surface brightness profiles from the previous section (Fig. 4.13). To do this we measure the change in total enclosed brightness (i.e. the total integrated luminosity, calculated via Eq. 3.5) specifically measured within a fixed stellar halo region (i.e. L_{halo}). This region is fixed between $4R_e$ at high redshift ($z = 0.9 - 1.1$ bin) and R_{lim} at low redshift ($z = 0.2 - 0.35$ bin).

In Fig. 4.14 we show what these enclosed (and integrated) stellar halo regions look like on the normalized median light profiles. Each panel shows a different stellar mass bin from the star-forming and quiescent samples, with the stellar haloes at high redshift ($z \sim 1.1$) shown in grey. Then with the coloured-shaded regions, we show how stellar haloes are built up across the full redshift range and where this material is distributed radially. However because of our decision to truncate all normalized median profiles of different redshift bins at the same radius (Sec. 4.4), some of the outermost growth (i.e. near the brown vertical lines in Fig. 4.14) may be underestimated for lower redshift profiles.

Figure 4.15 shows the relative increases in the integrated stellar halo light (L_{halo})

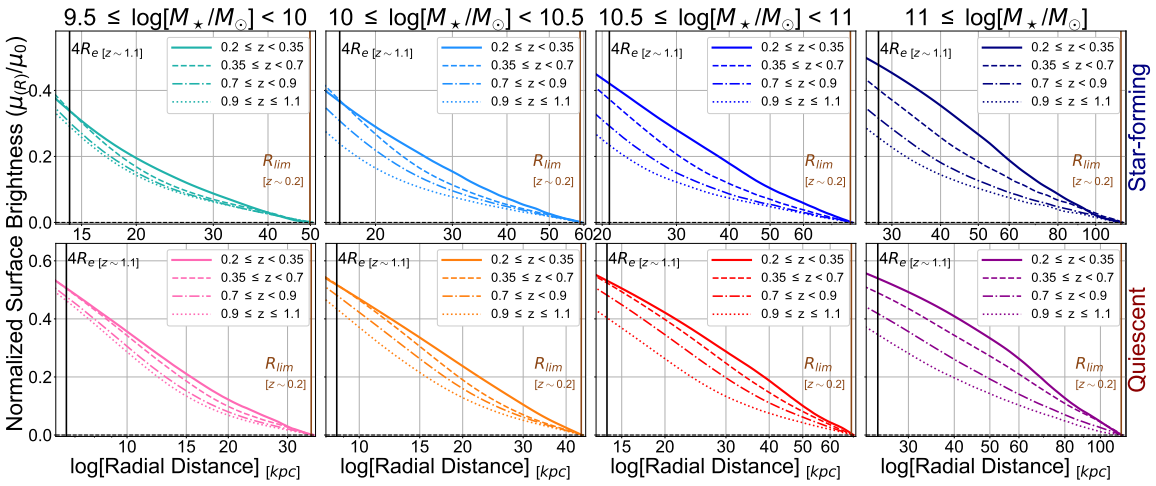

Figure 4.14. Buildup of the stellar halo regions ($R \gtrsim 4R_e$) in the normalized median rest-frame g-band surface brightness profiles from Fig. 4.13 (explained throughout Sec. 4.4). Each panel shows a different stellar mass bin from the star-forming (bluer colours) or quiescent (redder colours) population and contains all four median profiles from each redshift bin (different dashed lines in the legend). The grey-shaded region indicates the stellar halo region at high redshift, and the shaded colour regions indicate where stellar haloes have added material across the redshift range. The vertical lines indicate the limits of the fixed stellar halo regions used for measurement - $4R_e$ in black and truncation radius R_{lim} in brown.

across our redshift bins (i.e. the quantification of the coloured shaded regions in Fig. 4.14). These increases are displayed in relative units of $L_{halo\ [z=1.1]}$, which represents the integrated stellar halo light from our highest redshift bin and median profile. Table 4.1 summarizes all the increases to L_{halo} for each galaxy sub-population.

We find that more massive galaxies build up more material in their stellar halo regions since $z \sim 1.1$ (larger total increase to L_{halo} by $z \sim 0.2$ in Fig. 4.15). From the shaded stellar halo regions in Fig. 4.14 this material is distributed out to larger radii in more massive galaxies (i.e. right-hand columns show most profile growth). Low-mass galaxies ($10^{9.5} M_\odot \leq M_\star < 10^{10.5} M_\odot$) are increasing L_{halo} by a factor of ∼1.43 and ∼1.79 (for star-forming galaxies) and a factor of ∼1.31 and ∼1.58 (for quiescent galaxies) across our full redshift range. The high-mass galaxies ($M_\star \geq 10^{10.5} M_\odot$)

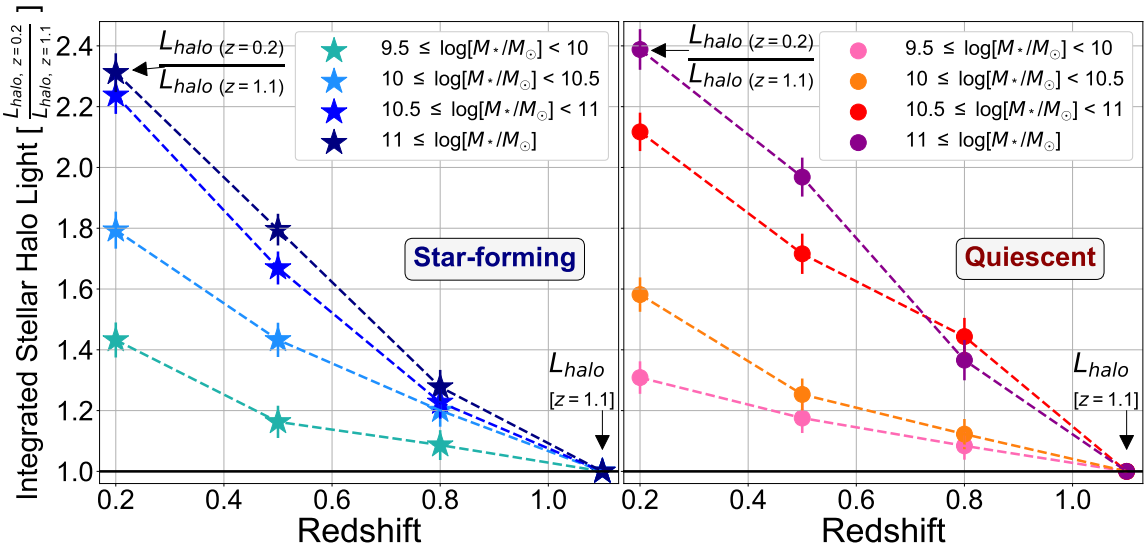

Figure 4.15. Cumulative increases in the median integrated stellar halo light (L_{halo}) from Fig. 4.14, with different stellar mass bins shown as different colours and listed in the legends. The increases are shown in units of the total enclosed surface brightness of the high redshift stellar halo ($L_{halo\ [z=1.1]}$), in order to display what fractional increase has occurred. The data points here are evenly spaced across our full redshift range ($0.2 \leq z \leq 1.1$), but represent the median profiles from our four redshift bins: $z4$=(1.1-0.9), $z3$=(0.9-0.7), $z2$=(0.7-0.35), $z1$=(0.35-0.2). Increases to L_{halo} are also compiled in Table 4.1.

instead exhibit a larger amount of growth, increasing L_{halo} by a factor of ∼2.24 and ∼2.31 (for star-forming galaxies) and a factor of ∼2.12 and ∼2.38 (for quiescent galaxies) since $z \sim 1.1$.

This slightly larger buildup of outer material in star-forming galaxies (except at $M_\star \geq 10^{11} M_\odot$) aligns with the assembly of star-forming galaxies through both in-situ and ex-situ processes. Quiescent galaxies on the other hand are not forming new stars, and so their stellar halo buildup (i.e. total increases to L_{halo}, last column Table 4.1) is more likely coming from ex-situ related accretion. Thus although our results suggest star-forming galaxies are forming the most amount of stellar mass in these outer regions from high to low redshift, quiescent galaxies may be adding more material through ex-situ assembly specifically. To further test this scenario we

quantify the contribution from in-situ star-formation for star-forming galaxies in Sec. 5.1, along with the possible contribution from the effect of progenitor bias for the quiescent population.

Star-forming Galaxies $[log(M_\star/M_\odot)]$	L_{halo} **increase** $(z4-z3)$ $[L_{halo\ z4}]$	L_{halo} **increase** $(z4-z2)$ $[L_{halo\ z4}]$	**Total** L_{halo} **increase** $(z4-z1)$ $[L_{halo\ z4}]$
$9.5 \leq M_\star < 10$	1.09 $\pm$0.02	1.17 $\pm$0.02	1.43 $\pm$0.02
$10 \leq M_\star < 10.5$	1.20 $\pm$0.02	1.43 $\pm$0.02	1.79 $\pm$0.02
$10.5 \leq M_\star < 11$	1.23 $\pm$0.02	1.67 $\pm$0.02	2.24 $\pm$0.02
$11 \leq M_\star$	1.28 $\pm$0.03	1.80 $\pm$0.03	2.31 $\pm$0.03
Quiescent Galaxies $[log(M_\star/M_\odot)]$	L_{halo} **increase** $(z4-z3)$ $[L_{halo\ z4}]$	L_{halo} **increase** $(z4-z2)$ $[L_{halo\ z4}]$	**Total** L_{halo} **increase** $(z4-z1)$ $[L_{halo\ z4}]$
$9.5 \leq M_\star < 10$	1.08 $\pm$0.02	1.18 $\pm$0.02	1.31 $\pm$0.02
$10 \leq M_\star < 10.5$	1.12 $\pm$0.02	1.25 $\pm$0.02	1.58 $\pm$0.02
$10.5 \leq M_\star < 11$	1.44 $\pm$0.03	1.72 $\pm$0.03	2.12 $\pm$0.03
$11 \leq M_\star$	1.37 $\pm$0.03	1.97 $\pm$0.03	2.38 $\pm$0.03

Table 4.1: Cumulative increases of the integrated stellar halo surface brightness (L_{halo}), for the normalized median rest-frame g-band surface brightness profiles shown in Fig. 4.14. Increases are shown as a relative increase to the highest redshift L_{halo} for that galaxy sub-population (see Sec. 4.4.1 for details). The redshift ranges corresponding to the header labels e.g. ($z4$-$z3$) are: $z4$=(1.1-0.9), $z3$=(0.9-0.7), $z2$=(0.7-0.35), $z1$=(0.35-0.2). Errors come from the small bootstrapped errors on the median brightness profiles (Sec. 3.2.2).

Chapter 5

Discussion

Throughout our results in Chap. 4, we see multiple signs that mergers and ex-situ accretion have likely influenced the evolution of galaxies in our sample since $z \sim 1.1$. We next perform additional analyses and comparisons with predictions, in order to further investigate the link between our observed results and the ex-situ phase of galaxy assembly (one of our main objectives outlined in Sec. 1.3).

In Sec. 5.1 we investigate how much of the normalized stellar halo assembly seen in Sec. 4.4.1 (Fig. 4.14) could come from in-situ star formation for star-forming galaxies (Sec. 1.1.1), and the effect of progenitor bias for quiescent galaxies (Sec. 1.1.3).

In Sec. 5.2 we measure the evolution in median sizes (R_e) with redshift for different galaxy sub-populations in our sample, to investigate the influence of ex-situ accretion. We also investigate the link between the pivot mass (M_p, discussed in Sec. 3.2.1) and accelerated size growth in more massive galaxies, by fitting size-stellar

mass relations (R_e vs. $M_\star$, Shen et al. 2003; Zhang & Zaritsky 2016; Mercier et al. 2022) for lower and higher stellar mass galaxies separately. This pivot mass has been linked to a transition into an ex-situ-dominated stage of assembly (e.g., Mowla et al. 2019a; Kawinwanichakij et al. 2021).

To explore the impact of different types of mergers on galaxy colour gradients, in Sec. 5.3 we compare our median rest-frame U-g colour profile gradients with the results from Hirschmann et al. (2015). These authors investigate how different merger types (i.e. minor vs. major, Sec. 1.1.2) affect the evolution of U-g colour profiles and colour gradients in simulated galaxies.

Finally, in Sec. 5.4 we investigate the role of minor and major mergers in driving the stellar mass assembly of the massive ($M_\star \geq 10^{11} M_\odot$) quiescent galaxy population since $z \sim 1.1$. Using the brightness profile normalization procedure of van Dokkum et al. (2010), we estimate how much stellar mass is accumulated in the massive quiescent galaxies in our sample, based on our median light profile evolution over $0.2 \leq z \leq 1.1$. We then use observed stellar mass-accretion rates due to different types of mergers from Conselice et al. (2022), to test whether the total amount of stellar mass assembly we estimated can be explained through accretion via minor or major mergers.

5.1 Contributions to Stellar Halo Growth

In Sec. 4.4.1 we analyze how different galaxy sub-populations build up their stellar halo regions ($R \gtrsim 4R_e$) since $z \sim 1.1$. In this section, we aim to quantify how much

of the total stellar halo growth (i.e. the total increases to L_{halo}, Fig. 4.15) can be attributed to in-situ star formation (Sec. 1.1.1) or the effect of progenitor bias (Sec. 1.1.3) for star-forming and quiescent galaxies, respectively.

We discuss our procedure for calculating the contributions from star formation in Sec. 5.1.1, and contributions from progenitor bias in Sec. 5.1.2. In Sec. 5.1.3 we present the results of both procedures and any remaining increases to L_{halo}. Finally in Sec. 5.1.4 we compare these remaining fractions of assembled stellar halo material with predictions of stellar halo ex-situ fractions from Cook et al. (2016).

5.1.1 Contributions From Star Formation

For contributions from star formation, we calculate median star formation rates (SFR, in $M_{\odot}$/yr) for each star-forming stellar mass bin (Table 3.1). The star formation rates for individual galaxies come from the HSC+CLAUDS catalogues (Sec. 2.2, Desprez et al. 2023). For each stellar mass bin, we calculate four separate median SFRs for our four redshift bins. Next, taking the time in years covered by an individual redshift bin (i.e. the Δt that corresponds to Δz), and multiplying it by the median SFR for that redshift bin, we estimate an amount of stellar mass (in $M_{\odot}$) formed over the given redshift interval. By adding up the amounts formed across all four redshift bins, we obtain the total possible amount of stellar mass each of our star-forming mass bins could form through star formation over $0.2 \leq z \leq 1.1$. Since we assume that the SFRs from the catalogue are constant throughout a galaxy (when they are likely lower in galaxy outskirts), the estimates we obtain for total stellar mass formed through star formation are considered upper-limit predictions.

Next, we use a stellar mass-to-light ratio (rest-frame g-band) to convert this total stellar mass formed into luminosity. For each of our four stellar mass bins, we utilize a different $M_\star/L_g$ ratio based on their rest-frame U-g colours. To obtain these ratios we utilize the mean U-g colour within the stellar halo region (i.e. $R \geq 4R_e$) of our median rest-frame U-g colour profiles (Fig. 4.11). We then utilize the relation between U-g colour and $M_\star/L_g$ ratio provided by Szomoru et al. (2013, Fig. 1), to obtain a ratio that corresponds to our measured stellar halo colour.

With these estimated amounts of total rest-frame g-band luminosity that could arise from star formation for each of the stellar mass bins in our star-forming sample, we calculate a similar increase to the integrated light within the stellar halo region (i.e. increase to L_{halo}) as was done in Sec. 4.4.1 and Fig. 4.15. In Sec. 5.1.3 we present the results of this procedure.

5.1.2 Contributions From Progenitor Bias

For contributions from progenitor bias (Sec. 1.1.3), we utilize the work of Donnari et al. (2019, 2021) on the predicted change in quenched galaxy fractions over our redshift range. The authors study galaxies in the IllustrisTNG simulation and use a similar colour-colour diagram cut (a UVJ cut) as we do in this work to separate star-forming and quiescent galaxy samples, except for the highest stellar mass galaxies ($M_\star \geq 10^{11} M_\odot$, our highest mass bin) where a cut to SFR[1] is used by Donnari et al.

[1]For the three lower stellar mass bins, Donnari et al. (2019) used both a UVJ cut and a SFR cut, which produced very similar quenched fraction results. Therefore we do not believe the SFR cut used by Donnari et al. (2021) for our highest stellar mass bin is introducing any bias in our results when adopting their predicted quenched fraction changes.

(2021). The change in quenched fraction we obtain for our four stellar mass bins are 15%, 20%, 25%, and 15% (for our low to high mass bins respectively, Table 3.1). This gives a percentage of quiescent galaxies in the low redshift bin ($z = 0.2 - 0.35$), that may be recently quenched star-forming galaxies that have entered the sample at later times.

We then remove these percentages of individual brightness profiles from our four low redshift quiescent galaxy mass bins and recalculate median profiles. We preferentially remove individual profiles with the largest sizes (R_e), as it is well-established that star-forming galaxies are larger than quiescent galaxies of the same stellar mass (e.g., van der Wel et al. 2014; Mowla et al. 2019b; Kawinwanichakij et al. 2021). With these adjusted median profiles we then repeat the entire normalization procedure outlined in Sec. 4.4, which leads to the measured total increases in L_{halo} (Fig. 4.15). The contributions from progenitor bias are defined as the difference between the original increase to L_{halo} over $0.2 \leq z \leq 1.1$ (i.e. Fig. 4.15, or last column of Table 4.1), and the increase calculated with these profiles adjusted for progenitor bias. In Sec. 5.1.3 we present the results of this procedure.

5.1.3 Excess Stellar Halo Buildup

In Fig. 5.1 we show how much of the total assembled stellar halo material (Fig. 4.14) can be attributed to either in-situ star formation or the effect of progenitor bias for star-forming and quiescent galaxies, respectively. The total growth in L_{halo} over $0.2 \leq z \leq 1.1$ measured for each stellar mass bin is represented in Fig. 5.1 by the full bars (i.e. horizontal line at an assembled fraction of 1.0). The possible contributions

from star formation and progenitor bias for each sub-population are represented by the amount of grey in each bar. The coloured portions represent how much stellar mass assembly remains unaccounted for (percentages in text boxes of Fig. 5.1).

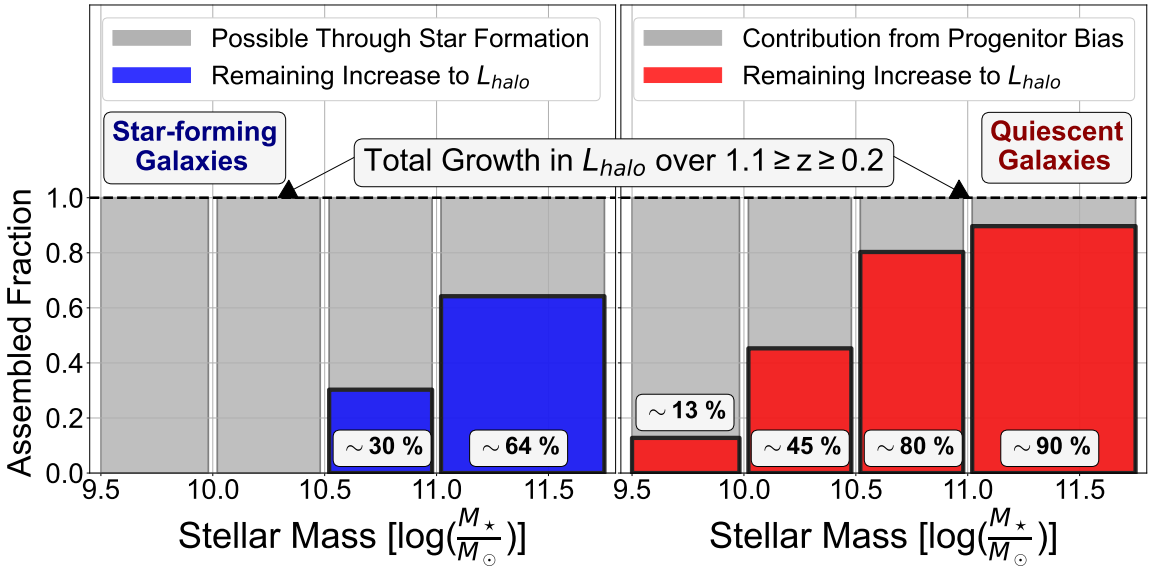

Figure 5.1. Fraction of assembled stellar halo material (Fig. 4.14), that can be attributed to star formation (SF) or the effect of progenitor bias (PB), for star-forming and quiescent galaxies, respectively (details in Sec. 5.1). Grey regions show the contributions from SF and PB, while the blue and red coloured regions represent the fraction of remaining stellar halo material that requires an additional assembly mechanism (shown as percentages in the small grey text boxes). Errors (not shown) are small ($\sigma_y \lesssim$ 0.02-0.03) due to the small bootstrapped uncertainties on median surface brightness profiles (Sec. 3.2.2).

We find that low-mass ($10^{9.5} M_\odot \leq M_\star < 10^{10.5} M_\odot$) star-forming galaxies can grow solely via star formation (two full grey bars, left-hand plot in Fig. 5.1). For more massive star-forming galaxies there is a fraction of assembled stellar halo material that cannot arise from star formation alone. That fraction increases with stellar mass and ranges from ∼0.30 to ∼0.64 for star-forming galaxies of $10^{10.5} M_\odot \leq M_\star < 10^{11} M_\odot$ and $M_\star \geq 10^{11} M_\odot$, respectively (two blue bars, left-hand plot in Fig. 5.1).

There is a strong possibility that this remaining growth in massive star-forming galaxies is resulting from ex-situ accretion as we show in Sec. 5.1.4. Other processes

that may affect the stellar mass assembly in these outer stellar halo regions are inefficient at producing this amount of remaining growth (Hopkins et al. 2010; Hilz et al. 2013; Cook et al. 2016). As demonstrated by Hopkins et al. (2010, their Fig. 2), internal processes such as adiabatic expansion or feedback mechanisms alone cannot account for the growth in outer brightness profiles that we observe (and that would cause the remaining assembled fractions in Fig. 5.1). Additionally, we can infer that the stellar migration mechanism identified in the simulations of Boecker et al. (2023) would also be insufficient at building up these outer regions, since this causes stars to migrate away from these extended distances into the innermost regions (< 1 kpc) of galaxies.

As mentioned in Sec. 1.1.2, minor mergers are expected to disrupt disk structures far less than major mergers (Jackson et al. 2020, 2022), and they also contribute less material (via accretion) with each interaction (Hopkins et al. 2010; Lambas et al. 2012). For these reasons, it seems likely that the remaining fractions of assembled stellar halo material of massive ($M_\star \geq 10^{10.5} M_\odot$) star-forming galaxies in our sample (i.e. $\sim$0.30 and $\sim$0.64) are the product of a series of minor and very minor mergers (Sec. 1.1.2).

From the right-hand panel in Fig. 5.1 (red portions of bars), we see that quiescent galaxies of all four stellar mass bins have fractions of assembled stellar material that remain after we account for the possible effect of progenitor bias ($\sim$0.13, $\sim$0.45, $\sim$0.80, $\sim$0.90, low to high stellar mass bins respectively). Buildup through ex-situ accretion is the most likely explanation for this observed growth, particularly for the high-mass quiescent galaxies which display significant remaining fractions of assembled material.

For low-mass ($10^{9.5} M_{\odot} \leq M_{\star} < 10^{10.5} M_{\odot}$) quiescent galaxies, minor and very minor mergers could completely explain the amount of buildup we measure (Hopkins et al. 2010; Rodriguez-Gomez et al. 2016; Tacchella et al. 2019; Huško et al. 2022). However, for more massive quiescent galaxies ($M_{\star} \geq 10^{10.5} M_{\odot}$), the higher fractions of assembled material that remain (i.e. ∼0.8-0.9, Fig. 5.1) indicate that major mergers may be contributing to the growth within the population. This is because simulations have shown that minor mergers alone are insufficient at building up similarly large ex-situ fractions, capable of producing ex-situ fractions of ∼0.5 or below depending on the simulation (e.g., Rodriguez-Gomez et al. 2016; Huško et al. 2022; Cannarozzo et al. 2022). The amount of minor or very minor mergers needed to build up such large ex-situ fractions would greatly exceed the predicted merger rates for these minor interactions.

5.1.4 Comparing With Predicted Ex-Situ Fractions

To further demonstrate that the remaining fractions of assembled material shown in Fig. 5.1 (blue and red portions of histograms) are arising from ex-situ accretion, we compare our results with the predicted stellar halo ex-situ fractions from the work of Cook et al. (2016). In their work studying ex-situ assembly in simulated galaxies, these authors identify a linear relationship between the surface brightness profile gradient of a galaxy (measured within 2-4R_e), and the stellar halo ex-situ stellar mass fraction of the galaxy (i.e. the $f_{ex} - \nabla\Sigma_v$ relation, see their Fig. 4).

In Fig. 5.2 we plot the $f_{ex} - \nabla\Sigma_v$ relation (grey band, with dashed lines as $\pm 1\sigma$), along with a wider region (shown in red) that encompasses the full distribution of

galaxies from the sample of Cook et al. (2016). We then take the intermediate region (2-4R$_e$) profile gradients from our median rest-frame g-band surface brightness profiles (Fig. 4.7), and the remaining fractions of assembled stellar halo material from Fig. 5.1 in the previous sub-section. In Fig. 5.2 we plot these profile gradients on the x-axis and our assembled stellar halo fractions on the y-axis, to see where galaxies from different bins lie along the relation from Cook et al. (2016).

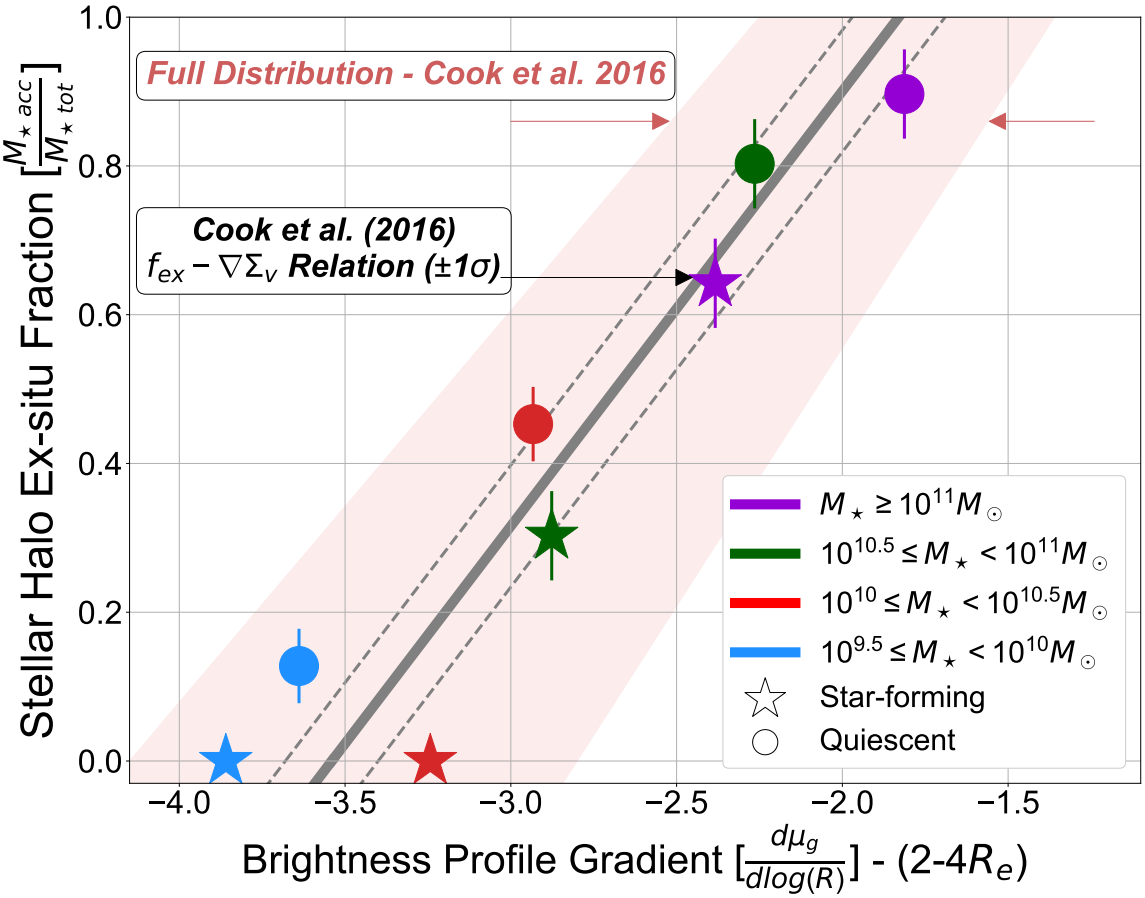

Figure 5.2. Comparison of our estimated stellar halo ex-situ fractions (percentages from Fig. 5.1) and our median brightness profile gradients within 2-4R_e (shown in Fig. 4.7), with those predicted from the $f_{ex} - \nabla\Sigma_v$ relation (grey band, with dashed lines showing $\pm 1\sigma$) of Cook et al. (2016). Different colours represent different stellar mass bins (in legend), with stars and circles representing star-forming and quiescent galaxies, respectively. The larger red region encompasses the entire distribution of galaxies analyzed by Cook et al. (2016). Errors on data points come from small bootstrapped errors on median profiles (σ_x much smaller than symbol sizes). See Sec. 5.1.3 for discussion.

We find that the remaining fractions of assembled material we estimate after accounting for contributions from star formation and progenitor bias (percentages in Fig. 5.1), are in good agreement with predicted stellar halo ex-situ fractions in Fig. 5.2. In particular, quiescent galaxies in all four stellar mass bins (coloured circles in Fig. 5.2) align very well (within 1-2σ) with the predicted linear relation (grey band and dashed lines). Thus, both the brightness profile gradients (Fig. 4.7) and remaining increases to L_{halo} (Fig. 5.1) that we measure indicate that quiescent galaxies in our sample are growing through ex-situ accretion.

Star-forming galaxies of higher stellar masses (green and purple stars in Fig. 5.2) also agree very well (within $\sim 1\sigma$) with the predicted linear relation, demonstrating that our remaining fractions of assembled material (from Fig. 5.1) are in good agreement with predicted ex-situ fractions. The low-mass ($10^{9.5} M_{\odot} \leq M_{\star} < 10^{10.5} M_{\odot}$) star-forming galaxies (blue and red stars) did not have any remaining stellar halo assembly (i.e. full grey bars in Fig. 5.1), and as such they contain 0% ex-situ fractions here in Fig. 5.2. However, this is still in agreement with predictions from Cook et al. (2016) as the authors also identified $\sim$0% ex-situ fractions (e.g., red region in Fig. 5.2). In future work, if we can better model the exact amount of growth through star formation for galaxies at these lower masses ($10^{9.5} M_{\odot} \leq M_{\star} < 10^{10.5} M_{\odot}$) we may be able to identify small ex-situ fractions if they exist.

This comparison with predictions from Cook et al. (2016) in Fig. 5.2 further supports our statement that the remaining fractions of assembled stellar halo material identified in Sec. 5.1.3 (red and blue histograms of Fig. 5.1), are a result of ex-situ assembly. Our results throughout this section imply that *more massive galaxies in our sample accrete more ex-situ material*, and that *quiescent galaxies contain higher*

ex-situ fractions than star-forming galaxies of similar stellar masses.

5.2 Influence of Ex-Situ Assembly on Galaxy Sizes

Galaxy scaling relations provide important constraints for models of galaxy formation and evolution (e.g., Stone et al. 2021; Zhang & Zaritsky 2016; Mercier et al. 2022; Trayford & Schaye 2019). One of these important scaling relations is the size-stellar mass relation ($R_e \propto {M_\star}^\alpha$) of galaxies (Shen et al. 2003; Suess et al. 2021; Trujillo et al. 2007; Mowla et al. 2019b; Damjanov et al. 2015, 2022b; Kawinwanichakij et al. 2021). Observations show that galaxies of higher stellar masses (above a pivot mass $M_p \sim 10^{10.5\pm0.5} M_\odot$) follow a steeper size-stellar mass relation (i.e. steeper slope to the fit) than low-mass galaxies (e.g., Damjanov et al. 2022a; Mowla et al. 2019a; Lange et al. 2015; Kawinwanichakij et al. 2021). The cause of this steeper relation and the enhanced growth in size seen in more massive galaxies have been attributed to an increase in merger activity and accretion of ex-situ material (e.g., Trujillo et al. 2007, 2011; Hopkins et al. 2010; van der Wel et al. 2014; Kawinwanichakij et al. 2021; Damjanov et al. 2022a,b). This is particularly true for quiescent galaxies, as the observed size growth cannot result from their low levels of star formation. In Sec. 5.2.1 we analyze the size-stellar mass relations of galaxies in our sample and investigate how the relations differ for high-mass galaxies above a pivot mass of $M_p = 10^{10.5} M_\odot$.

Another commonly studied trend in galaxy sizes (R_e) is the evolution of median sizes with redshift (e.g., van der Wel et al. 2014; Mowla et al. 2019b; Kawinwanichakij et al. 2021). As demonstrated by Hopkins et al. (2010, their Fig. 3), different types

of mergers (Sec. 1.1.2), alternative processes (e.g. adiabatic expansion, Sec. 1.1.3), and observational effects, can influence how sizes evolve with decreasing redshift. However, each of these effects is expected to exert a different influence on overall size growth. In Sec. 5.2.2, we measure how the median sizes (R_e) of galaxies in our sample (i.e. different stellar mass bins, Table 3.1) have evolved over the full redshift range, to probe which physical processes are driving their size growth.

5.2.1 Size-Stellar Mass Relations

To investigate the size growth of galaxies in our sample, we fit linear size-stellar mass relations (in log space) for each of our four redshift ranges (Table 3.1). To demonstrate that higher stellar mass galaxies follow steeper relations we use a piecewise linear function with the effective radius ($\log R_e$) given by

$$\log R_e = \begin{cases} \gamma \cdot \log M_\star + [\log R_p - (\gamma \cdot \log M_p)], & \text{if } M_\star < M_p \\ \beta \cdot \log M_\star + [\log R_p - (\beta \cdot \log M_p)], & \text{if } M_\star \geq M_p \end{cases}, \tag{5.1}$$

where the pivot mass (M_p) is set to $M_p = 10^{10.5} M_\odot$ as discussed in Sec. 3.2.1 (i.e. the split between our lower and upper two stellar mass bins), and the free parameter R_p represents the effective radius at the pivot mass. In Eq. 5.1, γ and β represent the slopes of the fits to the lower ($10^{9.5} M_\odot \leq M_\star < 10^{10.5} M_\odot$) and higher ($M_\star \geq 10^{10.5} M_\odot$) stellar mass galaxies, respectively. Figure 5.3 shows the relations for the star-forming and quiescent populations in each of our four redshift ranges, and Table 5.1 lists the parameters of the fit.

At all stellar masses and redshifts we probe, we find that quiescent galaxies

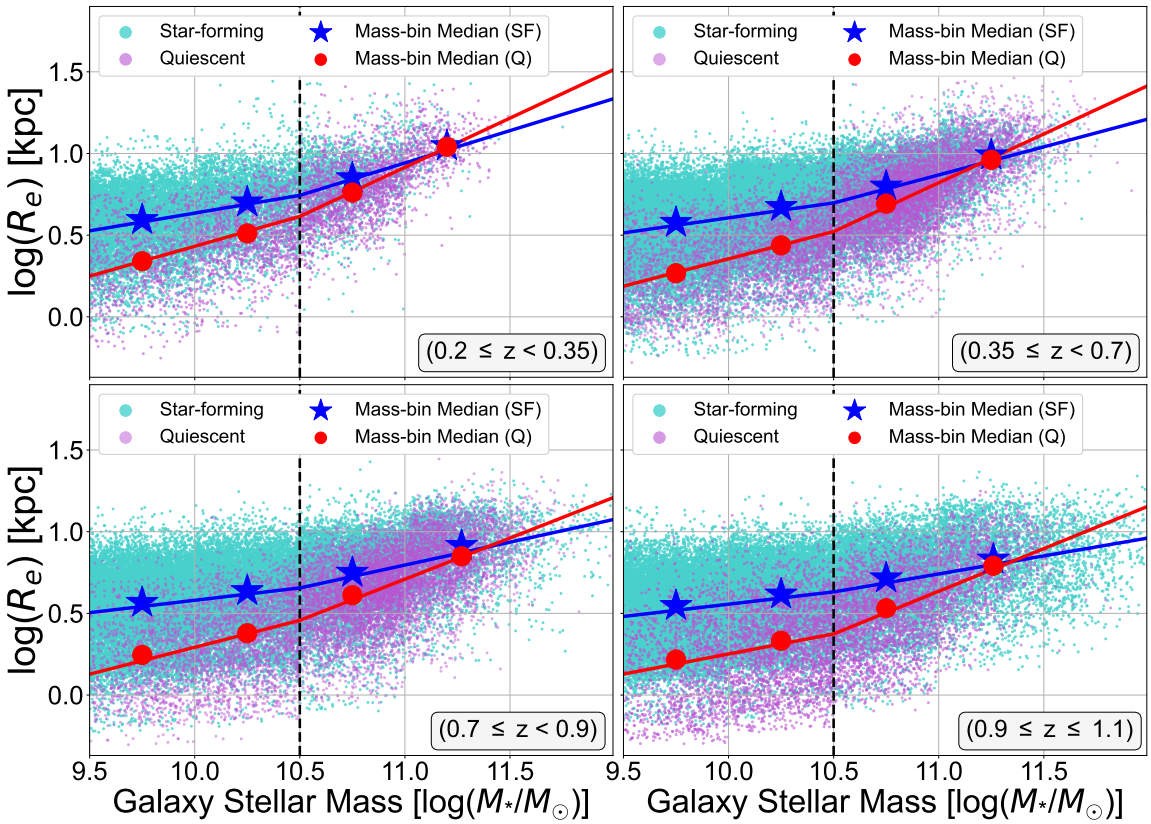

Figure 5.3. Size-stellar mass (R_e - $M_\star$) relations (blue & red solid lines) for our quiescent (pink dots) and star-forming (cyan dots) galaxies. Each subplot represents one of our four redshift ranges (labelled in the bottom-right corners). Large blue stars and red circles represent median sizes for our four stellar mass bins (see Table 3.1). The dashed vertical line splits our lower and higher two stellar mass bins at the pivot mass ($M_p = 10^{10.5} M_\odot$) of the fitted relation. We report fitting parameters in Table 5.1.

always follow a steeper size-stellar mass relation than star-forming galaxies (solid red and blue lines in Fig. 5.3), in good agreement with previous studies (e.g. van der Wel et al. 2014; Mowla et al. 2019b; Kawinwanichakij et al. 2021). This is particularly noticeable for higher stellar mass galaxies above the pivot mass, where the solid red lines cross over the solid blue lines in Fig. 5.3.

For both our star-forming and quiescent galaxy samples, high-mass galaxies ($M_\star \geq 10^{10.5} M_\odot$) above the pivot mass follow steeper size-stellar mass relations than

Redshift Range (Star-forming Sample)	γ	β	$\log(R_p)$ [kpc]
$0.2 \leq z < 0.35$	0.217 ±0.01	0.396 ±0.02	0.744 ±0.01
$0.35 \leq z < 0.7$	0.183 ±0.01	0.343 ±0.01	0.697 ±0.01
$0.7 \leq z < 0.9$	0.151 ±0.01	0.281 ±0.01	0.655 ±0.01
$0.9 \leq z \leq 1.1$	0.150 ±0.01	0.221 ±0.01	0.631 ±0.01
Redshift Range (Quiescent Sample)	γ	β	$\log(R_p)$ [kpc]
$0.2 \leq z < 0.35$	0.365 ±0.01	0.602 ±0.02	0.614 ±0.01
$0.35 \leq z < 0.7$	0.334 ±0.01	0.598 ±0.01	0.522 ±0.01
$0.7 \leq z < 0.9$	0.329 ±0.01	0.504 ±0.01	0.457 ±0.01
$0.9 \leq z \leq 1.1$	0.246 ±0.01	0.523 ±0.01	0.374 ±0.01

Table 5.1: Fitting parameters of size-stellar mass relations shown in Fig. 5.3 and fit with Eq. 5.1. The parameters γ and β represent the slopes of the fits to the lower ($10^{9.5} M_\odot \leq M_\star < 10^{10.5} M_\odot$) and higher ($M_\star \geq 10^{10.5} M_\odot$) stellar mass galaxies, respectively. The free parameter R_p represents the effective radius at the pivot mass ($M_p = 10^{10.5} M_\odot$).

low-mass ($10^{9.5} M_\odot \leq M_\star < 10^{10.5} M_\odot$) galaxies (compare γ and β values along a row in Table 5.1). Steeper slopes above the pivot mass have been linked to an increased influence of merger-driven growth (e.g., Hilz et al. 2013; Hopkins et al. 2010; Kawinwanichakij et al. 2021), implying that massive galaxies in our sample are experiencing more ex-situ accretion than low-mass galaxies which is driving their accelerated size growth. We reach this same conclusion in the previous section based on the analysis of the growth in L_{halo} of more massive galaxies in our sample (Sec. 5.1).

The size-stellar mass relation slopes also get steeper with decreasing redshift for both the star-forming and quiescent galaxy populations in our sample (compare γ or β values along a column in Table 5.1). Steeper size-mass relation slopes at lower redshifts are also seen in the late-type galaxy sample of van der Wel et al. (2014), and in the massive star-forming galaxies (above the pivot mass) in Kawinwanichakij et al. (2021). A steeper slope of the size-stellar mass relation at lower redshifts (i.e.

$z \lesssim 0.2$) has been linked to an increased influence of mergers (e.g., Hilz et al. 2013; Hopkins et al. 2010; Kawinwanichakij et al. 2021), particularly for higher stellar mass galaxies. At the low-mass end (i.e. below the pivot mass) the steeper slopes at lower redshifts may also be explained through the growth of bulge components in star-forming galaxies, or the effect of progenitor bias for quiescent galaxies (e.g., George 2020; Kawinwanichakij et al. 2021).

5.2.2 Evolution of Median Galaxy Sizes

Using the median sizes we measure for our galaxy sub-populations (blue stars and red circles in Fig. 5.3), in this subsection we examine size growth with decreasing redshift for star-forming and quiescent galaxies in our four stellar mass bins (Table 3.1). Following the literature (e.g. van der Wel et al. 2014; Mowla et al. 2019b; Kawinwanichakij et al. 2021) we fit a power law function to the median size evolution, where the effective radius (R_e, in kpc) as a function of redshift is given by

$$R_e = A(1+z)^{-\alpha}. \tag{5.2}$$

The intercept (A) in Eq. 5.2 represents the median size (in kpc) at $z = 0.2$ for each stellar mass bin. The exponent (α) represents the slope of the evolution with larger values implying faster growth in size with decreasing redshift. We show the fitting results as coloured dashed lines in Fig. 5.4, and in Table 5.2 we summarize the fitting parameters we obtain.

We find a trend in stellar mass in both the star-forming and quiescent populations, where more massive galaxies follow a steeper evolution in size over our full

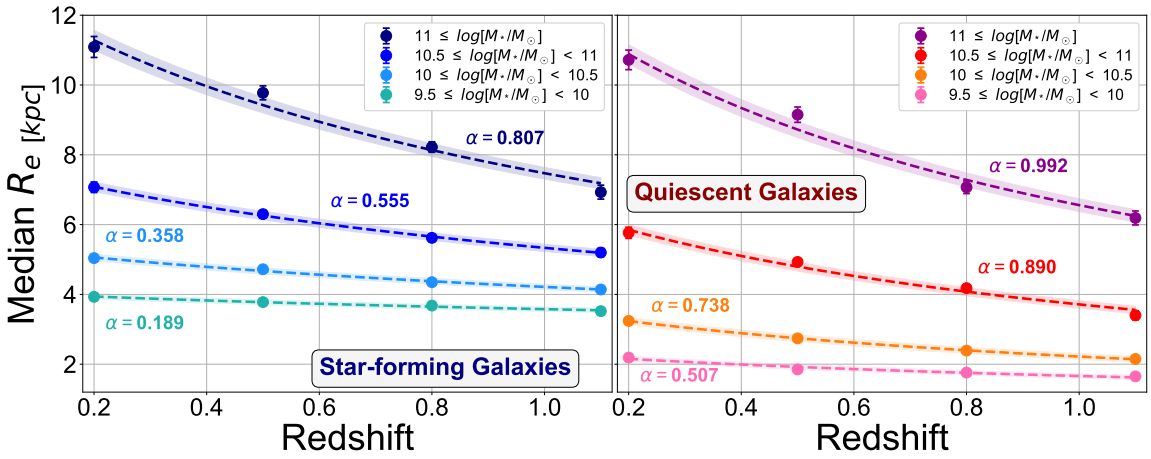

Figure 5.4. Evolution of median sizes (R_e) across redshift for our galaxy sample, split into star-forming (left) and quiescent (right) galaxies. Different colours represent different stellar mass bins (shown in the legend). The evolution tracks (dashed lines) are fitted with a power law function (Eq. 5.2), with the exponents (α) displayed as colour-coded text along different tracks. The shaded coloured bands represent the errors on the median sizes (see Sec. 3.2.4).

Galaxy Population $[log(M_\star/M_\odot)]$	A [kpc]	α
Star-forming		
$9.5 \leq M_\star < 10$	4.08 $\pm$0.1	0.189 $\pm$0.02
$10 \leq M_\star < 10.5$	5.40 $\pm$0.1	0.358 $\pm$0.02
$10.5 \leq M_\star < 11$	7.84 $\pm$0.21	0.555 $\pm$0.03
$11 \leq M_\star$	13.07 $\pm$0.53	0.807 $\pm$0.08
Quiescent		
$9.5 \leq M_\star < 10$	2.38 $\pm$0.1	0.507 $\pm$0.08
$10 \leq M_\star < 10.5$	3.70 $\pm$0.15	0.738 $\pm$0.03
$10.5 \leq M_\star < 11$	6.88 $\pm$0.28	0.890 $\pm$0.09
$11 \leq M_\star$	13.04 $\pm$0.6	0.992 $\pm$0.1

Table 5.2: Fitting parameters obtained from the median size evolution shown in Fig. 5.4. See Sec. 5.2.2 for details.

redshift range (darker colours show steeper fits in Fig. 5.4). This is in good agreement with previous observational studies (e.g., van der Wel et al. 2014; Mowla et al. 2019a,b; Kawinwanichakij et al. 2021), and highlights that *more massive galaxies are growing in size at a faster rate since* $z \sim 1.1$. For all stellar masses we probe, the

quiescent galaxies follow a faster size evolution than star-forming galaxies of similar stellar masses (α values in Fig. 5.4 and Table 5.2), also in agreement with previous studies in the literature (e.g., van der Wel et al. 2014; Kawinwanichakij et al. 2021).

Based on theoretical predictions from Hopkins et al. (2010), the evolution in size we see for low-mass quiescent galaxies ($10^{9.5} M_{\odot} \leq M_{\star} < 10^{10.5} M_{\odot}$) could be a result of accretion through minor mergers. The expected size increase as a function of redshift from these minor interactions would be sufficient to explain the evolution in median sizes we see for these galaxy populations. However, it is important to not discount the possible influence from additional mechanisms, as these authors also show that observational effects, $M_{\star}/L$ gradients, and adiabatic expansion (Sec. 1.1.3) can all have similar influences on size evolution. More massive quiescent galaxies ($M_{\star} \geq 10^{10.5} M_{\odot}$) exhibit a steep evolution in size, which based on predictions may be arising from a combination of both minor and major mergers occurring within the sub-populations.

For star-forming galaxies, it is possible that some of their size growth is a result of in-situ star formation, and therefore we may need less of a contribution from ex-situ accretion to account for the total evolution in median sizes. However, as demonstrated by Wilman et al. (2020), growth through star formation may not be able to account for the total size growth in the star-forming population and additional mechanisms such as mergers may be required. For the low-mass star-forming galaxies in our sample ($10^{9.5} M_{\odot} \leq M_{\star} < 10^{10.5} M_{\odot}$), it is possible their relatively shallow evolution in size may not require any minor mergers (as opposed to the low-mass quiescent galaxies). For our high-mass star-forming galaxies ($M_{\star} \geq 10^{10.5} M_{\odot}$), their steeper evolution in size may require an additional size growth mechanism beyond star formation (i.e.

minor mergers). However, they likely do not require the large size increase expected from major mergers, as is the case with the size evolution for the high-mass quiescent galaxies.

5.3 Impact of Mergers on Colour Gradients

In this section, we explore how a range of merger-driven assembly histories may impact the rest-frame U-g colour gradients of galaxies we measure at low redshift (Fig. 4.12). To do this, we compare our measured U-g colour gradients with the colour gradients based on simulated galaxies of Hirschmann et al. (2015). These authors create 10 different massive ($M_{\star}{\sim}10^{11}M_{\odot}$) galaxy models and simulate their evolution from $z = 2$ to $z = 0$ (see their Sec. 2 for full details of the simulations). A key difference between the models is the number of major and minor mergers each model experiences since $z = 2$. The authors extract rest-frame $u - g$ colour profiles from their model galaxies (their Fig. 8) and measure colour gradients at $z = 2$, $z = 1$, and $z = 0$. These gradients are measured specifically between a stellar halo region at 2-6R_e.

For comparison with our results, we select three specific low redshift ($z = 0$) $u-g$ colour profile gradients from Hirschmann et al. (2015, their Table 4). These three gradient values encompass the full range of possible assembly histories throughout all the models. The first gradient value comes from a major merger-dominated galaxy model (i.e. ex-situ stellar mass assembly dominated completely by growth through major mergers). In this model, a galaxy experiences only one single minor merger but two major mergers since $z = 1.1$ (our redshift limit). In the second model, the

assembly history of the galaxy is completely dominated by minor mergers, and the galaxy experiences zero major mergers and six minor mergers since $z = 1.1$. The last gradient value we select is the mean gradient across all ten galaxy models, which is representative of a range of merger histories with a mixture of contributions from major and minor mergers. This model acts as the midway point between the other two extremes we choose (i.e. minor and major merger-dominated models).

Next, we measure the gradients of our median rest-frame U-g colour profiles within the same stellar halo region (2-6R_e) as in Hirschmann et al. (2015). We did this only for the two higher stellar mass bins ($M_\star \geq 10^{10.5} M_\odot$), as they are more comparable to the model galaxies. Figure 5.5 shows the colour gradients we measure as a function of redshift, alongside the $z = 0$ model gradients we selected (black symbols in Fig. 5.5). As our median colour profile coverage does not extend to $z = 0$, we linearly extrapolate our four median gradient points down to $z = 0$ to infer how colour gradients may evolve by $z = 0$ (dashed lines in Fig. 5.5).

From the purple and blue lines in Fig. 5.5, we see the low redshift U-g colour gradients ($z = 0$ extrapolated values) of massive star-forming galaxies align with the minor merger-dominated model gradient (black pentagon in Fig. 5.5). This would suggest that minor mergers have a large effect on the colour evolution in the stellar halo regions of massive star-forming galaxies.

From the green and red lines in Fig. 5.5, we see that the extrapolated $z = 0$ colour gradients of massive quiescent galaxies agree more with the gradients representing mixed-merger and major merger-dominated assembly histories (i.e. the black square and triangle in Fig. 5.5). From the merger histories of the galaxy models (see Fig. 2 in

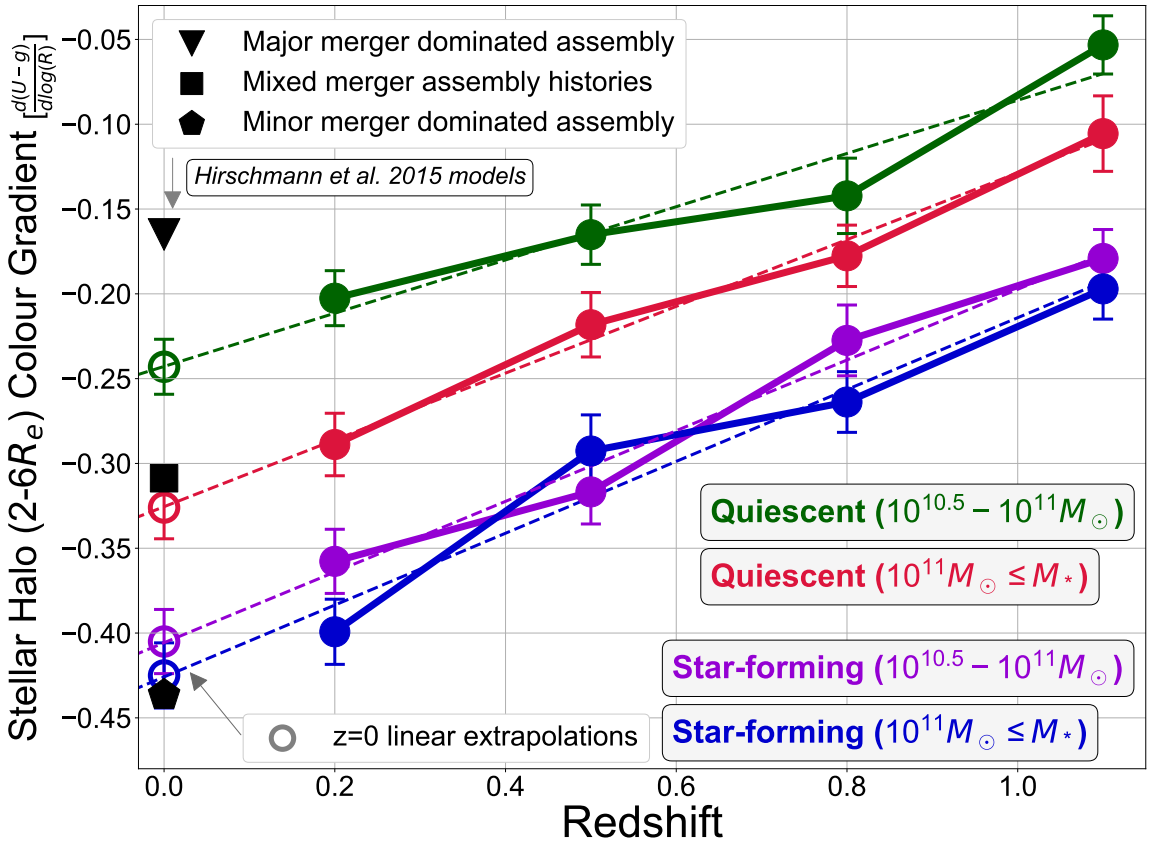

Figure 5.5. Median rest-frame U-g colour profile gradients as a function of redshift for our massive ($M_\star \geq 10^{10.5} M_\odot$) galaxy sample. Gradients are measured within a modified stellar halo region (2-6R_e) to compare with results of Hirschmann et al. (2015). Different black symbols correspond to different merger-dominated assembly histories from Hirschmann et al. (2015) models. Dashed lines show linear fits to data points, used to extrapolate the $z = 0$ gradient values shown as coloured rings.

Hirschmann et al. 2015), this means that since $z = 1.1$ massive quiescent galaxies may have experienced ∼1-2 major mergers and a larger range of minor mergers (∼1-10).

The larger amount of minor mergers that are possible could explain why the most massive ($M_\star \geq 10^{11} M_\odot$) quiescent galaxies in Fig. 5.5 (red open circle) exhibit steeper (more negative) colour gradients by $z = 0$ than the slightly less massive ($10^{10.5} M_\odot \leq M_\star < 10^{11} M_\odot$) quiescent galaxies (green open circle). A scenario that emerges from this is that both sub-populations of massive quiescent galaxies are experiencing similar

numbers of major mergers since $z = 1.1$ (causing flatter colour gradients), but the most massive quiescent galaxies ($M_\star \geq 10^{11} M_\odot$) are potentially experiencing more minor mergers overall (inducing slightly more negative colour gradients).

This comparison with the results and models of Hirschmann et al. (2015) has provided some interesting insights into the assembly histories of galaxies in our sample based on the evolution of their colours. It is important again to mention that galaxy colours are influenced by a myriad of factors, some of which (e.g. stellar metallicities and ages) are beyond the scope of this project. If we assume that ex-situ assembly is driving colour evolution in the outer regions (2-6R_e) of galaxies in our sample, then our results argue for assembly histories driven primarily by minor and very minor mergers for massive ($M_\star \geq 10^{10.5} M_\odot$) star-forming galaxies. For the massive quiescent galaxies, results suggest that a combination of major and minor mergers are driving the evolution in colour gradients since $z \sim 1.1$.

5.4 Ex-Situ Driven Stellar Mass Assembly in the Most Massive Quiescent Galaxies

In this section, we analyze the stellar mass assembly of the massive quiescent galaxies in our sample ($M_\star \geq 10^{11} M_\odot$), to investigate the role of minor and major mergers in building up this population. We omit the massive star-forming galaxies in this section simply because we lack accurate information on the precise amount of growth that has occurred through star formation over $0.2 \leq z \leq 1.1$, and thus results concerning ex-situ assembly are less certain.

In Sec. 5.4.1 we adopt the normalization procedure of van Dokkum et al. (2010) and apply it to our median rest-frame g-band light profiles. This enables us to quantify the amount of stellar mass the massive quiescent galaxies in our sample have accreted over $0.2 \leq z \leq 1.1$ based on our median profile evolution. Using this amount for total stellar mass accreted, in Sec. 5.4.2 we use observed merger stellar mass-accretion rates derived by Conselice et al. (2022) to investigate whether minor or major mergers can account for the stellar mass assembly since $z \sim 1.1$.

5.4.1 Normalized Stellar Mass Assembly

In van Dokkum et al. (2010), the authors derive an equation (their Eq. 1) that quantifies how stellar mass is built up over redshift in this massive ($M_{\star} \geq 10^{11} M_{\odot}$) galaxy population. Using their Eq. 1, the authors find a normalized stellar mass value (M_n) for each of their redshift ranges. The authors then normalize the median surface mass density profiles of their different redshift bins (their Eq. 2) so that their integral is equal to the corresponding value of M_n for that redshift bin. After performing this normalization, van Dokkum et al. (2010) demonstrate that the massive galaxy population in their sample has a significant amount of stellar mass assembly that occurs between $z = 2$ and $z = 0$ ($\sim$50%).

In this section, we adopt this normalization procedure and apply it to our median rest-frame g-band surface brightness profiles, in order to quantify how much stellar mass assembly has occurred in our massive quiescent sample based on their median profile evolution. First, we use stellar mass-to-light ratios (rest-frame g-band) to convert our median surface brightness profiles (units of $L_{\odot}/\mathrm{kpc}^2$) into median surface

mass density profiles (units of $M_{\odot}/\mathrm{kpc}^2$). For these ratios, we utilize the mean $U-g$ colour from our median rest-frame $U-g$ colour profiles (Fig. 4.11), and the relation between $U-g$ colour and $M_{\star}/L_g$ ratio from Szomoru et al. (2013, Fig. 1). This process results in a different $M_{\star}/L_g$ ratio for each of the four redshift bins of our massive quiescent sample ($M_{\star}/L_g = 1.26$, 1.41, 1.62, 1.91 for the high to low redshift bins, respectively).

Next, we use Eq. 1 from van Dokkum et al. (2010) to find a normalized stellar mass value (M_n) for each of our four redshift bins. We modify the intercept of their Eq. 1 slightly (which represents the median stellar mass of their galaxy sample) to better reflect the galaxies in our sample (median $M_{\star} = 10^{11.27} M_{\odot}$). We calculate M_n following

$$\log(M_n) = 11.27 - 0.15z, \tag{5.3}$$

where the 11.27 value is our median stellar mass for this massive quiescent galaxy bin and the $0.15z$ factor holds the important scaling information of how stellar mass changes with redshift. It should be noted that this stellar mass growth scaling factor was determined by van Dokkum et al. (2010) using massive ($M_{\star} \geq 10^{11} M_{\odot}$) star-forming and quiescent galaxies, and so it is possible that it should differ when considering only the quiescent population as we do here. However, the authors do note that Eq. 1 traces stellar mass growth regardless of whether it came through star formation or merger-related growth. Additionally, in their Fig. 3 they mention that their sample includes mostly red galaxies out to $z \sim 1$.

Next, we perform the same integration as van Dokkum et al. (2010, their Eq. 2), requiring the total enclosed stellar mass in our median surface mass density profiles

to be equal to the normalized stellar mass value (M_n) for that redshift bin. This integration is done following

$$M_n = \int_0^{R_{lim}} \Sigma(r) 2\pi r \, dr, \tag{5.4}$$

where Σ represents our median surface mass density values, and R_{lim} are the profile truncation radii (see Sec. 3.2.2). The $2\pi r dr$ factor represents the surface area element.

Figure 5.6 shows the results of the entire conversion and normalization process, and demonstrates how the median normalized surface mass density profiles of massive ($M_\star \geq 10^{11} M_\odot$) quiescent galaxies in our sample evolve over our full redshift range. The inset panel in Fig. 5.6 shows the integrated profiles (i.e. curves of growth, via Eq. 5.4), and highlights how much stellar mass assembly occurs over the full redshift range (shown as percentages of the stellar mass at $z = 0.2 - 0.35$).

We find that massive ($M_\star \geq 10^{11} M_\odot$) quiescent galaxies in our sample build up a large amount of stellar mass over the full redshift range (e.g., need to accrete an additional $\sim 4.3 \times 10^{10} M_\odot \pm 0.3 \times 10^{10} M_\odot$). The majority of this buildup occurs at extended radial distances (e.g. $R \gtrsim$10-15 kpc in Fig. 5.6). Our results are in agreement with those from van Dokkum et al. (2010), although galaxies in their sample exhibit slightly more stellar mass assembly over a similar redshift range and the outer profile regions are slightly flatter in their median profiles (i.e. more extended material detected). Although as mentioned above, these authors include massive star-forming galaxies in their analysis, so this excess growth may simply be due to star formation.

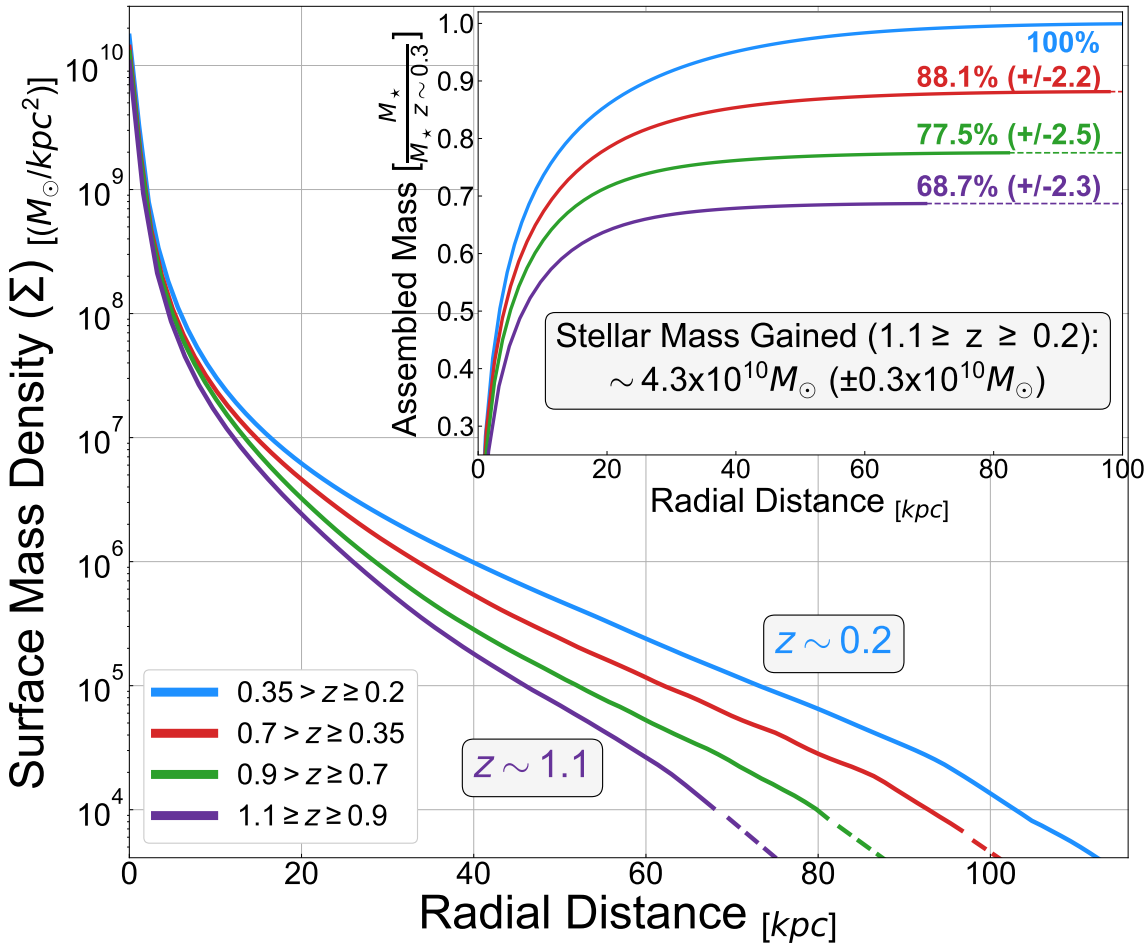

Figure 5.6. Normalized median surface mass density profiles of our massive ($M_\star \geq 10^{11} M_\odot$) quiescent galaxy sample. Profiles from different redshift ranges are colour coded and listed in the legend. The inset panel shows the curves of growth integrated via Eq. 5.4, and the percent of the $z = 0.2-0.35$ stellar mass (median $M_\star \sim 10^{11.27} M_\odot$) that has been built up at each redshift interval. The dashed portions of the higher redshift profiles (and lines in the inset panel) are extrapolations of the data. This is due to higher redshift profiles having smaller truncation radii (R_{lim}, Sec. 3.2.2).

5.4.2 Mass Growth Through Different Merger Channels

From the previous section (Sec. 5.4.1) we obtain an estimate for the amount of stellar mass ($\sim 4.3 \times 10^{10} M_\odot$) that massive quiescent galaxies in our sample need to accrete over $0.2 \leq z \leq 1.1$. In this sub-section, we investigate how different types of mergers (Sec. 1.1.2) can explain this stellar mass assembly (since star formation is ruled out

due to galaxies being quenched).

In a recent study, Conselice et al. (2022) use a combination of photometric and spectroscopic datasets to derive merger-related stellar mass-accretion rates. Figure 9 from Conselice et al. (2022) shows the stellar mass-accretion rates due to major and minor mergers for the massive ($M_\star \geq 10^{11} M_\odot$) galaxy population since $z = 3$. We retrieve these accretion rates (from their Eq. 43 and 45) and show them in Fig. 5.7, illustrating that since $z = 1.1$, more stellar mass is accreted through major mergers (blue line) than from minor mergers (purple line).

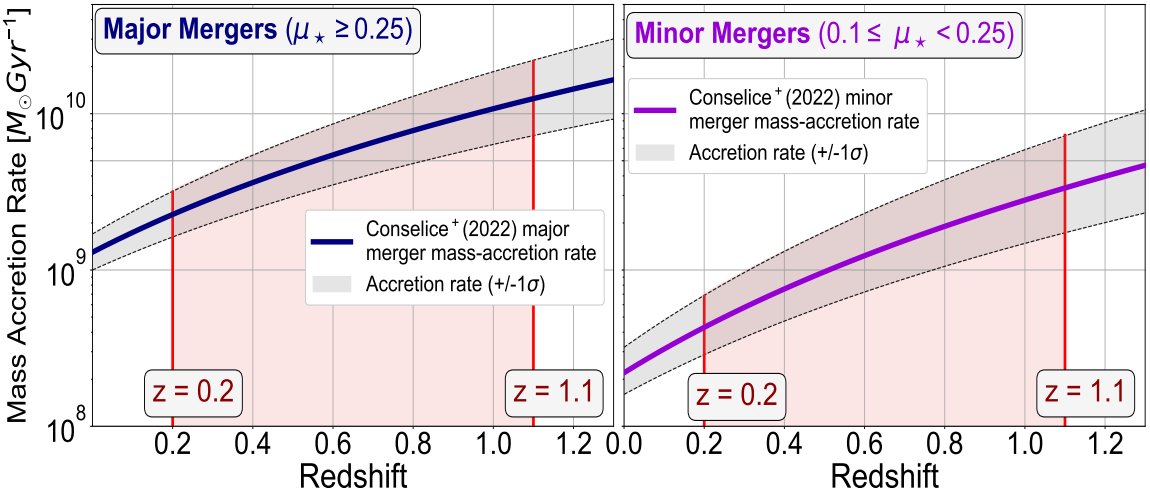

Figure 5.7. Stellar mass accretion rates from Conselice et al. (2022) for the major (blue, left-hand plot) and minor (purple, right-hand plot) merger ex-situ channels. The red region encloses our full redshift range. The grey shaded regions represent $\pm 1\sigma$ on the accretion rates.

We then integrate these curves over our specific redshift range (red regions in Fig. 5.7), to calculate the total amount of stellar mass (in $M_\odot$) that could be accreted through each merger channel. Table 5.3 summarizes the results of the integration for both types of mergers, using the average and $\pm 1\sigma$ accretion rates (dashed black lines above and below coloured lines in both panels of Fig. 5.7). In the last column of Table 5.3 we show the amount of observed stellar mass growth from the median surface mass

density profiles in Fig. 5.6 (i.e. $\sim 4.3\times10^{10} M_{\odot}$) divided by the amount expected to be accreted through each merger type and accretion rate.

Merger Channel	$M_{\star}$ **Accreted** (M_{acc}) **over 0.2** $\leq z \leq$ **1.1** $[10^{10} M_{\odot}]$	**Needed for SMD Evolution** $[4.3 \times 10^{10} M_{\odot}/M_{acc}]$
Minor mergers	$0.77^{+0.75}_{-0.34}$	$5.58^{+4.42}_{-2.75}$
Major mergers	$3.21^{+2.04}_{-1.21}$	$1.34^{+0.81}_{-0.52}$

Table 5.3: Amount of stellar mass accreted from minor and major mergers using the mass-accretion rates of Conselice et al. (2022). The first column shows the type of merger and the second column shows the specific amounts of stellar mass accreted between $z = 1.1 - 0.2$, using the average and $\pm1\sigma$ accretion rates. The final column shows the amount of observed stellar mass growth from the surface mass density (SMD) profiles in Fig. 5.6 divided by the amount expected to be accreted through each merger type and accretion rate.

To account for the entire stellar mass growth observed in the median surface mass density profiles (Fig. 5.6), massive quiescent galaxies in our sample need to accrete $5.58^{+4.42}_{-2.75}$ times more material than minor mergers alone can provide. In comparison, massive quiescent galaxies would only need to accrete $1.34^{+0.81}_{-0.52}$ times the material that major mergers could contribute. If we combine the amount of stellar mass accreted based on the average accretion rates of both minor and major mergers (i.e. $3.21 + 0.77 = 4.00\times10^{10} M_{\odot}$, second column Table 5.3), we get an amount of stellar mass that agrees with the amount identified by the surface mass density profile evolution in Fig. 5.6 (i.e. $4.3\times10^{10} M_{\odot} \pm 0.3\times10^{10} M_{\odot}$)

From this analysis, we conclude that massive ($M_{\star} \geq 10^{11} M_{\odot}$) quiescent galaxies are growing through a combination of minor and major mergers since $z \sim 1.1$, rather than minor mergers alone. This conclusion further supports findings from the literature that show major mergers are occurring at $z \lesssim 1.1$ (as discussed in Sec. 1.1.2), based on both galaxy simulations (e.g., Cannarozzo et al. 2022; Boecker et al. 2023;

Sotillo-Ramos et al. 2022) and observations (e.g., McIntosh et al. 2008; Giri et al. 2023). From our results, it is clear that major mergers are driving the bulk of the stellar mass growth for this sub-population (e.g., expected accretion of $3.21\times10^{10}M_{\odot}$ vs. $0.77\times10^{10}M_{\odot}$ from minor mergers (factor of $\sim$4), Table 5.3). These major mergers can also explain the steeper evolution in median size we measured for our massive quiescent sample (i.e. Fig. 5.4), and are likely driving the size growth of these massive quiescent galaxies along with the stellar mass assembly.

Chapter 6

Conclusions and Future Directions

We investigate the size growth and stellar mass assembly of star-forming and quiescent galaxies ($M_\star \geq 10^{9.5} M_\odot$) over a wide range of redshift ($0.2 \leq z \leq 1.1$), through the buildup of their stellar halo components. We use deep multi-wavelength photometric observations of galaxies ($U + grizy$ filters, Fig. 2.1), provided by two complementary large-area imaging surveys - HSC-SSP (Aihara et al. 2022) and CLAUDS (Sawicki et al. 2019). From the images of galaxies in our sample, we extract rest-frame g-band surface brightness profiles and rest-frame U-g colour profiles. Using these profiles and their evolution with redshift, we study how the stellar haloes of galaxies in our sample have evolved in size, colour, and stellar mass. While our results agree with the widely accepted theory of stellar haloes being built up around galaxies gradually over time as they accrete or form additional stellar material (e.g., Oser et al. 2010; Cook et al. 2010, 2016; Cooper et al. 2010; Pillepich et al. 2014; Hirschmann et al. 2015; Huško et al. 2022; Genina et al. 2023), we also show that this growth and evolution is not uniform across all galaxy populations.

The key conclusions from our results, concerning the stellar halo assemblies of galaxies in our sample are as follows:

1. **More massive galaxies build up brighter and more extended stellar haloes since $z \sim 1.1$ than less massive galaxies**. This is evident from the buildup of their rest-frame g-band surface brightness profiles over the full redshift range (Fig. 4.3-SF, and Fig. 4.4-Q), where the amount of relative growth scales with increasing stellar mass. The profile buildup is particularly noticeable in the outer stellar halo regions ($R \geq 4R_e$, Fig. 4.14), where we see more massive galaxies assemble stellar halo material at larger physical radial distances than less massive galaxies. From the measured increases to the integrated stellar halo light (i.e. L_{halo}), we find that over $0.2 \leq z \leq 1.1$ quiescent galaxies in our four stellar mass bins (Table 3.1) increase L_{halo} by a factor 1.31, 1.58, 2.12, and 2.38. In comparison, the star-forming galaxies increase L_{halo} by a factor 1.43, 1.79, 2.24, and 2.31 over the full redshift range.

2. **Stellar mass assembly in inner galaxy regions (1-4R_e) occurs very differently for low-mass galaxies ($10^{9.5} M_\odot \leq M_\star < 10^{10.5} M_\odot$) and high-mass galaxies ($M_\star \geq 10^{10.5} M_\odot$).** We find that high-mass galaxies in our sample (particularly quiescent galaxies) show a greater degree of buildup in the inner regions (1-4R_e) of their rest-frame g-band surface brightness profiles (Fig. 4.1-SF, and Fig. 4.2-Q). From analyzing light profile gradients in these central (1-2R_e, Fig. 4.6) and intermediate (2-4R_e, Fig. 4.8) galaxy regions, we see the low-mass galaxies exhibit trends towards slightly steeper light profile gradients at low redshift. High-mass galaxies instead display the opposite trend

towards flatter gradients by $z \sim 0.2$. Based on predictions from simulations, these two trends imply that stellar mass buildup in inner galaxy regions is primarily influenced by internal physical processes for low-mass galaxies (e.g. star formation, AGN or stellar feedback), and by ex-situ accretion for high-mass galaxies (Cook et al. 2016).

3. **Stellar haloes of galaxies display negative U-g colour gradients (i.e. bluer outskirts, redder inner regions), which are steeper at higher stellar masses or with decreasing redshift (at fixed stellar mass).** This is evident from the median rest-frame U-g colour profiles (Fig. 4.11) and the colour gradients measured within smaller radial regions (Fig. 4.12). All median rest-frame U-g colour profiles slope downward towards bluer outskirts, and higher stellar masses show the steepest colour profiles. The evolution towards more negative U-g colour gradients at lower redshift is more noticeable at larger distances, seen more clearly in the evolution of colour gradients in extended regions (i.e. 4-6R_e and 6-8R_e). The presence of negative colour gradients in our quiescent sample is particularly interesting given that star formation cannot account for the bluer colours in the outskirts of these galaxies.

4. **More massive galaxies exhibit larger size (R_e) growth since $z \sim 1.1$ than less massive galaxies. At a fixed stellar mass, quiescent galaxies exhibit greater size growth than star-forming galaxies.** From the size-stellar mass relations of galaxies in our sample (Fig. 5.3), we find that the slope of the relation for quiescent galaxies is always steeper than that for star-forming galaxies within a redshift interval. When we split the sample at a pivot mass of $M_p = 10^{10.5} M_\odot$, we find that the high-mass galaxies exhibit steeper

slopes in the size-stellar mass relations (particularly for quiescent galaxies). The slopes of the relations for the lower two stellar mass bins are γ ∼0.25-0.37 (quiescent galaxies) and γ ∼0.15-0.22 (star-forming galaxies) depending on the redshift interval. In comparison, the two higher stellar mass bins display slopes of β ∼0.52-0.6 (quiescent galaxies) and β ∼0.22-0.40 (star-forming galaxies) depending on the redshift interval. Furthermore, more massive galaxies (or quiescent galaxies at a fixed stellar mass) show a faster evolution in median size over $0.2 \leq z \leq 1.1$ than less massive galaxies (or star-forming galaxies at fixed stellar mass, Fig. 5.4). The exponent (α) of the best-fit median size growth trend ($R_e \propto A(1+z)^{-\alpha}$) ranges from $\alpha = 0.19$ to $\alpha = 0.81$ for star-forming galaxies and from $\alpha = 0.51$ to $\alpha = 0.99$ for quiescent galaxies (for low to high stellar mass bins).

One of our main objectives in this work is to study merger-related growth in galaxies and how stellar halo assembly is influenced by ex-situ accretion. Additionally, we aim to separate contributions from minor and major mergers to galaxy assembly at these redshifts ($0.2 \leq z \leq 1.1$). To accomplish this, we probe various processes and effects contributing to the stellar halo growth of galaxies in our sample and investigate fractional contributions from ex-situ accretion. We also explore the role of the pivot mass range ($M_p \sim 10^{10.5\pm0.5} M_\odot$) and how it may mark a transition into an ex-situ dominated phase of assembly in galaxies, as suggested in the literature both observationally (e.g., Mowla et al. 2019a; Kawinwanichakij et al. 2021) and from simulations (e.g., Tacchella et al. 2019; Huško et al. 2022). Lastly, we investigate the role of minor and major mergers in driving the evolution in sizes, stellar masses, and colours of galaxies in our sample, to provide insight into which ex-situ channels are

dominating galaxy assembly over $0.2 \leq z \leq 1.1$.

From our investigation of ex-situ driven galaxy assembly, we find:

5. **Quiescent galaxies accrete more stellar mass through ex-situ channels than star-forming galaxies of similar stellar masses.** In Fig. 5.1 we estimated the contributions to total stellar halo growth over $0.2 \leq z \leq 1.1$ from in-situ star formation for star-forming galaxies (∼100%, ∼100%, ∼70%, and ∼36%, low to high stellar mass bins) and the effect of progenitor bias for quiescent galaxies (∼87%, ∼55%, ∼20%, and ∼10%, low to high stellar mass bins). After accounting for these contributions and effects, we find that quiescent galaxies contain larger additional fractions of assembled stellar mass in their stellar haloes than star-forming galaxies at similar masses. After comparing with predictions from simulations in Fig. 5.2, we show these remaining fractions of assembled material are most likely ex-situ fractions. The stellar halo ex-situ fractions we estimate for our quiescent sample are ∼13%, ∼45%, ∼80%, and ∼90% (low to high stellar mass bins), while star-forming galaxies contain stellar halo ex-situ fractions of ∼ 0%, ∼ 0%, ∼30%, and ∼64%. Apart from ex-situ fractions, we find that quiescent galaxies exhibit steeper slopes of their size-stellar mass relations (Fig. 5.3) and a steeper evolution in median size with redshift than star-forming galaxies at similar masses (Fig. 5.4). This enhanced size growth has been linked to a larger influence from ex-situ assembly. Finally, we find that the rest-frame U-g colour gradients of massive ($M_\star \geq 10^{10.5} M_\odot$) quiescent galaxies agree with predictions of galaxy assembly driven by a mixture of major and minor mergers (Fig. 5.5). The colour gradients of star-forming

galaxies instead aligned with models with minor merger-dominated assembly histories.

6. **Galaxies near or above a pivot mass range ($M_p \sim 10^{10.5\pm0.5} M_\odot$) show evidence of a larger contribution from ex-situ accretion to their assembly.** We infer this through several of our results. First, we see a stark contrast in the evolution of median surface brightness profile gradients in the central (Fig. 4.6) and intermediate (Fig. 4.8) galaxy regions between high-mass ($M_\star \geq 10^{10.5} M_\odot$) and low-mass galaxies ($10^{9.5} M_\odot \leq M_\star < 10^{10.5} M_\odot$). The high-mass galaxies display a flattening trend (predicted to be from ex-situ accretion; Hopkins et al. 2010; Cook et al. 2016), while low-mass galaxies show a steepening trend (predicted to be from lack of mergers; Cook et al. 2016). With our estimated stellar halo ex-situ fractions in Fig. 5.1 we also see a contrast above and below the pivot mass. We calculate no ex-situ fractions for the low-mass star-forming galaxies, while for high-mass star-forming we estimate ∼30% and ∼64% of their stellar halo material is accreted through mergers. In comparison, the estimated ex-situ fractions for low-mass quiescent galaxies are ∼13% and ∼45% while high-mass quiescent galaxies contain much higher fractions of accreted material in their stellar haloes (∼80% and ∼90%). Lastly, when we use the pivot mass to fit two separate size-stellar mass relations for the low- and high-mass galaxies (Fig. 5.3), we find that galaxies above the pivot mass display significantly steeper slopes to their relations (and steeper evolution in median sizes, Table 5.2). This enhanced size growth has been suggested to be a result of merger activity and ex-situ accretion (e.g., Mowla et al. 2019a; Kawinwanichakij et al. 2021; Damjanov et al. 2022a).

7. **Minor and very minor mergers are likely dominating the ex-situ assembly of most galaxies in our sample. However, major mergers appear to play a significant role in building up the massive ($M_\star \geq 10^{10.5} M_\odot$) quiescent population since $z \sim 1.1$.** Many of our results are in favour of a minor merger-driven scenario (since $z \sim 1.1$) for all star-forming galaxies and low-mass ($10^{9.5} M_\odot \leq M_\star < 10^{10.5} M_\odot$) quiescent galaxies in our sample. This includes the negative $U - g$ colour gradients (Fig. 4.12 and Fig. 5.5), which are predicted to arise from minor mergers (Hirschmann et al. 2015). From the lack of substantial light profile buildup (and gradient flattening) in the inner regions (i.e. 1-4R_e, see gradients in Fig. 4.6 and Fig. 4.8) we can infer that major mergers are not the dominating ex-situ channel as they are predicted to significantly grow these inner profile regions (Hopkins et al. 2010; Hilz et al. 2013). The ex-situ fractions we estimate (Fig. 5.1) for the star-forming galaxies and low-mass quiescent galaxies can arise from minor mergers alone based on simulations (e.g., Rodriguez-Gomez et al. 2016; Huško et al. 2022). Lastly, the evolution in median sizes (Fig. 5.4) we measure for these sub-populations is not enough to require any major mergers based on predictions (e.g., Hopkins et al. 2010).

However, for massive quiescent galaxies ($M_\star \geq 10^{10.5} M_\odot$) our results suggest major mergers are playing an equally significant role in driving assembly. We see they display a substantial amount of central (1-2R_e) light profile flattening (Fig. 4.6), predicted to arise more from major mergers than minor interactions (Hopkins et al. 2010; Hilz et al. 2013). We also find that low redshift U-g colour gradients of massive quiescent galaxies align with simulated galaxy mod-

els where 1-2 major mergers (and 1-10 minor mergers) occurred since $z = 1.1$ (Fig. 5.5). Additionally, the estimated ex-situ fractions for massive quiescent galaxies (∼80-90%, Fig. 5.1) are too high to arise from minor mergers alone based on simulations (e.g., Rodriguez-Gomez et al. 2016; Tacchella et al. 2019). Lastly, from our analysis of the stellar mass assembly of the most massive quiescent galaxies ($M_\star \geq 10^{11} M_\odot$) over $0.2 \leq z \leq 1.1$, in order to account for the buildup in their median surface mass density profiles (Fig. 5.6), these massive quiescent galaxies would have to accrete $5.58^{+4.42}_{-2.75}$ times more material than minor mergers alone can provide (see Table 5.3). In comparison, massive quiescent galaxies only need to accrete $1.34^{+0.81}_{-0.52}$ times the amount expected from major mergers, and combining the expected amount of accretion through both minor and major mergers agrees very well with the evolution in the median surface mass density profiles over $0.2 \leq z \leq 1.1$.

In summary, we have investigated the size growth and stellar mass assembly in half a million galaxies we observe at $0.2 \leq z \leq 1.1$, and analyzed their evolution in size, stellar mass, and colour through the assembly of their stellar halo components. We find that more massive galaxies are building up brighter and more extended stellar haloes since $z \sim 1.1$ than less massive galaxies. The processes driving this assembly are inducing negative colour gradients (rest-frame U-g) in galaxy outskirts (even in quiescent galaxies), which grow steeper (more negative) with decreasing redshift. More massive galaxies (particularly in the quiescent population) also exhibit significantly more growth in their inner galaxy regions (i.e. 1-4R_e) than less massive galaxies. This inner buildup is driving a much faster evolution in median size (R_e) over $0.2 \leq z \leq 1.1$ and steeper slopes in their size-stellar mass relations. From

estimating stellar halo ex-situ fractions, we find quiescent galaxies are growing much more through ex-situ assembly than star-forming galaxies at a fixed stellar mass. Furthermore, we note several instances where galaxies above or below a pivot mass of $M_p = 10^{10.5} M_\odot$ display evidence of very different contributions from ex-situ accretion. This may indicate that this stellar mass range (i.e. $M_\star \sim 10^{10.5\pm0.5} M_\odot$) marks the transition from an in-situ to an ex-situ-dominated phase of assembly for galaxies. Combined together, our results imply that minor and very minor mergers are likely driving the size evolution of the majority of galaxies in our sample over $0.2 \leq z \leq 1.1$. These minor interactions can also account for any ex-situ-related stellar mass assembly in star-forming galaxies or low-mass quiescent galaxies ($10^{9.5} M_\odot \leq M_\star < 10^{10.5} M_\odot$). For the massive quiescent galaxy population ($M_\star \geq 10^{10.5} M_\odot$), our results instead suggest that major mergers are also playing an important role in the assembly of this population since $z \sim 1.1$. Major mergers are dominating the stellar mass assembly in these massive quiescent galaxies and are greatly accelerating their size growth in addition to the contribution from minor mergers.

6.1 Future Directions

One important aspect of galaxy evolution that we have not addressed in this work is the influence of the cosmic environment. The location of a galaxy in the large-scale cosmic web structure (i.e. in a dense cluster or under-dense void region) can have a significant impact on its evolution and the physical processes that regulate its size growth and stellar mass assembly (Kotecha et al. 2021; Wechsler & Tinker 2018; Conselice 2014).

The additional analysis of the evolution of galaxy light profiles with respect to galaxy environment will enable us to probe the results of this work further. First and foremost we will be able to better understand how galaxy-galaxy interactions and ex-situ accretion are influencing galaxy assembly. For example, we can better understand the influence of major or minor mergers if we have a more accurate picture of how galaxies are physically distributed in different environments. Furthermore, as demonstrated in the simulations by Kotecha et al. (2021), the level of quenching experienced by galaxies can significantly differ depending on their location in the cosmic web. In particular, the filament regions appear to be important sites where the pre-processing of material in galaxies is occurring, as galaxies travel along filaments toward denser cluster regions. It is thus important to understand how filament regions are regulating in-situ stellar mass assembly, and also whether these filament regions are sites that promote galaxy-galaxy interactions and the accretion of ex-situ material.

In the near future, we plan to investigate the effect of the cosmic environment on galaxy size growth and stellar mass assembly. This will be accomplished through the results of the DEUS survey, an upcoming deep U-band imaging survey conducted by CFHT in the northern Euclid deep field. Based on these observations and with the help of ancillary data, we will trace the cosmic web structure out to a redshift of $z \sim 2$, to study how the evolution of galaxy stellar haloes is impacted by their location in the cosmic web.

Appendix A

Median Rest-Frame g-Band Surface Brightness Profile Gradients

Stellar Mass & Redshift Bin	**1-2**R_e $[mag/dex]$	**2-4**R_e $[mag/dex]$	**4-10**R_e $[mag/dex]$
0.2≤ z <0.35			
9.5≤ $M_\star$ <10	-5.27 ±0.17	-3.64 ±0.14	-1.22 ±0.05
10≤ $M_\star$ <10.5	-4.23 ±0.17	-2.93 ±0.14	-0.92 ±0.05
10.5≤ $M_\star$ <11	-2.42 ±0.17	-2.26 ±0.14	-0.55 ±0.05
11≤ $M_\star$	-1.70 ±0.17	-1.81 ±0.15	-0.35 ±0.05
0.35≤ z <0.7			
9.5≤ $M_\star$ <10	-4.76 ±0.17	-3.52 ±0.16	-1.36 ±0.06
10≤ $M_\star$ <10.5	-4.09 ±0.17	-3.13 ±0.16	-0.98 ±0.06
10.5≤ $M_\star$ <11	-3.11 ±0.17	-2.62 ±0.17	-0.62 ±0.06
11≤ $M_\star$	-2.02 ±0.18	-2.26 ±0.17	-0.41 ±0.05
0.7≤ z <0.9			
9.5≤ $M_\star$ <10	-4.38 ±0.19	-3.48 ±0.15	-1.40 ±0.07
10≤ $M_\star$ <10.5	-3.83 ±0.19	-3.32 ±0.15	-1.09 ±0.07
10.5≤ $M_\star$ <11	-3.45 ±0.19	-3.05 ±0.16	-0.66 ±0.06
11≤ $M_\star$	-2.93 ±0.19	-2.64 ±0.16	-0.44 ±0.06
0.9≤ z <1.1			
9.5≤ $M_\star$ <10	-4.33 ±0.19	-3.44 ±0.14	-1.45 ±0.08
10≤ $M_\star$ <10.5	-4.11 ±0.19	-3.57 ±0.14	-1.14 ±0.08
10.5≤ $M_\star$ <11	-3.99 ±0.19	-3.29 ±0.14	-0.74 ±0.07
11≤ $M_\star$	-3.56 ±0.2	-2.95 ±0.15	-0.49 ±0.07

Table A.1: Summary of all profile gradients (see Sec. 4.2 and plots contained within) measured from the median rest-frame g-band surface brightness profiles of our ***quiescent*** galaxy sample (Fig. 4.2). Errors on gradient values are derived from the median profile percentiles (16/84%), discussed in Sec. 3.2.2. Specific radial regions are defined and discussed in Sec. 3.2.5. Stellar mass ranges are displayed in units of $\log[M_\star/M_\odot]$.

Stellar Mass & Redshift Bin	**1-2**R_e $[mag/dex]$	**2-4**R_e $[mag/dex]$	**4-10**R_e $[mag/dex]$
0.2≤ z <0.35			
9.5≤ $M_\star$ <10	-3.61 ±0.14	-3.86 ±0.14	-0.51 ±0.05
10≤ $M_\star$ <10.5	-3.17 ±0.14	-3.24 ±0.14	-0.48 ±0.04
10.5≤ $M_\star$ <11	-2.33 ±0.15	-2.88 ±0.14	-0.38 ±0.04
11≤ $M_\star$	-1.77 ±0.15	-2.38 ±0.15	-0.29 ±0.03
0.35≤ z <0.7			
9.5≤ $M_\star$ <10	-3.33 ±0.16	-3.59 ±0.16	-0.44 ±0.05
10≤ $M_\star$ <10.5	-3.11 ±0.17	-3.35 ±0.16	-0.40 ±0.04
10.5≤ $M_\star$ <11	-2.69 ±0.18	-3.09 ±0.17	-0.35 ±0.04
11≤ $M_\star$ -	2.22 ±0.17	-2.82 ±0.17	-0.26 ±0.04
0.7≤ z <0.9			
9.5≤ $M_\star$ <10	-3.26 ±0.19	-3.50 ±0.15	-0.42 ±0.05
10≤ $M_\star$ <10.5	-3.05 ±0.18	-3.45 ±0.15	-0.39 ±0.04
10.5≤ $M_\star$ <11	-2.87 ±0.19	-3.19 ±0.16	-0.32 ±0.04
11≤ $M_\star$	-2.50 ±0.19	-3.03 ±0.16	-0.25 ±0.04
0.9≤ z <1.1			
9.5≤ $M_\star$ <10	-3.13 ±0.19	-3.47 ±0.14	-0.40 ±0.04
10≤ $M_\star$ <10.5	-3.02 ±0.19	-3.49 ±0.14	-0.36 ±0.04
10.5≤ $M_\star$ <11	-3.09 ±0.2	-3.41 ±0.14	-0.31 ±0.04
11≤ $M_\star$	-2.81 ±0.2	-3.18 ±0.15	-0.24 ±0.04

Table A.2: Summary of all profile gradients (see Sec. 4.2 and plots contained within) measured from the median rest-frame g-band surface brightness profiles of our ***star-forming*** galaxy sample (Fig. 4.1). Errors on gradient values are derived from the median profile percentiles (16/84%), discussed in Sec. 3.2.2. Specific radial regions are defined and discussed in Sec. 3.2.5. Stellar mass ranges are displayed in units of $\log[M_\star/M_\odot]$.

Appendix B

Median Rest-Frame U-g Colour Profile Gradients

Stellar Mass & Redshift Bin	∇U-g $[mag/dex]$	∇U-g $[mag/dex]$	∇U-g $[mag/dex]$	∇U-g $[mag/dex]$
0.2≤ z <0.35	**1-2 R_e**	**2-4 R_e**	**4-6 R_e**	**6-8 R_e**
9.5≤ $M_\star$ <10	-0.018±0.02	-0.026±0.03	-0.297±0.04	-0.186±0.04
10≤ $M_\star$ <10.5	-0.032±0.02	-0.127±0.04	-0.447±0.04	-0.322±0.05
10.5≤ $M_\star$ <11	-0.031±0.03	-0.212±0.04	-0.596±0.05	-0.437±0.05
11≤ $M_\star$	0.004±0.03	-0.192±0.03	-0.740±0.05	-0.574±0.05
0.35≤ z <0.7	**1-2 R_e**	**2-4 R_e**	**4-6 R_e**	**6-8 R_e**
9.5≤ $M_\star$ <10	-0.013±0.02	-0.059±0.04	-0.181±0.04	-0.198±0.04
10≤ $M_\star$ <10.5	-0.061±0.03	-0.058±0.04	-0.322±0.04	-0.138±0.05
10.5≤ $M_\star$ <11	-0.028±0.02	-0.211±0.03	-0.578±0.04	-0.404±0.05
11≤ $M_\star$	-0.022±0.03	-0.126±0.03	-0.507±0.05	-0.593±0.05
0.7≤ z <0.9	**1-2 R_e**	**2-4 R_e**	**4-6 R_e**	**6-8 R_e**
9.5≤ $M_\star$ <10	-0.005±0.02	-0.104±0.04	-0.079±0.05	-0.061±0.04
10≤ $M_\star$ <10.5	-0.095±0.03	-0.063±0.05	-0.275±0.05	-0.223±0.06
10.5≤ $M_\star$ <11	0.024±0.03	-0.121±0.04	-0.361±0.05	-0.276±0.06
11≤ $M_\star$	-0.035±0.03	-0.190±0.04	-0.401±0.06	-0.104±0.05
0.9≤ z ≤1.1	**1-2 R_e**	**2-4 R_e**	**4-6 R_e**	**6-8 R_e**
9.5≤ $M_\star$ <10	0.015±0.02	-0.051±0.03	-0.081±0.05	-0.089±0.04
10≤ $M_\star$ <10.5	-0.059±0.03	0.038±0.04	-0.236±0.05	-0.151±0.05
10.5≤ $M_\star$ <11	0.002±0.02	-0.048±0.03	-0.280±0.06	-0.188±0.05
11≤ $M_\star$	0.033±0.03	-0.116±0.05	-0.423±0.06	-0.192±0.05

Table B.1: Median rest-frame U-g colour profile gradients of the ***star-forming*** galaxy sample. Colour gradients are plotted in Fig. 4.12, and colour profiles are shown in Fig. 4.11. Stellar mass ranges are displayed in units of $\log[M_\star/M_\odot]$.

Stellar Mass & Redshift Bin	∇U-g $[mag/dex]$	∇U-g $[mag/dex]$	∇U-g $[mag/dex]$	∇U-g $[mag/dex]$
0.2≤ z <0.35	**1-2 R_e**	**2-4 R_e**	**4-6 R_e**	**6-8 R_e**
9.5≤ $M_\star$ <10	0.050±0.03	-0.024±0.03	-0.153±0.05	-0.350±0.04
10≤ $M_\star$ <10.5	0.023±0.03	-0.057±0.03	-0.213±0.05	-0.293±0.05
10.5≤ $M_\star$ <11	-0.093±0.02	-0.104±0.02	-0.440±0.05	-0.668±0.05
11≤ $M_\star$	-0.044±0.03	-0.151±0.03	-0.669±0.05	-0.880±0.04
0.35≤ z <0.7	**1-2 R_e**	**2-4 R_e**	**4-6 R_e**	**6-8 R_e**
9.5≤ $M_\star$ <10	0.040±0.03	-0.033±0.04	-0.061±0.06	-0.220±0.04
10≤ $M_\star$ <10.5	-0.019±0.03	-0.003±0.04	-0.173±0.05	-0.312±0.06
10.5≤ $M_\star$ <11	-0.034±0.03	-0.079±0.03	-0.343±0.05	-0.395±0.05
11≤ $M_\star$	-0.035±0.03	-0.099±0.03	-0.402±0.06	-0.436±0.05
0.7≤ z <0.9	**1-2 R_e**	**2-4 R_e**	**4-6 R_e**	**6-8 R_e**
9.5≤ $M_\star$ <10	0.124±0.03	-0.007±0.03	-0.130±0.06	-0.199±0.05
10≤ $M_\star$ <10.5	-0.118±0.03	-0.016±0.03	-0.188±0.06	-0.108±0.05
10.5≤ $M_\star$ <11	0.145±0.04	-0.003±0.03	-0.384±0.06	-0.384±0.06
11≤ $M_\star$	-0.048±0.04	-0.041±0.03	-0.324±0.06	-0.486±0.05
0.9≤ z ≤1.1	**1-2 R_e**	**2-4 R_e**	**4-6 R_e**	**6-8 R_e**
9.5≤ $M_\star$ <10	0.160±0.03	-0.009±0.03	-0.021±0.06	-0.241±0.05
10≤ $M_\star$ <10.5	-0.145±0.03	-0.042±0.04	-0.064±0.06	-0.160±0.06
10.5≤ $M_\star$ <11	0.069±0.04	-0.048±0.04	-0.197±0.07	-0.335±0.06
11≤ $M_\star$	0.066±0.04	-0.007±0.03	-0.321±0.07	-0.386±0.05

Table B.2: Median rest-frame U-g colour profile gradients of the ***quiescent*** galaxy sample. Colour gradients are plotted in Fig. 4.12, and colour profiles are shown in Fig. 4.11. Stellar mass ranges are displayed in units of $\log[M_\star/M_\odot]$.

References

Abadi, M. G., Moore, B., & Bower, R. G. 1999, MNRAS, 308, 947, doi: 10.1046/j.1365-8711.1999.02715.x

Aihara, H., Arimoto, N., Armstrong, R., et al. 2018, PASJ, 70, S4, doi: 10.1093/pasj/psx066

Aihara, H., AlSayyad, Y., Ando, M., et al. 2022, PASJ, 74, 247, doi: 10.1093/pasj/psab122

Arnouts, S., & Ilbert, O. 2011, LePHARE: Photometric Analysis for Redshift Estimate, Astrophysics Source Code Library, record ascl:1108.009. http://ascl.net/1108.009

Arnouts, S., Le Floc'h, E., Chevallard, J., et al. 2013, A&A, 558, A67, doi: 10.1051/0004-6361/201321768

Astropy Collaboration, Robitaille, T. P., Tollerud, E. J., et al. 2013, A&A, 558, A33, doi: 10.1051/0004-6361/201322068

Baldry, I. K., Glazebrook, K., Brinkmann, J., et al. 2004, ApJ, 600, 681, doi: 10.1086/380092

Balogh, M. L., Baldry, I. K., Nichol, R., et al. 2004, ApJ, 615, L101, doi: 10.1086/426079

Bell, E. F., McIntosh, D. H., Katz, N., & Weinberg, M. D. 2003, ApJS, 149, 289, doi: 10.1086/378847

Bell, E. F., Naab, T., McIntosh, D. H., et al. 2006, ApJ, 640, 241, doi: 10.1086/499931

Bender, R., Doebereiner, S., & Moellenhoff, C. 1988, A&AS, 74, 385

Benson, A. J. 2010, Phys. Rep., 495, 33, doi: 10.1016/j.physrep.2010.06.001

Bergin, E. A., & Tafalla, M. 2007, ARA&A, 45, 339, doi: 10.1146/annurev.astro.45.071206.100404

Bernardi, M., Roche, N., Shankar, F., & Sheth, R. K. 2011, MNRAS, 412, L6, doi: 10.1111/j.1745-3933.2010.00982.x

Bertin, E. 2011, in Astronomical Society of the Pacific Conference Series, Vol. 442, Astronomical Data Analysis Software and Systems XX, ed. I. N. Evans, A. Accomazzi, D. J. Mink, & A. H. Rots, 435

Bertin, E., & Arnouts, S. 1996, A&AS, 117, 393, doi: 10.1051/aas:1996164

Bezanson, R., van Dokkum, P. G., Tal, T., et al. 2009, ApJ, 697, 1290, doi: 10.1088/0004-637X/697/2/1290

Bluck, A. F. L., Conselice, C. J., Buitrago, F., et al. 2012, ApJ, 747, 34, doi: 10.1088/0004-637X/747/1/34

Boecker, A., Neumayer, N., Pillepich, A., et al. 2023, MNRAS, 519, 5202, doi: 10.1093/mnras/stac3759

Borlaff, A., Eliche-Moral, M. C., Beckman, J. E., et al. 2017, A&A, 604, A119, doi: 10.1051/0004-6361/201630282

Borlaff, A., Eliche-Moral, M. C., Rodríguez-Pérez, C., et al. 2014, A&A, 570, A103, doi: 10.1051/0004-6361/201424299

Bosch, J., Armstrong, R., Bickerton, S., et al. 2018, PASJ, 70, S5, doi: 10.1093/pasj/psx080

Boselli, A., Fossati, M., & Sun, M. 2022, A&A Rev., 30, 3, doi: 10.1007/s00159-022-00140-3

Boylan-Kolchin, M., Ma, C.-P., & Quataert, E. 2005, MNRAS, 362, 184, doi: 10.1111/j.1365-2966.2005.09278.x

Brennan, R., Pandya, V., Somerville, R. S., et al. 2015, MNRAS, 451, 2933, doi: 10.1093/mnras/stv1007

Bridge, C. R., Carlberg, R. G., & Sullivan, M. 2010, ApJ, 709, 1067, doi: 10.1088/0004-637X/709/2/1067

Bruzual, G., & Charlot, S. 2003, MNRAS, 344, 1000, doi: 10.1046/j.1365-8711.2003.06897.x

Buitrago, F., Trujillo, I., Curtis-Lake, E., et al. 2017, MNRAS, 466, 4888, doi: 10.1093/mnras/stw3382

Bundy, K., Fukugita, M., Ellis, R. S., et al. 2009, ApJ, 697, 1369, doi: 10.1088/0004-637X/697/2/1369

Calzetti, D., Harris, J., Smith, D. A., et al. 2002, in American Astronomical Society Meeting Abstracts, Vol. 201, American Astronomical Society Meeting Abstracts, 116.04

Calzetti, D., Kinney, A. L., Storchi-Bergmann, T., & Panagia, N. 1993, in American Astronomical Society Meeting Abstracts, Vol. 182, American Astronomical Society Meeting Abstracts #182, 31.10

Cannarozzo, C., Leauthaud, A., Oyarzún, G. A., et al. 2022, arXiv e-prints, arXiv:2210.08109. https://arxiv.org/abs/2210.08109

Carollo, C. M., Bschorr, T. J., Renzini, A., et al. 2013, ApJ, 773, 112, doi: 10.1088/0004-637X/773/2/112

Chambers, K. C., Magnier, E. A., Metcalfe, N., et al. 2016, arXiv e-prints, arXiv:1612.05560, doi: 10.48550/arXiv.1612.05560

Chen. 2019, Master's Thesis, Department of Astronomy and Physics, Saint Mary's University. https://library2.smu.ca/handle/01/29025

Coccato, L., Gerhard, O., & Arnaboldi, M. 2010, MNRAS, 407, L26, doi: 10.1111/j.1745-3933.2010.00897.x

Conselice, C. J. 2014, ARA&A, 52, 291, doi: 10.1146/annurev-astro-081913-040037

Conselice, C. J., Mundy, C. J., Ferreira, L., & Duncan, K. 2022, ApJ, 940, 168, doi: 10.3847/1538-4357/ac9b1a

Conselice, C. J., Yang, C., & Bluck, A. F. L. 2009a, MNRAS, 394, 1956, doi: 10.1111/j.1365-2966.2009.14396.x

—. 2009b, MNRAS, 394, 1956, doi: 10.1111/j.1365-2966.2009.14396.x

Consolandi, G., Gavazzi, G., Fumagalli, M., Dotti, M., & Fossati, M. 2016, A&A, 591, A38, doi: 10.1051/0004-6361/201527618

Contini, E., Gu, Q., Ge, X., et al. 2020, ApJ, 889, 156, doi: 10.3847/1538-4357/ab6730

Cook, B. A., Conroy, C., Pillepich, A., Rodriguez-Gomez, V., & Hernquist, L. 2016, ApJ, 833, 158, doi: 10.3847/1538-4357/833/2/158

Cook, M., Barausse, E., Evoli, C., Lapi, A., & Granato, G. L. 2010, MNRAS, 402, 2113, doi: 10.1111/j.1365-2966.2009.15875.x

Cooper, A. P., Cole, S., Frenk, C. S., et al. 2010, MNRAS, 406, 744, doi: 10.1111/j.1365-2966.2010.16740.x

Daddi, E., Renzini, A., Pirzkal, N., et al. 2005, ApJ, 626, 680, doi: 10.1086/430104

Damjanov, I., Sohn, J., Geller, M. J., Utsumi, Y., & Dell'Antonio, I. 2022a, arXiv e-prints, arXiv:2210.01129. https://arxiv.org/abs/2210.01129

Damjanov, I., Sohn, J., Utsumi, Y., Geller, M. J., & Dell'Antonio, I. 2022b, ApJ, 929, 61, doi: 10.3847/1538-4357/ac54bd

Damjanov, I., Zahid, H. J., Geller, M. J., & Hwang, H. S. 2015, ApJ, 815, 104, doi: 10.1088/0004-637X/815/2/104

Damjanov, I., Zahid, H. J., Geller, M. J., et al. 2019, ApJ, 872, 91, doi: 10.3847/1538-4357/aaf97d

Damjanov, I., McCarthy, P. J., Abraham, R. G., et al. 2009, ApJ, 695, 101, doi: 10.1088/0004-637X/695/1/101

Davies, J. J., Pontzen, A., & Crain, R. A. 2022, MNRAS, 515, 1430, doi: 10.1093/mnras/stac1742

Davison, T. A., Norris, M. A., Pfeffer, J. L., Davies, J. J., & Crain, R. A. 2020, MNRAS, 497, 81, doi: 10.1093/mnras/staa1816

de Jong, R. S. 2008, MNRAS, 388, 1521, doi: 10.1111/j.1365-2966.2008.13505.x

de Jong, R. S., & Davies, R. L. 1997, MNRAS, 285, L1, doi: 10.1093/mnras/285.1.L1

Desprez, G., Picouet, V., Moutard, T., et al. 2023, A&A, 670, A82, doi: 10.1051/0004-6361/202243363

Di Matteo, P., Bournaud, F., Martig, M., et al. 2008, A&A, 492, 31, doi: 10.1051/0004-6361:200809480

Dimauro, P., Daddi, E., Shankar, F., et al. 2022, MNRAS, 513, 256, doi: 10.1093/mnras/stac884

Donnari, M., Pillepich, A., Nelson, D., et al. 2021, MNRAS, 506, 4760, doi: 10.1093/mnras/stab1950

—. 2019, MNRAS, 485, 4817, doi: 10.1093/mnras/stz712

Driver, S. P., & Robotham, A. S. G. 2010, MNRAS, 407, 2131, doi: 10.1111/j.1365-2966.2010.17028.x

D'Souza, R., Kauffman, G., Wang, J., & Vegetti, S. 2014, MNRAS, 443, 1433, doi: 10.1093/mnras/stu1194

Du, W., Cheng, C., Zheng, Z., & Wu, H. 2020, AJ, 159, 138, doi: 10.3847/1538-3881/ab6efb

Elias, L. M., Sales, L. V., Creasey, P., et al. 2018, MNRAS, 479, 4004, doi: 10.1093/mnras/sty1718

Faber, S. M., & Gallagher, J. S. 1979, ARA&A, 17, 135, doi: 10.1146/annurev.aa.17.090179.001031

Faber, S. M., Willmer, C. N. A., Wolf, C., et al. 2007, ApJ, 665, 265, doi: 10.1086/519294

Ferreras, I., & Silk, J. 2000, MNRAS, 316, 786, doi: 10.1046/j.1365-8711.2000.03597.x

Flynn, C., Holmberg, J., Portinari, L., Fuchs, B., & Jahreiß, H. 2006, MNRAS, 372, 1149, doi: 10.1111/j.1365-2966.2006.10911.x

Geda, R., Crawford, S. M., Hunt, L., et al. 2022, The Astronomical Journal, 163, 202, doi: 10.3847/1538-3881/ac5908

Genina, A., Deason, A. J., & Frenk, C. S. 2023, MNRAS, 520, 3767, doi: 10.1093/mnras/stad397

George, A. 2020, Master's Thesis, Department of Astronomy and Physics, Saint Mary's University. https://library2.smu.ca/xmlui/handle/01/29427

Géron, T., Smethurst, R. J., Lintott, C., et al. 2021, MNRAS, 507, 4389, doi: 10.1093/mnras/stab2064

Gilhuly, C., Merritt, A., Abraham, R., et al. 2022, ApJ, 932, 44, doi: 10.3847/1538-4357/ac6750

Gilmore, G., Wyse, R. F. G., & Kuijken, K. 1989, ARA&A, 27, 555, doi: 10.1146/annurev.aa.27.090189.003011

Giri, G., Barway, S., & Raychaudhury, S. 2023, MNRAS, 520, 5870, doi: 10.1093/mnras/stad474

González Delgado, R. M., García-Benito, R., Pérez, E., et al. 2015, A&A, 581, A103, doi: 10.1051/0004-6361/201525938

Gordon, K. D. 2007, The Spitzer Infrared Nearby Galaxies Survey (SINGS) Hubble Tuning-Fork. https://www.spitzer.caltech.edu/image/sig07-025-lifestyles-of-the-galaxies-next-door

Gott, J. R., I. 1977, ARA&A, 15, 235, doi: 10.1146/annurev.aa.15.090177.001315

Graham, A. W. 2023, MNRAS, 518, 6293, doi: 10.1093/mnras/stac3173

Graham, A. W., & Driver, S. P. 2005, , 22, 118, doi: 10.1071/AS05001

Gustafsson, B. 1989, ARA&A, 27, 701, doi: 10.1146/annurev.aa.27.090189.003413

Gwyn, S. D. J. 2008, PASP, 120, 212, doi: 10.1086/526794

Harris, C. R., Millman, K. J., van der Walt, S. J., et al. 2020, Nature, 585, 357, doi: 10.1038/s41586-020-2649-2

Hester, J. A. 2006, ApJ, 647, 910, doi: 10.1086/505614

Hilz, M., Naab, T., & Ostriker, J. P. 2013, MNRAS, 429, 2924, doi: 10.1093/mnras/sts501

Hirschmann, M., Naab, T., Ostriker, J. P., et al. 2015, MNRAS, 449, 528, doi: 10.1093/mnras/stv274

Hopkins, P. F., Bundy, K., Hernquist, L., Wuyts, S., & Cox, T. J. 2010, MNRAS, 401, 1099, doi: 10.1111/j.1365-2966.2009.15699.x

Huang, S., Ho, L. C., Peng, C. Y., Li, Z.-Y., & Barth, A. J. 2013, ApJ, 768, L28, doi: 10.1088/2041-8205/768/2/L28

Huang, S., Leauthaud, A., Greene, J. E., et al. 2018a, MNRAS, 475, 3348, doi: 10.1093/mnras/stx3200

Huang, S., Leauthaud, A., Greene, J., et al. 2018b, MNRAS, 480, 521, doi: 10.1093/mnras/sty1136

Hubble, E. P. 1936, Realm of the Nebulae

Huško, F., Lacey, C. G., & Baugh, C. M. 2022, arXiv e-prints, arXiv:2207.07139. https://arxiv.org/abs/2207.07139

Iodice, E., Capaccioli, M., Grado, A., et al. 2016, ApJ, 820, 42, doi: 10.3847/0004-637X/820/1/42

Iodice, E., Spavone, M., Capaccioli, M., et al. 2017, ApJ, 839, 21, doi: 10.3847/1538-4357/aa6846

—. 2019, A&A, 623, A1, doi: 10.1051/0004-6361/201833741

Jackson, R. A., Kaviraj, S., Martin, G., et al. 2022, MNRAS, 511, 607, doi: 10.1093/mnras/stac058

Jackson, R. A., Martin, G., Kaviraj, S., et al. 2019, MNRAS, 489, 4679, doi: 10.1093/mnras/stz2440

—. 2020, MNRAS, 494, 5568, doi: 10.1093/mnras/staa970

Jarvis, M. J., Bonfield, D. G., Bruce, V. A., et al. 2013, MNRAS, 428, 1281, doi: 10.1093/mnras/sts118

Jedrzejewski, R. I. 1987, MNRAS, 226, 747, doi: 10.1093/mnras/226.4.747

Kaviraj, S. 2014, MNRAS, 440, 2944, doi: 10.1093/mnras/stu338

Kawinwanichakij, L., Silverman, J. D., Ding, X., et al. 2021, ApJ, 921, 38, doi: 10.3847/1538-4357/ac1f21

Kennicutt, Robert C., J. 1998, ARA&A, 36, 189, doi: 10.1146/annurev.astro.36.1.189

Kormendy, J., & Djorgovski, S. 1989, ARA&A, 27, 235, doi: 10.1146/annurev.aa.27.090189.001315

Kormendy, J., & Kennicutt, Robert C., J. 2004, ARA&A, 42, 603, doi: 10.1146/annurev.astro.42.053102.134024

Kotecha, S., Welker, C., Zhou, Z., et al. 2021, arXiv e-prints, arXiv:2110.13419, doi: 10.48550/arXiv.2110.13419

Kraljic, K., Arnouts, S., Pichon, C., et al. 2018, MNRAS, 474, 547, doi: 10.1093/mnras/stx2638

Kuschel, M., Scarlata, C., Mehta, V., et al. 2022, arXiv e-prints, arXiv:2205.12169. https://arxiv.org/abs/2205.12169

Lambas, D. G., Alonso, S., Mesa, V., & O'Mill, A. L. 2012, A&A, 539, A45, doi: 10.1051/0004-6361/201117900

Lange, R., Driver, S. P., Robotham, A. S. G., et al. 2015, MNRAS, 447, 2603, doi: 10.1093/mnras/stu2467

Lawrence, A., Warren, S. J., Almaini, O., et al. 2007, MNRAS, 379, 1599, doi: 10.1111/j.1365-2966.2007.12040.x

Lazar, I., Kaviraj, S., Martin, G., et al. 2023, MNRAS, 520, 2109, doi: 10.1093/mnras/stad224

Li, J., Huang, S., Leauthaud, A., et al. 2021, arXiv e-prints, arXiv:2111.03557. https://arxiv.org/abs/2111.03557

Li, W., Nair, P., Rowlands, K., et al. 2023, MNRAS, 523, 720, doi: 10.1093/mnras/stad1473

Lin, C.-H., Chen, K.-J., & Hwang, C.-Y. 2022, arXiv e-prints, arXiv:2209.10535. https://arxiv.org/abs/2209.10535

Liu, S., Gu, Y., Yuan, Q., et al. 2021, ApJ, 923, 46, doi: 10.3847/1538-4357/ac2817

Madau, P., & Dickinson, M. 2014, ARA&A, 52, 415, doi: 10.1146/annurev-astro-081811-125615

Mahajan, S., Drinkwater, M. J., Driver, S., et al. 2018, MNRAS, 475, 788, doi: 10.1093/mnras/stx3202

Man, A., & Belli, S. 2018, Nature Astronomy, 2, 695, doi: 10.1038/s41550-018-0558-1

Man, A. W. S., Zirm, A. W., & Toft, S. 2016, ApJ, 830, 89, doi: 10.3847/0004-637X/830/2/89

Mantha, K. B., McIntosh, D. H., Brennan, R., et al. 2018, MNRAS, 475, 1549, doi: 10.1093/mnras/stx3260

Martig, M., Bournaud, F., Teyssier, R., & Dekel, A. 2009, ApJ, 707, 250, doi: 10.1088/0004-637X/707/1/250

Martin, D. C., Fanson, J., Schiminovich, D., et al. 2005, ApJ, 619, L1, doi: 10.1086/426387

Matharu, J. 2019, doi: https://doi.org/10.17863/CAM.44899

McCracken, H. J., Milvang-Jensen, B., Dunlop, J., et al. 2012, A&A, 544, A156, doi: 10.1051/0004-6361/201219507

McIntosh, D. H., Guo, Y., Hertzberg, J., et al. 2008, MNRAS, 388, 1537, doi: 10.1111/j.1365-2966.2008.13531.x

McKee, C. F., & Ostriker, E. C. 2007, ARA&A, 45, 565, doi: 10.1146/annurev.astro.45.051806.110602

McNab, K., Balogh, M. L., van der Burg, R. F. J., et al. 2021, MNRAS, 508, 157, doi: 10.1093/mnras/stab2558

Menci, N., Fontana, A., Giallongo, E., & Salimbeni, S. 2005, ApJ, 632, 49, doi: 10.1086/432788

Mercier, W., Epinat, B., Contini, T., et al. 2022, A&A, 665, A54, doi: 10.1051/0004-6361/202243110

Merritt, A., Pillepich, A., van Dokkum, P., et al. 2020, MNRAS, 495, 4570, doi: 10.1093/mnras/staa1164

Merritt, A., van Dokkum, P., Abraham, R., & Zhang, J. 2016, ApJ, 830, 62, doi: 10.3847/0004-637X/830/2/62

Miller, T. B., van Dokkum, P., & Mowla, L. 2023, ApJ, 945, 155, doi: 10.3847/1538-4357/acbc74

Moffett, A. J., Phillipps, S., Robotham, A. S. G., et al. 2019, MNRAS, 489, 2830, doi: 10.1093/mnras/stz2237

Montenegro-Taborda, D., Rodriguez-Gomez, V., Pillepich, A., et al. 2023, MNRAS, 521, 800, doi: 10.1093/mnras/stad586

Moore, B., Katz, N., Lake, G., Dressler, A., & Oemler, A. 1996, Nature, 379, 613, doi: 10.1038/379613a0

Moutard, T., Malavasi, N., Sawicki, M., Arnouts, S., & Tripathi, S. 2020, MNRAS, 495, 4237, doi: 10.1093/mnras/staa1434

Moutard, T., Sawicki, M., Arnouts, S., et al. 2018, MNRAS, 479, 2147, doi: 10.1093/mnras/sty1543

Mowla, L., van der Wel, A., van Dokkum, P., & Miller, T. B. 2019a, ApJ, 872, L13, doi: 10.3847/2041-8213/ab0379

Mowla, L. A., van Dokkum, P., Brammer, G. B., et al. 2019b, ApJ, 880, 57, doi: 10.3847/1538-4357/ab290a

Naab, T., Johansson, P. H., & Ostriker, J. P. 2009, ApJ, 699, L178, doi: 10.1088/0004-637X/699/2/L178

Naab, T., Johansson, P. H., Ostriker, J. P., & Efstathiou, G. 2007, ApJ, 658, 710, doi: 10.1086/510841

Naab, T., & Ostriker, J. P. 2017, ARA&A, 55, 59, doi: 10.1146/annurev-astro-081913-040019

Naab, T., Oser, L., Emsellem, E., et al. 2014, MNRAS, 444, 3357, doi: 10.1093/mnras/stt1919

Nelson, E. J., Tacchella, S., Diemer, B., et al. 2021, MNRAS, 508, 219, doi: 10.1093/mnras/stab2131

Nelson, E. J., Suess, K. A., Bezanson, R., et al. 2022, arXiv e-prints, arXiv:2208.01630. https://arxiv.org/abs/2208.01630

Nevin, R., Blecha, L., Comerford, J., et al. 2023, MNRAS, 522, 1, doi: 10.1093/mnras/stad911

Newman, A. B., Ellis, R. S., Bundy, K., & Treu, T. 2012, ApJ, 746, 162, doi: 10.1088/0004-637X/746/2/162

Oser, L., Ostriker, J. P., Naab, T., Johansson, P. H., & Burkert, A. 2010, ApJ, 725, 2312, doi: 10.1088/0004-637X/725/2/2312

Ownsworth, J. R., Conselice, C. J., Mortlock, A., et al. 2014, MNRAS, 445, 2198, doi: 10.1093/mnras/stu1802

Pagel, B. E. J., & Edmunds, M. G. 1981, ARA&A, 19, 77, doi: 10.1146/annurev.aa.19.090181.000453

Park, M., Tacchella, S., Nelson, E. J., et al. 2022, MNRAS, 515, 213, doi: 10.1093/mnras/stac1773

Pedregosa, F., Varoquaux, G., Gramfort, A., et al. 2012, arXiv e-prints, arXiv:1201.0490. https://arxiv.org/abs/1201.0490

Peng, Y.-j., Lilly, S. J., Kovač, K., et al. 2010, ApJ, 721, 193, doi: 10.1088/0004-637X/721/1/193

Peschken, N., Łokas, E. L., & Athanassoula, E. 2020, MNRAS, 493, 1375, doi: 10.1093/mnras/staa299

Picouet, V., Arnouts, S., Le Floc'h, E., et al. 2023, A&A, 675, A164, doi: 10.1051/0004-6361/202245756

Pillepich, A., Madau, P., & Mayer, L. 2015, ApJ, 799, 184, doi: 10.1088/0004-637X/799/2/184

Pillepich, A., Vogelsberger, M., Deason, A., et al. 2014, MNRAS, 444, 237, doi: 10.1093/mnras/stu1408

Poggianti, B. M., & Barbaro, G. 1996, in Astronomical Society of the Pacific Conference Series, Vol. 98, From Stars to Galaxies: the Impact of Stellar Physics on Galaxy Evolution, ed. C. Leitherer, U. Fritze-von-Alvensleben, & J. Huchra, 51

Puget, J. L., & Leger, A. 1989, ARA&A, 27, 161, doi: 10.1146/annurev.aa.27.090189.001113

Pulsoni, C., Gerhard, O., Arnaboldi, M., et al. 2021, A&A, 647, A95, doi: 10.1051/0004-6361/202039166

Renaud, F., Segovia Otero, Á., & Agertz, O. 2022a, MNRAS, 516, 4922, doi: 10.1093/mnras/stac2557

—. 2022b, MNRAS, 516, 4922, doi: 10.1093/mnras/stac2557

Rey, M. P., & Starkenburg, T. K. 2022, MNRAS, 510, 4208, doi: 10.1093/mnras/stab3709

Roche, N., Ratnatunga, K., Griffiths, R. E., Im, M., & Naim, A. 1998, MNRAS, 293, 157, doi: 10.1046/j.1365-8711.1998.01126.x

Rodriguez-Gomez, V., Pillepich, A., Sales, L. V., et al. 2016, MNRAS, 458, 2371, doi: 10.1093/mnras/stw456

Saglia, R. P., Sánchez-Blázquez, P., Bender, R., et al. 2016, The fundamental plane of EDisCS galaxies (Corrigendum). The effect of size evolution, Astronomy & Astrophysics, Volume 596, id.C1, 3 pp., doi: 10.1051/0004-6361/201014703e

Sandin, C. 2014, A&A, 567, A97, doi: 10.1051/0004-6361/201423429

—. 2015, A&A, 577, A106, doi: 10.1051/0004-6361/201425168

Santini, P., Castellano, M., Fontana, A., et al. 2022, arXiv e-prints, arXiv:2209.11250. https://arxiv.org/abs/2209.11250

Sawicki, M., Arcila-Osejo, L., Golob, A., et al. 2020, MNRAS, 494, 1366, doi: 10.1093/mnras/staa779

Sawicki, M., Arnouts, S., Huang, J., et al. 2019, MNRAS, 489, 5202, doi: 10.1093/mnras/stz2522

Schlegel, D. J., Finkbeiner, D. P., & Davis, M. 1998, ApJ, 500, 525, doi: 10.1086/305772

Scoville, N., Aussel, H., Brusa, M., et al. 2007, ApJS, 172, 1, doi: 10.1086/516585

Sérsic, J. L. 1963, Boletin de la Asociacion Argentina de Astronomia La Plata Argentina, 6, 41

Shen, S., Mo, H. J., White, S. D. M., et al. 2003, MNRAS, 343, 978, doi: 10.1046/j.1365-8711.2003.06740.x

Shimakawa, R., Tanaka, M., Bottrell, C., et al. 2022, PASJ, 74, 612, doi: 10.1093/pasj/psac023

Silk, J. 2013, ApJ, 772, 112, doi: 10.1088/0004-637X/772/2/112

Simard, L., Mendel, J. T., Patton, D. R., Ellison, S. L., & McConnachie, A. W. 2011, ApJS, 196, 11, doi: 10.1088/0067-0049/196/1/11

Sipols, A., & Pavlovich, A. 2020, Galaxies, 8, 48, doi: 10.3390/galaxies8020048

Smercina, A., Bell, E. F., Price, P. A., et al. 2020, ApJ, 905, 60, doi: 10.3847/1538-4357/abc485

Sotillo-Ramos, D., Pillepich, A., Donnari, M., et al. 2022, MNRAS, 516, 5404, doi: 10.1093/mnras/stac2586

Souchereau et al. in prep., GalPRIME. https://pypi.org/project/galprime/

Sousbie, T. 2011, MNRAS, 414, 350, doi: 10.1111/j.1365-2966.2011.18394.x

Spavone, M., Krajnović, D., Emsellem, E., Iodice, E., & den Brok, M. 2021, A&A, 649, A161, doi: 10.1051/0004-6361/202040186

Spavone, M., Capaccioli, M., Napolitano, N., et al. 2017, Galaxies, 5, 31, doi: 10.3390/galaxies5030031

Spavone, M., Iodice, E., van de Ven, G., et al. 2020, A&A, 639, A14, doi: 10.1051/0004-6361/202038015

Stone, C., Courteau, S., & Arora, N. 2021, ApJ, 912, 41, doi: 10.3847/1538-4357/abebe4

Strateva, I., Ivezić, Ž., Knapp, G. R., et al. 2001, AJ, 122, 1861, doi: 10.1086/323301

Streich, D., de Jong, R. S., Bailin, J., et al. 2014, A&A, 563, A5, doi: 10.1051/0004-6361/201220956

Suess, K. A., Kriek, M., Price, S. H., & Barro, G. 2021, ApJ, 915, 87, doi: 10.3847/1538-4357/abf1e4

Szomoru, D., Franx, M., & van Dokkum, P. G. 2012, ApJ, 749, 121, doi: 10.1088/0004-637X/749/2/121

Szomoru, D., Franx, M., van Dokkum, P. G., et al. 2013, ApJ, 763, 73, doi: 10.1088/0004-637X/763/2/73

—. 2010, ApJ, 714, L244, doi: 10.1088/2041-8205/714/2/L244

Tacchella, S., Diemer, B., Hernquist, L., et al. 2019, MNRAS, 487, 5416, doi: 10.1093/mnras/stz1657

Tal, T., & van Dokkum, P. G. 2011, ApJ, 731, 89, doi: 10.1088/0004-637X/731/2/89

Trayford, J. W., & Schaye, J. 2019, MNRAS, 485, 5715, doi: 10.1093/mnras/stz757

Trujillo, I. 2013, in The Intriguing Life of Massive Galaxies, ed. D. Thomas, A. Pasquali, & I. Ferreras, Vol. 295, 27–36. https://arxiv.org/abs/1211.3771

Trujillo, I., Aguerri, J. A. L., Cepa, J., & Gutiérrez, C. M. 2001a, MNRAS, 321, 269, doi: 10.1046/j.1365-8711.2001.03987.x

—. 2001b, MNRAS, 321, 269, doi: 10.1046/j.1365-8711.2001.03987.x

Trujillo, I., & Bakos, J. 2013, MNRAS, 431, 1121, doi: 10.1093/mnras/stt232

Trujillo, I., Conselice, C. J., Bundy, K., et al. 2007, MNRAS, 382, 109, doi: 10.1111/j.1365-2966.2007.12388.x

Trujillo, I., Ferreras, I., & de La Rosa, I. G. 2011, MNRAS, 415, 3903, doi: 10.1111/j.1365-2966.2011.19017.x

Trujillo, I., & Fliri, J. 2016, ApJ, 823, 123, doi: 10.3847/0004-637X/823/2/123

van der Wel, A., Franx, M., van Dokkum, P. G., et al. 2014, ApJ, 788, 28, doi: 10.1088/0004-637X/788/1/28

van Dokkum, P. G., & Franx, M. 1996, MNRAS, 281, 985, doi: 10.1093/mnras/281.3.985

—. 2001a, ApJ, 553, 90, doi: 10.1086/320645

—. 2001b, arXiv e-prints, astro, doi: 10.48550/arXiv.astro-ph/0101468

van Dokkum, P. G., Whitaker, K. E., Brammer, G., et al. 2010, ApJ, 709, 1018, doi: 10.1088/0004-637X/709/2/1018

Virtanen, P., Gommers, R., Oliphant, T. E., et al. 2020, Nature Methods, 17, 261, doi: 10.1038/s41592-019-0686-2

Wechsler, R. H., & Tinker, J. L. 2018, ARA&A, 56, 435, doi: 10.1146/annurev-astro-081817-051756

White, S. D. M., & Frenk, C. S. 1991, ApJ, 379, 52, doi: 10.1086/170483

Whitney, A., Conselice, C. J., Duncan, K., & Spitler, L. R. 2020, ApJ, 903, 14, doi: 10.3847/1538-4357/abb824

Williams, R. J., Quadri, R. F., Franx, M., van Dokkum, P., & Labbé, I. 2009, ApJ, 691, 1879, doi: 10.1088/0004-637X/691/2/1879

Willmer, C. N. A. 2018, ApJS, 236, 47, doi: 10.3847/1538-4365/aabfdf

Wilman, D. J., Fossati, M., Mendel, J. T., et al. 2020, ApJ, 892, 1, doi: 10.3847/1538-4357/ab7914

York, D. G., Adelman, J., Anderson, John E., J., et al. 2000, AJ, 120, 1579, doi: 10.1086/301513

Zhang, C., Peng, Y., Ho, L. C., et al. 2021, ApJ, 911, 57, doi: 10.3847/1538-4357/abd723

Zhang, H., & Zaritsky, D. 2016, MNRAS, 455, 1364, doi: 10.1093/mnras/stv2413